June 25, 2019

GMD-2019-15: Revision

Dear Editor,

We are pleased to submit our revised manuscript entitled: "Developing a monthly radiative kernel for surface albedo change from satellite climatologies of Earth's shortwave radiation budget: CACK v1.0" for publication consideration in *Geoscientific Model Development*.

Major changes to the manuscript include:

- A major re-structuring to improve overall flow and readability. This re-structuring was necessary to showcase CACK v1.0 as a comprehensive, transparent, and flexible dataset built on a novel model (parameterization) of shortwave radiation transfer.
- An expanded analysis of CACK's performance including new content on uncertainty and two new demonstrations of its application
- An improved description of the methods to ensure reproducibility, in particular that pertaining to the symbolic regression analysis
- The addition of a Supporting Information document providing additional detail surrounding CACK's uncertainty calculations, the symbolic regression method and results, and a detailed description of the CACK v1.0 dataset which now includes estimates for three sources of uncertainty.

The revised manuscript has increased by ~2,000 words, 3 figures, and 1 table. We feel confident that our revisions go above and beyond that which is required to satisfy reviewers and add notable value to the paper serving to elevate its overall impact. For instance, the new and comprehensive analysis on uncertainty and its inclusion in CACK v1.0 should make it more attractive as a credible candidate for use as part of a future Monitoring, Reporting, and Verification (MRV) framework for radiative forcing impacts of albedo changes on land.

Please do not hesitate contacting us should you require additional information or clarification.

Kind Regards,

Ryan M. Bright and Tom L. O'Halloran

Reponses to Anonymous Referee #1

This study by Bright and O'Halloran developed shortwave radiative kernels based on the CERES EBAF products, which would be an alternative to GCM-based kernels. The performance of the observation-based kernels is also evaluated based on the multi-GCM mean. This is an interesting study, and the developed shortwave radiative kernels have the potential of being used for land use-climate studies. However, I think the manuscript needs some improvement and further development in the analysis before it can be published.

We thank Anonymous Referee #1 for his/her constructive feedback. To address his/her major concerns, we have provided more detail about the GCM kernels and their uncertainties, improved the description of our methodology, and provided two examples illustrating CACK's application.

My major concerns include:

1. The evaluation of CERES kernels uses four GCM kernels as benchmarks. I am wondering the uncertainties among the different GCMs. GCM uncertainties are largely related to their representation of low-level cloud cover and properties (please see our reference to Dolinar *et al.* 2015 [original manuscript P3 L67]). Regarding cloud properties, one of the major differences among GCMs is related to the representation of atmospheric liquid water/ice associated with convective clouds. Of the four GCMs we considered, only CAM5 and GFDL attempt to model the effects of precipitating and/or convective core ice and liquid in their radiation calculations. We add this detail in (new) Section 2.a and provide a new citation (e.g., to Li et al. (2013)). First, why are these four models chosen? These GCM kernels were chosen simply because at the time the study commenced these were the only ones available. We add this rationale to the main text (new Section 2.a). But why CAM3 and GFDL are not mentioned in the results? We carried out a two-stage evaluation, where CAM3 and GFDL comprised part of the "multi-GCM mean" benchmark we used in the first stage (described in new Section 4a), whose results are presented in (new) Section 5, Figures 1 & 2. We hope our re-organization and improved methods descriptions have now made this clearer. Second, for Figure 1, if plotting the radiative kernel for individual GCMs, is there a large spread like the CERES-based estimates? This is a great question and we agree that the spread in GCMs should be made more visible. We have revised Figure 1 such that is now shows the spread (taken as 1 standard deviation) in latitudinal means across the four GCMs. Third, are the author's conclusions model-dependent? Because the BO18 kernel is trained using the multi-GCM mean as the reference, it is not surprising that it has better performance than other CERES kernels. This is a fair comment and valid concern. To check this, we re-ran the machine learning algorithm twice, first using a random sample of the CAM5 kernel (as the dependent) with its own boundary fluxes (as independents), the second time using a random sample of the ECHAM6 kernel with its own boundary fluxes as input (note: these were the only two kernels for which the boundary fluxes used to derive them were also available to us). The BO18 model emerged as the best solution (i.e., model form) common to the two independent machine learning analyses. Because the BO18 model was then applied using CERES EBAF inputs and subsequently compared to a multi-GCM mean that included the two additional GCM kernels (i.e., GFDL and CAM3) that were not part of the model training exercise, we feel confident that the BO18 model is robust and insensitive to the GCM kernels used for training. However, if using a single GCM (or including other GCMs, like HadGEM2 radiative kernels, Smith 2018) as the benchmarks, will QH06 or ANISO still be better than other kernel models? Yes, we indeed found this to be the case – that whether benchmarking to multi-GCM means or to specific GCMs, the CERES kernel performance ranking remained unchanged (excluding the QH06 kernel for the reason provided in revised Section 5b). The authors may

need more analysis and discussion about the model dependency. We have added a section in the Discussion regarding BO18's model (in)dependency.

2. One of the motivations of this study is "atmospheric state variables used as model input are limited to single years, thus being sensitive to anomalous weather conditions that may have occurred in those years". Can you explain more about this? As the authors mentioned in L278, they are comparing the multi-year CERES kernel to a single-year GCM kernel. I assume the GCM simulations are only one-year long? The authors may need to provide more description and discussion about these GCM simulations. The GCM simulations from which the kernels are derived are indeed carried out for a period of one year. However, when going back to double check this, we discovered that we had mistook this for the temporal signature and duration of the prescribed atmospheric background state, which for three of the four GCM kernels does extend beyond a single year. We now include a new table (Table 1) that summarizes this and other differences between the GCMs used to derive the GCM kernels and delete the incorrect statement quoted above. If the simulates are for a specific year (which year?), or a climatological run, are they comparable to the CERES-based kernel models which are for the period 2001-2016. No GCM kernel is comparable to the 2001-2016 CERES kernel; background climatologies of ECHAM6, CAM3, and GFDL kernels span several years (or decades) but all pre-date the CERES EBAF era. CAM5's background does fall within the CERES era but is based on a single year only. These discrepancies are why we chose to compare to the mean of all four kernels in our initial performance screening. We chose not to compare the CAM5 kernel to a CERES kernel based on the same background year because the atmospheric state information underlying CAM5 is not based on CERES EBAF (i.e., it would still not be possible to attribute disagreement to differences in the representation of shortwave radiative transfer). This is why we chose instead to emulate CAM5 with the BO18 parameterization run with CAM5's own boundary fluxes. Additionally, I am curious about the inter-annual variability of the multi-year CERES kernels. The interannual variability of a kernel based on CERES can now be inferred from the results of our second application example (Figure 7 C, southern Amazonian deforestation).

3. This study is started with the "need within LULCC science community for simple and transparent tools for predicting radiative forcings from surface albedo changes". Is it possible to provide a simple example of how to apply CACK v1.0 to the LULCC studies? This is a fair request and have thus invested notable effort into demonstrating how both a climatological CACK and a temporally-explicit CACK may be applied to estimate radiative forcings in LULCC studies (New Sections 4 d & e, 5 d & e, and new Figures 6 & 7).

Specific comments:

1. The organization of section 2 and section 3 is a little confusing. The title of section 2 is "Review of existing approaches", but most of the kernels described in section 3 are also "existing approaches", aren't they? We fully agree and have carried out a major re-organization of the manuscript. We are confident that the new manuscript structure is more intuitive and easier to follow and digest.

2. L40, What do you mean by "offline"? Run land surface model offline? Here we mean that GCMs are not practical to apply for estimating albedo change RFs for single locations, and that other modeling approaches have been applied for this purpose involving stand-alone radiative transfer modeling in which the surface and atmosphere are not coupled. I also can't find the paper (Randerson et al. 2006) in the reference. Thank you for pointing out this missing reference which has now been added.

3. L151, Eq. (3) and Eq. (4), are __s and __ the same thing? If yes, it would be better to keep the consistency. Yes, these are the same and have been corrected (thanks).

4. L247, Which part (or period) of data is used for model training, and which part is used for prediction? Model training and prediction datasets are based on a random sampling in both time and space (200,000 grid cells in each). This detail has been added to (new) Section 3 d).

5. L263, It should be "e. Initial screening of candidate models for a CERES-based kernel". Corrected.

6. L409, They are mean absolute bias, not RMSD. Corrected.

7. L441-444, Can the authors explain more about how the land-based solar radiation management is an example of the CACK's flexibility? This was a poorly constructed sentence which has been deleted in the revision.

Reference:
Smith, Christopher J. (2018) HadGEM2 radiative kernels. University of Leeds. [Dataset] https://doi.org/10.5518/406

Reponses to Anonymous Referee #2

General comments

The manuscript presented by Bright and O'Halloran suggests the use of a new kernel (CACKv1.0) to derive radiative forcing at the top of the atmosphere from surface albedo changes. This kernel is derived by applying a machine learning technique to identify a formula which can best reproduce the results from kernels derived from Global Circulation Models, once it is applied to CERES satellite-derived data. The authors argue that compared to GCM-derived kernels, this new formula would 1) enable a more transparent derivation of radiative forcing from surface albedo changes, and 2) rely on data from several years. Their analysis shows that the new formula performs better at mimicking the results from GCM-derived kernels compared to previously suggested formulations. They suggest the use of their results by the scientists studying the impacts of land-use and land-cover changes (LULCC) on climate to improve their calculations of radiative forcing from surface albedo changes.

Having an easily applicable kernel that reproduces the results from GCMs can indeed be useful for the LULCC community, and in that sense the authors' initiative is welcome and scientifically significant. Having said that, there are a couple of issues with the authors' approach, while the methodology could be better described to ensure reproducibility of the results. Overall, substantial work also needs to be done on the writing to improve understandability of the manuscript. These issues are not insurmountable, but I recommend that they are addressed before the manuscript is accepted.

We thank Anonymous Referee #2 for his/her constructive feedback. To address his/her major concerns, we have carried out a major re-structuring of the paper that we now believe is easier to follow and more intuitive to digest. This includes more attention to CACK's uncertainties as well as the uncertainties between GCM kernels, and we now include uncertainty estimates for CACK in effort to make CACK v1.0 a more attractive and complete dataset. Lastly, we have also

invested notable effort to improve the description of our methods to better-ensure reproducibility of results.

- Specific comments

The real added value of CACK compared to previously suggested simple formulations can only be assessed in light of the uncertainties between GCM kernels. These thus need to be included at least in Figure 1 and discussed in the manuscript, so that the readers can assess for themselves how much of a difference using CACK rather than a simple isotropic kernel (for example) makes. This is a fair comment. We have added additional text describing major sources of uncertainty in GCM-based kernels (new Section 2.a), a new table (new Table 1) highlighting the major differences between them, and a new Figure 1 that now shows the spread among the four GCM kernels we employed (expressed in terms of the seasonal and latitude band mean standard deviations). The authors also mention that the GCM-derived kernels are based on single years of forcing data. This renders them uncertain and thus less appropriate as a benchmark, therefore the authors choose to use the multi-GCM mean kernel as a reference to partly alleviate the lack of consideration of interannual variability when they were derived. This seems reasonable but only
partly alleviates the issue. In addition to being explicitly shown and discussed, the uncertainties about GCM-derived kernels (both related to model spread and interannual variability) need to be acknowledged in the Discussion. Even in the current state, more conclusions could be drawn from Figure 1 by describing for example which kernels perform worst against the GCM-derived ones and potentially advancing reasons why this is the case. We believe the revised Figure 1 sufficiently demonstrates the performance of all CERES kernel candidates in light of discrepancies among the GCM kernels themselves.

The methodology should be more detailed to be able to understand how Equation 16 is derived. Which optimal structures and coefficients are considered during the symbolic regression? What should make the reader think that this approach doesn't miss potentially relevant formulas? And which "boundary fluxes (or system parameters derived from these fluxes) that minimized the sum of squared residuals. . ." were considered? This information should at least be provided in the Supplementary Material. This is a fair comment and have thus provided more detail surrounding Eq. (16) (now Eq. (17)) in (new) Section 2.d, including what fluxes were included and what constraints were applied, as well as providing other detail in a new section of the Supporting Information. In the Supporting Information we provide examples of alternate model structures obtained from the machine learning exercise, their performance metrics, and the criteria we applied in the model selection process.

It is also not so clear from the current manuscript why certain choices were made regarding the GCM and kernel selections. Why are four GCM kernels included in the study, are these the only ones available? Correct, these are the only four GCM kernels available at the time the study commenced. We add this rationale to the main text (new Section 2 a). Is there some information existing on the quality of these kernels that guided the selection? Could the authors justify why they "emulated" the kernels of just two GCMs in a second step? Only ECHAM6 and CAM5 kernels were used in the emulation exercise because these were the only two kernels for which the boundary fluxes were also provided (which were needed for the machine learning-based model selection and for kernel emulation). We add this justification to (new) Section 3 b. It seems like only the 3 kernels performing best against the GCM-derived ones were retained for further analysis, but this is also not explicitly mentioned. We have added a sentence at the end of

(new) Section 4 a explicitly stating why only these three kernels were retained for further analysis (i.e., they were the top performers of the initial CERES candidate model evaluation exercise).

The structure of the manuscript could be improved to facilitate understandability. For example, why not mentioning the isotropic and anisotropic kernels, as well as the kernel from Qu and Hall in Section 2 already. Currently, at first it may read like they have been derived by the authors. The names of the studies that introduced other types of statistical kernels could also be added in the subsection titles to help the reader follow. We agree that our manuscript needed a more logical organization to facilitate improved readability. We believe the new organization leaves the reader with zero doubt about the origin of the CERES model candidates we consider in the paper.

The description of the CERES dataset also seems misplaced in Section 2. Additionally, in some occurrences the subsection numbering is wrong and the placeholders for Figures or Tables misplaced. We agree and have re-structured the manuscript accordingly such that description of the CERES EBAF v4 products is now provided up front in the Introduction. We have checked and updated all section/table/figure numbering.

Last but not least, the CACK dataset is only mentioned in the conclusion, although from the title it sounds like an important output of the study. If this is the case, it would need to be introduced in the abstract and the introduction of the manuscript. But ultimately, one may wonder whether describing CACK as a dataset is appropriate. Could the authors maybe develop on what makes it more than just applying Eq. 16 to CERES data, for example in terms of pre-processing or perspectives for updates, etc.? We agree that the value of CACK v1.0 packaged as a dataset (i.e., more than just Eq. (17) applied to CERES data) ought to be highlighted and clearly showcased. We have therefore invested considerable effort into describing and quantifying the various sources of uncertainty of CACK and include these as part of a more comprehensive CACK v1.0 data product. We believe this addition strengthens the credibility of CACK v1.0 as a data product and as a viable tool for the advancement of a verification framework for biogeophysical climate forcings on land.

- Technical comments

l. 68: "An additional downside is the that". Check typo Corrected typo.
l. 157: to facilitate understandability it could be good to repeat the downsides of GCMderived kernels here We agree and include this as part of (new) Section 2 a.
l. 425: "course" should read "coarse" Corrected.
l. 704-705: can the authors make clearer what is meant by "100X100 sample grid"? Clarified.

Developing a monthly radiative kernel for surface albedo change from satellite climatologies of Earth's shortwave radiation budget: CACK v1.0

Ryan M. Bright[1*] and Thomas L. O'Halloran[2,3]

1 – Norwegian Institute of Bioeconomy Research, Ås, Norway

2 – Department of Forestry and Environmental Conservation, Clemson University, Clemson, South Carolina, USA.

3 – Baruch Institute of Coastal Ecology and Forest Science, Clemson University, Georgetown, South Carolina, USA

[*]Contact: ryan.bright@nibio.no

Abstract

Due to the potential for land use / land cover change (LULCC) to alter surface albedo, there is need within the LULCC science community for simple and transparent tools for predicting radiative forcings (ΔF) from surface albedo changes ($\Delta\alpha_s$). To that end, the radiative kernel technique – developed by the climate modeling community to diagnose internal feedbacks within general circulation models (GCMs) – has been adopted by the LULCC science community as a tool to perform offline ΔF calculations for $\Delta\alpha_s$. However, the codes and data behind the GCM kernels are not readily transparent, and the climatologies of the atmospheric state variables used to derive them vary widely both in time period and duration. Observation-based kernels offer an attractive alternative to GCM-based kernels and could be updated annually at relatively low costs. Here, we present a radiative kernel for surface albedo change founded on a novel, simplified parameterization of shortwave radiative transfer driven with inputs from the Clouds and the Earth's Radiant Energy System (CERES) Energy

Balance and Filled (EBAF) products. When based on a 16-year climatology (2001-2016), we find that the CERES albedo change kernel – or CACK – agrees remarkably well with the mean kernel of four GCMs (rRMSE = 14%). When the novel parameterization underlying CACK is applied to emulate two of the GCM kernels using their own boundary fluxes as input, we find even greater agreement (mean rRMSE = 7.4%), suggesting that this simple and transparent parameterization represents a credible candidate for a satellite-based alternative to GCM kernels. We document and compute the various sources of uncertainty underlying CACK and include them as part of a more extensive dataset (CACK v1.0) while providing examples showcasing its application.

Keywords: GCM, radiative forcing, land use change, land cover change, LULCC

1. Introduction

Diagnosing changes to the shortwave radiation balance at the top-of-the-atmosphere (TOA) resulting from changes to albedo at the surface ($\Delta\alpha_s$) is an important step in predicting climate change. However, outside the climate science community, many researchers do not have the tools to convert $\Delta\alpha$ to the climate-relevant ΔF measure (Bright, 2015; Jones et al., 2015), which requires a detailed representation of the atmospheric constituents that absorb or scatter solar radiation (e.g. cloud, aerosols, and gases) and a sophisticated radiative transfer code. For single points in space or for small regions, these calculations are typically performed offline – meaning without feedbacks to the atmosphere (e.g., (Randerson et al., 2006))). Large-scale investigations (e.g. Amazonian or pan-boreal LULCC (Bonan et al., 1992; Dickinson and Henderson-Sellers, 1988)) typically prescribe the land surface layer in a GCM with initial and perturbed states, allowing the radiative transfer code to interact with the rest of the model. While this has the benefit of allowing interaction and feedbacks between surface albedo and scattering or absorbing components of the model, such an approach is

computationally expensive and thereby restricts the number of LULCC scenarios that can be investigated (Atwood et al., 2016). Consequently, this method does not meet the needs of some modern LULCC studies which may require millions of individual land cover transitions to be evaluated cost effectively (Ghimire et al., 2014; Lutz and Howarth, 2015).

Within the LULCC science community, two methods have primarily met the need for efficient ΔF calculations from $\Delta\alpha_s$: simplified parameterizations of atmospheric transfer of shortwave radiation (Bozzi et al., 2015; Bright and Kvalevåg, 2013; Caiazzo et al., 2014; Carrer et al., 2018; Cherubini et al., 2012; Muñoz et al., 2010), and radiative kernels (Ghimire et al., 2014; O'Halloran et al., 2012; Vanderhoof et al., 2013) derived from sophisticated radiative transfer schemes embedded in GCMs (Block and Mauritsen, 2014; Pendergrass et al., 2018; Shell et al., 2008; Soden et al., 2008). Simplified parameterizations of the LULCC science community have not been evaluated comprehensively in space and time. Bright & Kvalevåg (2013) evaluated the shortwave ΔF parameterization of Cherubini *et al.* (2012) when applied at several globally distributed sites on land, finding inconsistencies in performance at individual sites despite good overall cross-site performance. Radiative kernels (Block and Mauritsen, 2014; Pendergrass et al., 2018; Shell et al., 2008; Soden et al., 2008) – while being based on state-of-the-art models of radiative transfer – have the downside of being model-dependent and not readily transparent. While the radiative transfer codes behind them are well-documented, the scattering components (i.e. aerosols, gases, and clouds) affecting transmission have many simplifying parameterizations, vary widely across models, and may contain significant biases (Dolinar et al., 2015; Wang and Su, 2013). An additional downside is that the atmospheric state climatologies used to compute the GCM kernels vary widely in their time periods (i.e., from pre-industrial to the year 2007) and durations (from 1 to 1,000 yrs). The application of a state-dependent GCM kernel that is outdated may be undesirable in regions undergoing rapid changes in cloud cover or aerosol optical depth, such

as in the northwest United States (Free and Sun, 2014) and in southern and eastern Asia (Srivastava, 2017; Zhao et al., 2018), respectively. An albedo change kernel based on Earth-orbiting satellite products could be updated annually to capture changes in atmospheric state at relatively low costs.

The NASA Clouds and the Earth's Radiant Energy System (CERES) Energy Balance and Filled (EBAF) products (CERES Science Team, 2018a, b), which are based largely on satellite optical remote sensing, provide the monthly mean boundary fluxes and other atmospheric state information (e.g., cloud area fraction, cloud optical depth) that could be used to develop a more empirically-based alternative to the GCM-based kernels. The latest EBAF-TOA Ed4.0 (version 4.0) products have many improvements with respect to the previous version (version 2.8, Loeb et al. 2009), including the use of advanced and more consistent input data, retrieval of cloud properties, and instrument calibration (Kato et al., 2018; Loeb et al., 2017).

Here, we present an albedo change kernel based on the CERES EBAF v4 products – or CACK. Underlying CACK is a simplified model of shortwave radiative transfer through a one-layer atmosphere. The model form (or parameterization) is selected after a two-stage performance evaluation of six model candidates: two analytical, one semi-empirical, and three empirical. An initial performance screening is implemented where all six model candidates are driven with a 16-year climatology (January 2001 – December 2016) of monthly all-sky boundary fluxes from CERES, with the resulting kernels benchmarked both qualitatively and quantitatively against the mean of four GCM-based kernels (Block and Mauritsen, 2014; Pendergrass et al., 2018; Shell et al., 2008; Soden et al., 2008). Top model candidates from the initial performance screening are then subjected to an additional performance evaluation where they are applied to emulate two GCM kernels using their own

boundary fluxes as input, which eliminates possible biases related to differences in the GCM representation of clouds or other atmosphere state variables.

We start in Section 2 by providing a brief overview of existing approaches applied in LULCC climate studies for estimating ΔF from $\Delta\alpha$. We then present the six model candidates in Section 3. Section 4 describes the model evaluation and uncertainty quantification methods, in addition to two application examples. Results are presented in Section 5, while Section 6 discusses the merits and uncertainties of a CERES-based kernel relative to GCM-based kernels.

2 Review of existing approaches

Earth's energy balance (at TOA) in an equilibrium state can be written:

$$0 = F = LW_{\uparrow}^{TOA} - (SW_{\downarrow}^{TOA} - SW_{\uparrow}^{TOA}) \quad (1)$$

where the equilibrium flux F is a balance between the net solar energy inputs ($SW_{\downarrow}^{TOA} - SW_{\uparrow}^{TOA}$) and thermal energy output ($LW_{\uparrow}^{TOA}$). Perturbing this balance results in a radiative forcing ΔF, while perturbing the shortwave component is referred to as a shortwave radiative forcing and may be written as:

$$\Delta F = \Delta(SW_{\downarrow}^{TOA} - SW_{\uparrow}^{TOA}) = \Delta SW_{\downarrow}^{TOA}\left(1 - \frac{SW_{\uparrow}^{TOA}}{SW_{\downarrow}^{TOA}}\right) - SW_{\downarrow}^{TOA}\left(\Delta\frac{SW_{\uparrow}^{TOA}}{SW_{\downarrow}^{TOA}}\right) \quad (2)$$

where the shortwave radiative forcing results either from changes to solar energy inputs ($\Delta SW_{\downarrow}^{TOA}$) or from internal perturbations within the Earth system ($\Delta\frac{SW_{\uparrow}^{TOA}}{SW_{\downarrow}^{TOA}}$). The latter can be brought about by changes to the reflective properties of Earth's surface which is the focus of this paper.

a. GCM-based radiative kernels

The radiative kernel technique was developed as a way to assess various climate feedbacks from climate change simulations across multiple climate models in a computationally efficient manner (Shell et al., 2008; Soden et al., 2008). A radiative kernel is defined as the differential response of an outgoing radiation flux at TOA to an incremental change in some climate state variable -- such as water vapor, air temperature, or surface albedo (Soden et al., 2008). To generate a radiative kernel for a change in surface albedo with a GCM, the prescribed surface albedo change is perturbed incrementally by 1%, and the response by the outgoing shortwave radiation flux at TOA is recorded:

$$\Delta SW_{\uparrow}^{TOA} = SW_{\uparrow}^{TOA}(\alpha_s + \Delta\alpha_s) - SW_{\uparrow}^{TOA}(\alpha_s) = \frac{\partial SW_{\uparrow}^{TOA}}{\partial \alpha_s}\Delta\alpha_s \equiv K_{\alpha_s}\Delta\alpha_s \quad (3)$$

where $SW_{\uparrow}^{TOA}$ is the outgoing shortwave flux at TOA and K_{α_s} is the radiative kernel (in Wm^{-2}) which can then be used with Eq. (1) to estimate an instantaneous shortwave radiative forcing (ΔF) at TOA:

$$\begin{aligned} F + \Delta F &= LW_{\uparrow}^{TOA} - (SW_{\downarrow}^{TOA} - SW_{\uparrow}^{TOA} + K_{\alpha_s}\Delta\alpha_s) \\ \Delta F &= -K_{\alpha_s}\Delta\alpha_s \end{aligned} \quad (4)$$

To the best of our knowledge, four albedo change kernels have been developed based on the following GCMs: the Community Atmosphere Model version 3, or CAM3 (Shell et al., 2008), the Community Atmosphere Model version 5, or CAM5 (Pendergrass et al., 2018), the European Center and Hamburg model version 6, or ECHAM6 (Block and Mauritsen, 2014), and the Geophysical Fluid Dynamics Laboratory model version AM2p12b, or GFDL (Soden et al., 2008). These four GCM kernels vary in their vertical and horizontal resolutions, their parameterizations of shortwave radiative transfer, and their prescribed atmospheric state climatologies. These differences are summarized in Table 1. Apart from differences in their

prescribed atmospheric background states and radiative transfer schemes, a major source of uncertainty in GCM-based kernels is related to the GCM representation of atmospheric liquid water/ice associated with convective clouds; of the four aforementioned GCMs, only CAM5 and GFDL attempt to model the effects of convective core ice and liquid in their radiation calculations (Li et al., 2013).

< Table 1 >

b. Single-layer atmosphere models of shortwave radiation transfer

Within the atmospheric science community, various simplified analytical or semi-empirical modeling frameworks have been developed, either to diagnose effective surface and atmospheric optical properties from climate model outputs, or to study the relative contributions of changes to these properties on shortwave flux changes at the top and bottom of the atmosphere (Atwood et al., 2016; Donohoe and Battisti, 2011; Kashimura et al., 2017; Qu and Hall, 2006; Rasool and Schneider, 1971; Taylor et al., 2007; Winton, 2005; Winton, 2006). While these frameworks all treat the atmosphere as a single layer, they differ by whether or not the reflection and transmission properties of this layer are assumed to have a directional dependency (Stephens et al., 2015) and by whether or not inputs other than those derived from the boundary fluxes are required (e.g. cloud properties; (Qu and Hall, 2006)).

Winton (2005) presented a semi-empirical four-parameter optical model to account for the directional dependency of up- and downwelling shortwave fluxes through the one-layer atmosphere and found good agreement (rRMSE < 2% globally) when benchmarked to online radiative transfer calculations. Also considering a directional dependency of the atmospheric optical properties, Taylor et al. (2007) presented a two-parameter analytical model where atmospheric absorption was assumed to occur at a level above atmospheric reflection. The

analytical model of Donohoe and Battisti (2011) subsequently relaxed the directional dependency assumption and found the atmospheric attenuation of the surface albedo contribution to planetary albedo to be 8% higher than the model of Taylor et al. (2007). Elsewhere, Qu & Hall (2006) developed an analytical framework making use of additional atmospheric properties such as cloud cover fraction, cloud optical thickness, and the clear-sky planetary albedo, which proved highly accurate when model estimates of planetary albedo were evaluated against climate models and satellite-based datasets.

c. Simple empirical parameterizations of the LULCC science community

Two simple empirical parameterizations of shortwave radiative transfer have been widely applied within the LULCC science community for estimating ΔF from $\Delta\alpha_s$ (Bozzi et al., 2015; Caiazzo et al., 2014; Carrer et al., 2018; Cherubini et al., 2012; Lutz et al., 2015; Muñoz et al., 2010). While these parameterizations are also based on a single-layer atmosphere model of shortwave radiative transfer, at the core of these parameterizations is the fundamental assumption that radiative transfer is wholly independent of (or unaffected by) $\Delta\alpha_s$. In other words, they neglect the change in the attenuating effect of multiple reflections between the surface and the atmosphere that accompanies a change to the surface albedo. Nevertheless, due to their simplicity and ease of application they continue to be widely employed in climate research.

3. Kernel model candidates

The six candidate models (or parameterizations) for a CERES-based albedo change kernel (CACK) are presented henceforth. All requisite variables and their derivatives may be obtained directly from the CERES EBAF v4 products (at monthly and 1° × 1° resolution) and are presented in Table 2. To improve readability, temporal and spatial indexing is neglected and all terms presented henceforth in Section 3 denote the monthly pixel means.

< Table 2 >

a. Analytical kernels

The first kernel candidate may be analytically-derived from the CERES EBAF all-sky boundary fluxes and their derivatives. The surface contribution to the outgoing shortwave flux at TOA $SW_{\uparrow,SFC}^{TOA}$ can be expressed (Donohoe and Battisti, 2011; Stephens et al., 2015; Winton, 2005) as:

$$SW_{\uparrow,SFC}^{TOA} = SW_{\downarrow}^{TOA}\alpha_s \frac{(1-r-a)^2}{(1-r\alpha_s)} \tag{5}$$

where r is a single pass atmospheric reflection coefficient, a is a single pass atmospheric absorption coefficient, $SW_{\downarrow}^{TOA}$ is the extraterrestrial (downwelling) shortwave flux at TOA, and α_s is the surface albedo (defined in Table 2). The expression in the denominator of the righthand term represents a fraction attenuated by multiple reflections between the surface and the atmosphere. This model assumes that the atmospheric optical properties r and a are insensitive to the origin and direction of shortwave fluxes – or in other words – that they are isotropic.

The single-pass reflectance coefficient is calculated from the system boundary fluxes (Table 2) following Winton (2005) and Kashimura *et al.* (2017):

$$r = \frac{SW_{\downarrow}^{TOA}SW_{\uparrow}^{TOA} - SW_{\downarrow}^{SFC}SW_{\uparrow}^{SFC}}{SW_{\downarrow}^{TOA\ 2} - SW_{\uparrow}^{SFC\ 2}} \tag{6}$$

while the single-pass absorption coefficient a is given as:

$$a = 1 - r - T(1-\alpha_s r) \tag{7}$$

where T is the clearness index (defined in Table 2). Our interest is in quantifying the $SW_{\uparrow,SFC}^{TOA}$ response to an albedo perturbation at the surface – or the partial derivative of $SW_{\uparrow,SFC}^{TOA}$ with respect to α in Eq. (5):

$$\frac{\partial SW_{\uparrow}^{TOA}}{\partial \alpha_s}\Delta\alpha_s = K_{\alpha_s}^{ISO}\Delta\alpha_s = \frac{SW_{\downarrow}^{TOA}(1-r-a)^2}{(1-r\alpha_s)^2}\Delta\alpha_s \tag{8}$$

where $K_{\alpha_s}^{ISO}$ is referred to henceforth as the *Isotropic* kernel.

The second analytical kernel is based on the model of Qu and Hall (2006) which makes use of auxiliary cloud property information commonly provided in satellite-based products of Earth's radiation budget – including CERES EBAF – such as cloud cover area fraction, cloud visible optical depth, and clear-sky planetary albedo. This model links all-sky and clear-sky effective atmospheric transmissivities of the earth system through a linear coefficient k relating the logarithm of cloud visible optical depth to the effective all-sky atmospheric transmissivity:

$$k = \frac{(T_{a,CLR}) - (T_a)}{\ln(\tau + 1)} \tag{9}$$

where $T_{a,CLR}$ is the clear-sky effective system transmissivity, T_a is the all-sky effective system transmissivity, and τ is the cloud visible optical depth. This linear coefficient can then be used together with the cloud cover area fraction to derive a shortwave kernel based on the model of Qu and Hall (2006) – or $K_{\alpha_s}^{QH06}$:

$$\frac{\partial SW_{\uparrow}^{TOA}}{\partial \alpha_s}\Delta\alpha_s = K_{\alpha_s}^{QH06}\Delta\alpha_s = SW_{\downarrow}^{SFC}\left[(T_a) - kc\ln(\tau + 1)\right]\Delta\alpha_s \tag{10}$$

where c is the cloud cover area fraction.

b. Semi-empirical kernel

The third kernel makes use of three directionally-dependent (anisotropic) bulk optical properties $r_{\uparrow}$, $t_{\uparrow}$, and $t_{\downarrow}$, where the first is the atmospheric reflectivity to upwelling shortwave radiation and the latter two are the atmospheric transmission coefficients for upwelling and downwelling shortwave radiation, respectively (Winton, 2005). It is not possible to derive $r_{\uparrow}$ analytically from the all-sky boundary fluxes; however, Winton (2005) provides an empirical formula relating upwelling reflectivity $r_{\uparrow}$ to the ratio of all-sky to clear-sky fluxes incident at surface:

$$r_{\uparrow} = 0.05 + 0.85\left(1 - \frac{SW_{\downarrow}^{SFC}}{SW_{\downarrow,CLR}^{SFC}}\right) \tag{11}$$

where $SW_{\downarrow,CLR}^{SFC}$ is the clear-sky shortwave flux incident at the surface.

Knowing $r_{\uparrow}$, we can then solve for the two remaining optical parameters needed to obtain our kernel:

$$t_{\downarrow} = \frac{SW_{\downarrow}^{SFC} - r_{\uparrow} SW_{\uparrow}^{SFC}}{SW_{\downarrow}^{TOA}} \tag{12}$$

$$t_{\uparrow} = T_a - \left[t_{\downarrow} - t_{\downarrow}(1 - r_{\uparrow}\alpha_s)\right] \tag{13}$$

where T_a is the effective atmospheric transmittance (Table 2) of the earth system.

The kernel may now be expressed as:

$$\frac{\partial SW_{\uparrow}^{TOA}}{\partial \alpha_s}\Delta\alpha_s = K_{\alpha_s}^{ANISO}\Delta\alpha_s = \frac{SW_{\downarrow}^{TOA} t_{\downarrow} t_{\uparrow}}{(1 - r_{\uparrow}\alpha_s)^2}\Delta\alpha_s \tag{14}$$

where $K_{\alpha_s}^{ANISO}$ is henceforth referred to as the *Anisotropic* kernel.

c. Existing empirical parameterizations

248 Although not referred to as "kernels" in the literature *per se*, we present the simple empirical
249 parameterizations as such to ensure consistency with previously described notation and
250 terminology.
251
252 The first candidate parameterization, originally presented in Muñoz *et al*. (2010), makes use
253 of a local two-way transmittance factor based on the local clearness index:

254 $$\frac{\partial SW_{\uparrow}^{TOA}}{\partial \alpha_s}\Delta\alpha_s \equiv K_{\alpha_s}^{M10}\Delta\alpha_s = SW_{\downarrow}^{TOA}T^2\Delta\alpha_s \quad (15)$$

255 where $SW_{\downarrow}^{TOA}$ is the local incoming solar flux at TOA, T is the local clearness index, and
256 $\partial SW_{\uparrow}^{TOA}/\partial\alpha_s$ is the approximated change in the upwelling shortwave flux at TOA due to a
257 change in the surface albedo.

258 The second candidate parameterization, originally proposed in Cherubini *et al*. (2012), makes
259 direct use of the solar flux incident at the surface $SW_{\downarrow}^{SFC}$ combined with a one-way
260 transmission constant k:

261 $$\frac{\partial SW_{\uparrow}^{TOA}}{\partial \alpha_s}\Delta\alpha_s \equiv K_{\alpha_s}^{C12}\Delta\alpha_s = SW_{\downarrow}^{SFC}k\Delta\alpha_s \quad (16)$$

262 where k is based on the global annual mean share of surface reflected shortwave radiation
263 exiting a clear-sky (Lacis and Hansen, 1974; Lenton and Vaughan, 2009) and is hence
264 temporally and spatially invariant. This value – or 0.85 -- is similar to the global mean ratio
265 of forward-to-total shortwave scattering reported in Iqbal (1983). Bright & Kvalevåg (2013)
266 evaluated Eq. (16) at several global locations and found large biases for some regions and
267 months, despite good overall performance globally (rRMSE = 7%; n = 120 months).

268 *d. Novel empirical parameterization*

To determine whether the GCM-based kernels could be approximated with sufficient fidelity using other simpler model formulations based on their own boundary data, we applied machine learning to identify potential model forms using GCM boundary fluxes as input. For the two GCMs kernels in which the GCM's own boundary fluxes are also made available (CAM5 and ECHAM6), we used machine learning to minimize the sum of squared residuals between the four shortwave boundary fluxes and the GCM kernel at the monthly time step. The reference dataset consisted of a random global sample of 200,000 (~50%) grid cells at native model resolution (97% and 32% of all cells for ECHAM6 and CAM5, respectively) of which 50% were used for training and 50% for validation. Models were identified using a form of genetic programming known as symbolic regression (Eureqa®; Nutonian Inc.; (Schmidt and Lipson, 2009, 2010)) which searches a wide space of model structures as constrained by user input. In our case, we allowed the model to include the operators (i.e., addition, subtraction, multiplication, division, sine, cosine, tangent, exponential, natural logarithm, factorial, power, square root), but numerical coefficients were forbidden. The model search was allowed to continue until the percent convergence and maturity metrics exceeded 98% and 50%, respectively, at which point more than 1×10^{11} formulae had been evaluated. A parsimonious solution was chosen by minimizing the error metric and model complexity using the Pareto front (Figure S1 of Supporting Information) (Smits and Kotanchek, 2005). Between CAM5 and ECHAM6, four common model solutions were found (Table S1 of Supporting Information). The best of these common solutions is subsequently referred to as $K_{\alpha_s}^{BO18}$ and is given as:

$$\frac{\partial SW_{\uparrow}^{TOA}}{\partial \alpha_s}\Delta\alpha_s = K_{\alpha_s}^{BO18}\Delta\alpha_s = SW_{\downarrow}^{SFC}\sqrt{T}\Delta\alpha_s \quad (17)$$

4. Kernel model evaluation

a. Initial candidate screening

The four GCM kernels presented in Section 2.b are employed as benchmarks to initially screen the six simple model candidates. We compute a skill metric analogous to the "relative error" metric used to evaluate GCMs by Anav et al. (2013) that takes into account error in the spatial pattern between a model and an observation. Because we have no true observational reference, our evaluation instead focuses on the disagreement or deviation between CERES and GCM kernels at the monthly time step. Given interannual climate variability in the earth system, the challenge of comparing the multi-year CERES kernel to a single-year GCM kernel can be partially overcome by averaging the four GCM kernels.

Using the multi-GCM mean as the reference, we first compute the absolute deviation $AD^X_{m,p}$ as:

$$AD^X_{m,p} = \left| CERES^X_{m,p} - \overline{GCM}_{m,p} \right| \tag{18}$$

where $CERES^X_{m,p}$ is the kernel for CERES model candidate x in month m and pixel p and $\overline{GCM}_{m,p}$ is the multi-GCM mean of the same pixel and month. $AD^X_{m,p}$ is then normalized to the maximum absolute deviation of all six CERES kernels for the same pixel and month to obtain a normalized absolute deviation, $NAD^X_{m,p}$, which is analogous to the "relative error" metric of Anav et al. (2013) having values ranging between 0 and 1:

$$NAD^X_{m,p} = 1 - \frac{AD^X_{m,p}}{\max(AD_{m,p})} \tag{19}$$

where $\max(AD_{m,p})$ is the maximum absolute deviation of all six CERES kernels at pixel p and month m.

CERES kernel ranking is based on the mean relative absolute deviation in both space and time – or $\overline{NAD}^{X}$:

$$\overline{NAD}^{X} = \frac{1}{M}\sum_{m=1}^{M}\frac{1}{P}\sum_{p=1}^{P} NAD_{m,p}^{X} \tag{20}$$

where M is the total number of months (i.e., 12) and P is the total number of grid cells.

b. GCM kernel emulation

In order to eliminate any bias related to differences in the atmospheric state embedded in the GCM kernel input climatologies, we emulate them by applying the candidate models (or parameterizations) using the original GCM boundary fluxes as input. Emulation is only done for two of GCM-based kernels since only two of them have provided the accompanying boundary fluxes needed to do so: ECHAM6 (Block and Mauritsen, 2014) and CAM5 (Pendergrass et al., 2018). Emulation enables a more critical evaluation of the functional form of the candidate models in relation to the more sophisticated radiative transfer schemes employed by ECHAM6 (Stevens et al., 2013) and CAM5 (Hurrell et al., 2013).

c. CACK model uncertainty

Following emulation, monthly GCM kernels are then regressed on the monthly kernels emulated with the leading model candidates. The model that best emulates both GCM kernels – as measured in terms of the mean coefficient of determination (R^2) and mean RMSE – is chosen to represent CACK.

Three sources of uncertainty are considered for CACK when based on the CERES boundary flux climatology (i.e., 2001-2016 monthly means): 1) *physical variability* 2) *data uncertainty*; and 3) *model error* (Mahadevan and Sarkar, 2009). The first is related to the interannual variability of Earth's atmospheric state and boundary radiative fluxes. The second is related

to the uncertainty of the CERES EBAF v4 variables used as input to CACK (including measurement error). The third source of uncertainty is the error related to CACK's model form. CACK's combined uncertainty for any given pixel and month is estimated as follows, where if CACK or y is some non-linear function of the CERES boundary inputs x_1 and x_2 that co-vary in time and space, then the combined uncertainty of y – or $\sigma(y)$ – may be expressed as the sum of the *model error* plus the combined *physical variability* and *data uncertainty* associated with x_1 and x_2 summed in quadrature (Breipohl, 1970; Clifford, 1973; Green et al., 2017):

$$\sigma(y) \approx \sigma_{ME}(y) + \sqrt{\left(\frac{\partial y}{\partial x_1}\right)^2 \left[\sigma_{PV}(x_1) + \sigma_{DU}(x_1)\right]^2 + \left(\frac{\partial y}{\partial x_2}\right)^2 \left[\sigma_{PV}(x_2) + \sigma_{DU}(x_2)\right]^2 + \sqrt{\left(2\frac{\partial y}{\partial x_1}\frac{\partial y}{\partial x_2}\sigma(x_1, x_2)\right)^2}} \quad (21)$$

where $\sigma_{PV}(x_1)$ and $\sigma_{PV}(x_2)$ are the standard deviations of the 16-yr. climatological record of CERES input variables x_1 and x_2, respectively, for a given grid cell and month, $\sigma_{DU}(x_1)$ and $\sigma_{DU}(x_2)$ are the absolute uncertainties of CERES input variables x_1 and x_2, respectively, for a given grid cell and month, $\sigma(x_1, x_2)$ is the covariance within the 16-yr. climatological record between CERES input variables x_1 and x_2 for a given month and grid cell, and σ_{ME} is the monthly grid cell model error. Model error ($\sigma_{ME}(y)$) and data uncertainties ($\sigma_{DU}(x_n)$) for any given grid cell and month are based on the relative RMSE (Supporting Information) and relative uncertainties of CERES boundary terms reported in Kato *et al.* (2018) (cf. Table 8, "Monthly gridded, Ocean + Land") and Loeb *et al.* (2017) (cf. Table 8, "All-sky, *Terra-Aqua* period"). For the model error, we take the mean relative RMSE of the machine learning model solutions for ECHAM5 and CAM5. For the relative uncertainty of the incoming solar flux at TOA ($SW_{\downarrow}^{TOA}$), we use the 1% "calibration uncertainty" reported in Loeb *et al.* (2017).

If CACK's intended application is to estimate a temporally-explicit ΔF within the CERES era (i.e., if temporally-explicit rather than the climatological mean CERES boundary fluxes are desired to compute CACK), the uncertainty related to *physical variability* ($\sigma_{PV}(x_n)$) can be dropped from Eq. (21).

d. Climatological CACK example application

To demonstrate CACK's application when based on monthly CERES EBAF climatology, including the handling of uncertainty, we estimate the annual mean ΔF from a $\Delta\alpha$ scenario associated with hypothetical deforestation in the tropics, where ΔF for a given month is estimated as Eq. (4) where K_{α_s} is the 2001-2016 monthly climatological CACK and $\Delta\alpha$ is the difference in the 2001-2011 monthly climatological mean white-sky surface albedo between "Croplands" (CRO) and "Evergreen broadleaved forests" (EBF) taken from Gao *et al*. (2014) which is based on International Geosphere-Biosphere Program definitions of land cover classification.

The monthly climatological albedo look-up maps of Gao *et al*. (2014) contain their own uncertainties, which we take as the mean absolute difference between the monthly albedos reconstructed using their look-up model and the monthly MODIS retrieval record (c.f. Table 3 in Gao *et al*. (2014)).

The total estimated uncertainty linked to the annual local (i.e., grid cell) instantaneous ΔF can thus be expressed (in W m^{-2}) as:

$$\sigma(\Delta F) = \frac{1}{12}\sum_{m=1}^{12}\left|\Delta F_m\right|\sqrt{\left(\frac{\sigma(K_{\alpha_s,m})}{K_{\alpha_s,m}}\right)^2+\left(\frac{\sigma(\Delta\alpha_{s,m})}{\Delta\alpha_{s,m}}\right)^2} \quad (22)$$

where $\sigma(K_{\alpha_s,m})/K_{\alpha_s,m}$ is the relative grid cell uncertainty of CACK and $\sigma(\Delta\alpha_{s,m})/\Delta\alpha_{s,m}$ is the relative uncertainty of $\Delta\alpha_s$ in month *m* defined as:

$$\frac{\sigma(\Delta\alpha_{s,m})}{\Delta\alpha_{s,m}} = \sqrt{\left(\frac{\sigma(\alpha_{s,m})}{\alpha_{CRO,m}}\right)^2 + \left(\frac{\sigma(\alpha_{s,m})}{\alpha_{EBF,m}}\right)^2} \quad (23)$$

where $\sigma(\alpha_{s,m})$ is the monthly absolute uncertainty of the climatological mean surface albedo (i.e., of the Gao *et al*. (2014) product).

e. Temporally-explicit CACK application example

Use of a temporally-explicit CACK may be desirable for time-sensitive applications within the CERES era. This is particularly true for regions experiencing significant changes to the atmospheric state affecting shortwave radiation transfer. A good example is in southern Amazonia where tropical deforestation has been linked to changes in cloud cover (Durieux et al., 2003; Lawrence and Vandecar, 2014; Wright et al., 2017). To exemplify this, we estimate the annual mean instantaneous ΔF for CERES grid cells in the region having experienced significant trends in both surface albedo and cloud area fraction during the 2001-2016 period. Grid cell trends in surface albedo and cloud area fraction are deemed significant if the slopes of linear fits obtained from local (i.e., grid cell) ordinary least squares regressions had p-values ≤ 0.05. We then apply the slope of the surface albedo trend to represent the monthly mean interannal $\Delta\alpha$ incurred over the time series together with CACK updated monthly to estimate the local annual mean instantaneous ΔF at each step in the series:

$$\Delta F(t) = \sum_{m=1}^{m=12} -K_{\alpha_s,m}(t)\Delta\alpha_s \quad (24)$$

where $K_{\alpha_s,m}(t)$ is the monthly CACK in year *t* of the time series. ΔF is then averaged across all grid cells in the sample, with the results then compared to the ΔF that is computed for the

same grid sample using the time-insensitive CAM5 and ECHAM6 kernels (i.e., $K_{\alpha_s,m} \neq f(t)$). Using the slope of the surface albedo trend as the $\Delta\alpha_s$ for all months and years rather than the actual $\Delta\alpha_{s,m}(t)$ (i.e., $\Delta\alpha_{s,m}(t) = \alpha_{s,m,t} - \alpha_{s,m,t-1}$) yields the same result when averaged over the full time period but allows us to isolate the effect of the changing atmospheric state on calculations of *ΔF*. We limit the *ΔF* uncertainty estimate to CACK's uncertainty that includes $\sigma_{DU}(x_n)$ and $\sigma_{ME}(x_n)$ but excludes $\sigma_{PV}(x_n)$.

5. Results

a. Initial performance screening

Seasonally, differences in latitude band means between the CERES kernel candidates and the multi-GCM mean kernels are shown in Figure 1.

< Figure 1 >

Qualitatively, starting with December-January-February (*DJF*), $K_{\alpha_s}^{BO18}$ gives the best agreement with $K_{\alpha_s}^{\overline{GCM}}$ with the exception of the zone around 55 – 65°S (-55 – -65°), where $K_{\alpha_s}^{QH06}$ gives slightly better agreement (Fig. 1A). In March-April-May (*MAM*), $K_{\alpha_s}^{BO18}$ appears to give the best overall agreement with the exception of the high Arctic, where $K_{\alpha_s}^{ANISO}$ and $K_{\alpha_s}^{C12}$ give better agreement, and with the exception of the zone around 60 – 65°S (-60 – -65°) where $K_{\alpha_s}^{QH06}$, $K_{\alpha_s}^{ANISO}$, and $K_{\alpha_s}^{C12}$ agree best with $K_{\alpha_s}^{\overline{GCM}}$ (Fig. 1B). The largest spread in disagreement across all six CERES kernels is found in June-July-August (*JJA*; Fig. 1 C) at northern high latitudes. $K_{\alpha_s}^{BO18}$ appears to agree best both here and elsewhere with the exception of the zone between ~20 – 35°N, where $K_{\alpha_s}^{QH06}$ gives slightly better agreement.

In September-October-November (*SON*), $K_{\alpha_s}^{BO18}$ agrees best with $K_{\alpha_s}^{\overline{GCM}}$ at all latitudes except the zone between 10 – 25°N and 55 – 65°S where $K_{\alpha_s}^{QH06}$ agrees slightly better.

Quantitatively, the proportion of the total variance explained by linear regressions of monthly $K_{\alpha_s}^{\overline{GCM}}$ on monthly $K_{\alpha_s}^{CERES}$ (i.e., "R^2") is highest and equal for the CERES kernels based on the ANISO, QH06, and BO18 models (Fig. 2 B, C, & D). Of these three, $K_{\alpha_s}^{QH06}$ has a y-intercept ("B_0") closest to 0 and a slope ("m") of 1, although the root mean squared error ("*RMSE*") – an accuracy measure – is slightly better (lower) for $K_{\alpha_s}^{BO18}$. The two CERES kernels with the lowest R^2, highest slopes (negative deviations), highest *RMSE*s, and y-intercepts with the largest absolute difference from zero – or the worst performing candidates – are those based on the ISO and M10 models (Fig. 2 A&E).

< Figure 2 >

Although the y-intercept deviation from 0 for $K_{\alpha_s}^{C12}$ is relatively low, its *RMSD* is ~50% higher than that of $K_{\alpha_s}^{QH06}$, $K_{\alpha_s}^{BO18}$, and $K_{\alpha_s}^{ANISO}$ and leads to notable positive deviation from the multi-GCM mean ($K_{\alpha_s}^{\overline{GCM}}$) judging by its slope of 0.92.

Globally, $\overline{NAD}$ for the QH06, ANISO, and BO18 kernels are far superior to the ISO, M10, and C12 kernels (Table 3).

< Table 3 >

After filtering to remove grid cells for oceans and other water bodies, $\overline{NAD}$ scores for these three kernels decreased; the decrease was smallest for $K_{\alpha_s}^{BO18}$ (-0.03) and largest for $K_{\alpha_s}^{QH06}$ (-

444 0.06). Despite constraining the analysis to land surfaces only, the rank order remained
445 unchanged (Table 3), and $K_{\alpha_s}^{QH06}$, $K_{\alpha_s}^{BO18}$, and $K_{\alpha_s}^{ANISO}$ are subjected to further evaluation.

446 *b. GCM kernel emulation and additional performance evaluation*

447 However, because the QH06 model ($K_{\alpha_s}^{QH06}$) required auxiliary inputs for cloud cover area
448 fraction and cloud optical depth – two atmospheric state variables not provided with the
449 ECHAM6 and CAM5 kernel datasets – it was not possible to emulate these two GCM kernels
450 with $K_{\alpha_s}^{QH06}$. Additional performance evaluation through GCM kernel emulation is therefore
451 restricted to the ANISO and BO18 models.

452 < Figure 3 >

453 Globally, the kernel based on the ANISO model displays larger annual mean biases relative to
454 BO18 when compared to both ECHAM6 and CAM5 kernels (Figure 3). Notable positive
455 biases over land with respect to both ECHAM6 and CAM5 kernels are evident in the northern
456 Andes region of South America, the Tibetan plateau, and the tropical island region comprising
457 Indonesia, Malaysia, and Papua New Guinea (Fig. 3 A & C). Notable negative biases over
458 land with respect to both ECHAM6 and CAM5 kernels are evident over Greenland,
459 Antarctica, northeastern Africa, and the Arabian Peninsula (Fig. 3 A & C).

460 < Figure 4 >

461 Globally, annual biases for BO18 are generally found to be lower than for ANISO and are
462 mostly non-existent in extra-tropical ocean regions (Fig. 3 B & D). Patterns in biases over
463 land are mostly negative with the exception of Saharan Africa where the annual mean bias
464 with respect to both GCMs is positive. For BO18, systematic positive biases – or biases
465 evident with respect to both GCM kernels – appear over eastern tropical and subtropical

marine coastal upwelling zones where marine stratocumulus cloud dynamics are difficult for GCMs to resolve (Bretherton et al., 2004; Richter, 2015).

< Table 4 >

Regression statistics (Figure 4) indicate a greater overall performance for BO18 than for ANISO. RMSEs for monthly kernels emulated with BO18 are 9.0 and 8.2 W m^{-2} for CAM5 and ECHAM6, respectively – which is ~50-60% of the RMSEs emulated with the ANISO model. Relative to ANISO, the BO18 model also gives a higher R^2, a slope closer to 1, and a y-intercept closer to zero (Figure 4). The BO18 model (or parameterization) is therefore selected for the CERES albedo change kernel (CACK).

Focusing only on the GCM kernels emulated with $K_{\alpha_s}^{BO18}$ henceforth, negative biases are evident in all months (Table 4), with the largest biases (in magnitude) appearing in May (-4.4 W m^{-2}) and November (-2.5 W m^{-2}) for CAM5 and ECHAM6, respectively. In absolute terms, largest biases of 8.6 W m^{-2} and 6.8 W m^{-2} appear in June for CAM5 and ECHAM6, respectively. Annually, the mean absolute bias for CAM5 and ECHAM6 is 6.8 and 6.1 W m^{-2}, respectively – a magnitude which seems remarkably low if one compares this to the annual mean disagreement (standard deviation) of 33 W m^{-2} across all four GCM kernels (not shown; for seasonal mean standard deviations see Fig. 1).

c. CACK uncertainty

For a kernel based on 2001-2016 monthly mean CERES EBAF climatology, Figure 5 illustrates the contribution of the absolute error related to $K_{\alpha_s}^{BO18}$'s model form (Fig. 5 A, annual mean) relative to CACK's total absolute uncertainty (Fig. 5 C, annual mean), which includes the uncertainty surrounding CERES EBAF v4 input variables $SW_{\downarrow}^{SFC}$ and $SW_{\downarrow}^{TOA}$ and their interannual variability (Fig. 5 B, annual mean).

< Figure 5 >

Total propagated σ_{pv} and σ_{du} far exceeds σ_{me}, is dominated by $\sigma_{du}(SW_{\downarrow}^{SFC})$ and $\sigma_{pv}(SW_{\downarrow}^{SFC})$, and is largest in the Pacific region to the south of the intertropical convergence zone (ITCZ). Over land, the annual σ_{pv} and σ_{du} as well as the annual σ_{total} are generally largest in arid or high altitude regions (Fig. 5 B). However, annual CACK values are also large in these regions reducing the relative uncertainty (Fig. 5 D). The largest relative uncertainties over land (on an annual basis) – which can approach 50% – are found over central Europe, northwestern Asia, southeastern China, Andean Chile, and northwestern N. America (Fig. 5 D).

d. Climatological CACK application

When estimated with a CACK based on monthly CERES EBAF climatology, the annual *ΔF* from $\Delta\alpha_s$ linked to hypothetical deforestation in the tropics is negative in most regions, approaching -20 W m^{-2} locally in some regions of the Brazilian Cerrado and south of the Sahel region in Africa (Fig. 6 B). The combined CACK and $\Delta\alpha_s$ uncertainty for these regions can approach ± 5 W m^{-2} annually (Fig. 6 C) in regions like the Brazilian Cerrado and sub-Sahel Africa. Relative to the *ΔF* magnitude, however, the largest uncertainties (annual) may be found in the subtropical regions of Central America, southern Brazil, southern Asia, and northern Australia, where it can approach 30-40% (Fig. 6 D).

e. Temporally-explicit CACK application

The effect of a decreasing cloud cover trend in southern Amazonia (Fig. 7 B) on shortwave radiative transfer and thus a CACK-based estimate of regional mean annual *ΔF* emerges in Figure 7 C, where *ΔF* increases in magnitude by 0.004 W m^{-2} from 2002 to 2016. This *ΔF*

trend would otherwise go undetected if a GCM-based kernel were applied to the same surface albedo trend – that is, to a sustained positive interannual monthly albedo change "pulse". Alternatively, a CACK based on 2001 CERES EBAF inputs (applied with $\Delta\alpha_s$ for 2001-2002) would give slightly higher ΔF estimates relative to those based on ECHAM6 and CAM5 kernels; conversely, a CACK based on 2015 CERES EBAF inputs (applied with $\Delta\alpha_s$ for 2015-2016) that would yield lower ΔF estimates relative to those based on the same two GCM-based kernels (Fig. 7 C). Use of temporally-explicit CACK can therefore capture ΔF trends related to a changing atmospheric state that fixed-state GCM kernels are unable to capture.

5. Discussion

Motivated by an increasing abundance of climate impact research focusing on land processes in recent years, we comprehensively evaluated six simplified models (or parameterizations) as candidates for an albedo change kernel based on the CERES EBAF v4 products (Kato et al., 2018; Loeb et al., 2017). Relative to albedo change kernels based on sophisticated radiative transfer schemes embedded in GCMs, a CERES-based albedo change kernel – or CACK – represents a more transparent and empirically-rooted alternative that can be updated frequently at relatively low cost. This allows greater flexibility to meet the needs of research focusing on surface albedo trends within the CERES era in regions currently undergoing rapid changes to atmospheric state as it affects shortwave radiation transfer. Although some modeling groups have provided recent updates to their albedo change kernels using the latest GCM versions (e.g., (Pendergrass et al., 2018)), the atmospheric state conditions used to derive them may still be considered outdated or not in sync with that required for many applications (Table 1).

Based on both qualitative and quantitative benchmarking against the mean of four GCM kernels, the novel kernel parameterization obtained from machine learning $K_{\alpha_s}^{BO18}$, together with the two (semi-)analytically derived kernels $K_{\alpha_s}^{QH06}$ and $K_{\alpha_s}^{ANISO}$, proved far superior to the $K_{\alpha_s}^{ISO}$ analytical kernel and to the two additional empirical parameterizations $K_{\alpha_s}^{C12}$ and $K_{\alpha_s}^{M10}$. When subjected to additional performance evaluation, however, we found that $K_{\alpha_s}^{BO18}$ was able to more robustly emulate two GCM kernels (ECHAM6 and CAM5) with exceptionally high agreement, suggesting that $K_{\alpha_s}^{BO18}$ could serve as a suitable candidate for CACK.

Relative to the monthly CAM5 and ECHAM6 kernels, the mean absolute monthly emulation "error" of $K_{\alpha_s}^{BO18}$ was found to be 6.8 and 6.1 W m^{-2}, respectively – a magnitude which is only ~20% of the standard deviation found across four GCM kernels (annual mean). CACK's remarkable simplicity lends support to the idea of using machine learning to explore and detect emergent properties of radiative transfer or other complex, interactive model outputs in future research. The fact that the $K_{\alpha_s}^{BO18}$ parameterization emerged as the best common solution from two independently executed machine learning analyses each employing a random sampling unique to a specific GCM kernel suggests that the $K_{\alpha_s}^{BO18}$ parameterization is robust and insensitive to the underlying GCM representation of shortwave radiative transfer.

Despite its stronger empirical foundation over a GCM-based kernel, it is important to recognize CACK's limitations. Firstly, while CACK has a finer spatial resolution than most GCM kernels, it still represents a spatially averaged response rather than a truly local response; in other words, the state variables used to define the $SW_{\uparrow}^{TOA}$ response are averages tied to the coarse spatial (i.e., 1° x 1°) resolution of the CERES EBAF v4 product grids. Secondly, the monthly CERES EBAF-Surface product used to define lower atmospheric

boundary conditions is not strictly an observation. The space-borne platform is not able to directly observe surface irradiances, requiring additional satellite-based estimates of cloud and aerosol properties as input to a radiative transfer model (Kato et al., 2012). Although TOA irradiances are applied to constrain the surface irradiances, they remain susceptible to errors in the radiative transfer model inputs. Considering this error as "data uncertainty" increases CACK's overall uncertainty beyond that which is related to its underlying parameterization or "model error". The uncertainty of CERES surface shortwave irradiances as well as extensive ground validation and testing are documented in greater detail elsewhere (Kato et al., 2013; Kato et al., 2018; Loeb et al., 2017; Loeb et al., 2009) and may continue to be reduced in future EBAF-Surface versions.

a. Concluding remarks

To conclude, we developed, evaluated, and proposed a radiative kernel for surface albedo change based on CERES EBAF v4 products – or CACK. Relative to existing kernels based on GCMs, CACK provides a higher spatial resolution, higher transparency alternative that is more amenable to user needs. For LULCC research of the near-past, present day, or near-future periods, application of a CACK whose inputs are based on monthly climatological means of the full CERES EBAF record can better-account for the corresponding interannual variability in Earth's atmospheric state affecting shortwave radiative transfer. For regions undergoing changes in atmospheric state that are detectable above the normal variability within the CERES era, application of a temporally-explicit CACK can better-account for its influence on ΔF estimates from surface albedo change. CACK's input flexibility and transparency combined with documented uncertainty make it well-suited to be applied as part of a Monitoring, Reporting, and Verification (MRV) framework for biogeophysical impacts on land, analogous to those which currently exist for land sector greenhouse gas emissions.

Code and Dataset Availability

We make both monthly temporally-explicit and monthly climatological mean CACKs for years 2001-2016 available as a complete data product ("CACKv1.0"; netCDF file available at doi:10.6073/pasta/d77b84b11be99ed4d5376d77fe0043d8) that includes their respective uncertainty layers. A summary of this dataset and associated variables is provided in Table S3 of the Supporting Information. Octave script files for generating monthly CACK and demonstrating its application with user-specified temporal and spatial extents are bundled with the netCDF file.

Data Availability

CERES EBAF data are available for download at: https://ceres.larc.nasa.gov/products.php?product=EBAF-TOA . The CAM3 kernel is available at: http://people.oregonstate.edu/~shellk/kernel.html . The CAM5 kernel is available at: https://www.earthsystemgrid.org/ac/guest/secure/sso.html . The ECHAM5 kernel is available at: https://swiftbrowser.dkrz.de/public/dkrz_0c07783a-0bdc-4d5e-9f3b-c1b86fac060d/Radiative_kernels/ .

Acknowledgements

R.M.B. was supported by the Research Council of Norway, grants #244074/E20 and #250113/F20; T.L.O. was supported by the Climate and Land Use program award #2017-68002-26612 of the USDA National Institute of Food and Agriculture.

606 **References**

607 Anav, A., Friedlingstein, P., Kidston, M., Bopp, L., Ciais, P., Cox, P., Jones, C., Jung, M., Myneni, R.,
608 and Zhu, Z.: Evaluating the Land and Ocean Components of the Global Carbon Cycle in the
609 CMIP5 Earth System Models, Journal of Climate, 26, 6801-6843, 2013.
610
611 Atwood, A. R., Wu, E., Frierson, D. M. W., Battisti, D. S., and Sachs, J. P.: Quantifying Climate
612 Forcings and Feedbacks over the Last Millennium in the CMIP5–PMIP3 Models, Journal of
613 Climate, 29, 1161-1178, 2016.
614
615 Block, K. and Mauritsen, T.: Forcing and feedback in the MPI-ESM-LR coupled model under abruptly
616 quadrupled CO2, Journal of Advances in Modeling Earth Systems, 5, 676-691, 2014.
617
618 Bonan, G. B., Pollard, D., and Thompson, S. L.: Effects of Boreal Forest Vegetation on Global
619 Climate, Nature, 359, 716-718, 1992.
620
621 Bozzi, E., Genesio, L., Toscano, P., Pieri, M., and Miglietta, F.: Mimicking biochar-albedo feedback
622 in complex Mediterranean agricultural landscapes, Environmental Research Letters, 10, 084014,
623 2015.
624
625 Breipohl, A. M.: Probabilistic systems analysis: an introduction to probabilistic models, decisions,
626 and applications of random processes, Wiley, New York, 1970.
627
628 Bretherton, C. S., Uttal, T., Fairall, C. W., Yuter, S. E., Weller, R. A., Baumgardner, D., Comstock,
629 K., Wood, R., and Raga, G. B.: The Epic 2001 Stratocumulus Study, Bulletin of the American
630 Meteorological Society, 85, 967-978, 2004.
631
632 Bright, R. M.: Metrics for Biogeophysical Climate Forcings from Land Use and Land Cover Changes
633 and Their Inclusion in Life Cycle Assessment: A Critical Review, Environmental Science &
634 Technology, 49, 3291-3303, 2015.
635
636 Bright, R. M. and Kvalevåg, M. M.: Technical note: Evaluating a simple parameterization of radiative
637 shortwave forcing from surface albedo change, Atmospheric Chemistry and Physics, 13, 11169-
638 11174, 2013.
639
640 Caiazzo, F., Malina, R., Staples, M. D., Wolfe, P., J. ,, Yim, S. H. L., and Barrett, S. R. H.:
641 Quantifying the climate impacts of albedo changes due to biofuel production: a comparison with
642 biogeochemical effects, Environmental Research Letters, 9, 024015, 2014.
643
644 Carrer, D., Pique, G., Ferlicoq, M., Ceamanos, X., and Ceschia, E.: What is the potential of cropland
645 albedo management in the fight against global warming? A case study based on the use of cover
646 crops, Environmental Research Letters, 13, 044030, 2018.
647
648 CERES Science Team: CERES EBAF-Surface Edition 4.0. NASA Atmospheric Science and Data
649 Center (ASDC). https://doi.org/10.5067/TERRA+AQUA/CERES/EBAF-SURFACE_L3B004.0 .
650 Accessed January 14, 2018., 2018a.
651
652 CERES Science Team: CERES EBAF-TOA Edition 4.0. NASA Atmospheric Science and Data
653 Center (ASDC). https://doi.org/10.5067/TERRA+AQUA/CERES/EBAF-TOA_L3B004.0 . Accessed
654 January 14, 2018. . 2018b.
655
656 Cherubini, F., Bright, R. M., and Strømman, A. H.: Site-specific global warming potentials of biogenic
657 CO2 for bioenergy: contributions from carbon fluxes and albedo dynamics, Environmental
658 Research Letters, 7, 045902, 2012.

659

660 Clifford, A. A.: Multivariate error analysis: A handbook of error propagation and calculation in many-
661 parameter systems, Applied Science Publishers, London, U. K., 1973.
662
663 Collins, W. D., Rasch, P. J., Boville, B. A., Hack, J. J., McCaa, J. R., Williamson, D. L., Briegleb, B.
664 P., Bitz, C. M., Lin, S.-J., and Zhang, M.: The Formulation and Atmospheric Simulation of the
665 Community Atmosphere Model Version 3 (CAM3), Journal of Climate, 19, 2144-2161, 2006.
666
667 Dickinson, R. E. and Henderson-Sellers, A.: Modelling tropical deforestation: A study of GCM land-
668 surface parametrizations, Quarterly Journal of the Royal Meteorological Society, 114, 439-462,
669 1988.
670
671 Dolinar, E. K., Dong, X., Xi, B., Jiang, J. H., and Su, H.: Evaluation of CMIP5 simulated clouds and
672 TOA radiation budgets using NASA satellite observations, Clim. Dyn., 44, 2229-2247, 2015.
673
674 Donohoe, A. and Battisti, D. S.: Atmospheric and Surface Contributions to Planetary Albedo, Journal
675 of Climate, 24, 4402-4418, 2011.
676
677 Durieux, L., Machado, L. A. T., and Laurent, H.: The impact of deforestation on cloud cover over the
678 Amazon arc of deforestation, Remote Sensing of Environment, 86, 132-140, 2003.
679 Free, M. and Sun, B.: Trends in U.S. Total Cloud Cover from a Homogeneity-Adjusted Dataset,
680 Journal of Climate, 27, 4959-4969, 2014.
681
682 Gao, F., He, T., Wang, Z., Ghimire, B., Shuai, Y., Masek, J., Schaaf, C., and Williams, C.: Multi-scale
683 climatological albedo look-up maps derived from MODIS BRDF/albedo products, Journal of
684 Applied Remote Sensing, 8, 2014.
685
686 Ghimire, B., Williams, C. A., Masek, J., Gao, F., Wang, Z., Schaaf, C., and He, T.: Global albedo
687 change and radiative cooling from anthropogenic land cover change, 1700 to 2005 based on
688 MODIS, land use harmonization, radiative kernels, and reanalysis, Geophysical Research Letters,
689 41, 9087-9096, 2014.
690
691 Green, P., Gardiner, T., Medland, D., and Cimini, D.: WP2: Guide to uncertainty in measurement and
692 its nomenclature. Version 4.0. , U.K., 212 pp., 2017.
693
694 Hurrell, J. W., Holland, M. M., Gent, P. R., Ghan, S., Kay, J. E., Kushner, P. J., Lamarque, J. F.,
695 Large, W. G., Lawrence, D., Lindsay, K., Lipscomb, W. H., Long, M. C., Mahowald, N., Marsh,
696 D. R., Neale, R. B.,
697 Rasch, P., Vavrus, S., Vertenstein, M., Bader, D., Collins, W. D., Hack, J. J., Kiehl, J., and Marshall,
698 S.: The Community Earth System Model: A Framework for Collaborative Research, Bulletin of
699 the American Meteorological Society, 94, 1339-1360, 2013.
700
701 Iqbal, M.: An introduction to solar radiation, Academic Press Canada, Ontario, CA, 1983.
702
703 Jones, A. D., Calvin, K. V., Collins, W. D., and Edmonds, J.: Accounting for radiative forcing from
704 albedo change in future global land-use scenarios, Climatic Change, 131, 691-703, 2015.
705
706 Kashimura, H., Abe, M., Watanabe, S., Sekiya, T., Ji, D., Moore, J. C., Cole, J. N. S., and Kravitz, B.:
707 Shortwave radiative forcing, rapid adjustment, and feedback to the surface by sulfate
708 geoengineering: analysis of the Geoengineering Model Intercomparison Project G4 scenario,
709 Atmos. Chem. Phys., 17, 3339-3356, 2017.
710 Kato, S., Loeb, N. G., Rose, F. G., Doelling, D. R., Rutan, D. A., Caldwell, T. E., Yu, L., and Weller,
711 R. A.: Surface Irradiances Consistent with CERES-Derived Top-of-Atmosphere Shortwave and
712 Longwave Irradiances, Journal of Climate, 26, 2719-2740, 2012.
713

Kato, S., Loeb, N. G., Rose, F. G., Doelling, D. R., Rutan, D. A., Caldwell, T. E., Yu, L., and Weller, R. A.: Surface irradiances consistent with CERES-derived top-of-atmosphere shortwave and longwave irradiances, Journal of Climate, 26, 2719-2740, 2013.

Kato, S., Rose, F. G., Rutan, D. A., Thorsen, T. J., Loeb, N. G., Doelling, D. R., Huang, X., Smith, W. L., Su, W., and Ham, S.-H.: Surface Irradiances of Edition 4.0 Clouds and the Earth's Radiant Energy System (CERES) Energy Balanced and Filled (EBAF) Data Product, Journal of Climate, 31, 4501-4527, 2018.

Lacis, A. A. and Hansen, J. E.: A parameterization for the absorption of solar radiation in the earth's atmosphere, Journal of Atmospheric Sciences, 31, 118-133, 1974.

Lawrence, D. and Vandecar, K.: Effects of tropical deforestation on climate and agriculture, Nature Climate Change, 5, 27, 2014.

Lenton, T. M. and Vaughan, N. E.: The radiative forcing potential of different climate geoengineering options, Atmospheric Chemistry and Physics 9, 5539-5561, 2009.

Li, J. L. F., Waliser, D. E., Stephens, G., Lee, S., L'Ecuyer, T., Kato, S., Loeb, N., and Ma, H.-Y.: Characterizing and understanding radiation budget biases in CMIP3/CMIP5 GCMs, contemporary GCM, and reanalysis, Journal of Geophysical Research: Atmospheres, 118, 8166-8184, 2013.

Loeb, N. G., Doelling, D. R., Wang, H., Su, W., Nguyen, C., Corbett, J. G., Liang, L., Mitrescu, C., Rose, F. G., and Kato, S.: Clouds and the Earth's Radiant Energy System (CERES) Energy Balanced and Filled (EBAF) Top-of-Atmosphere (TOA) Edition-4.0 Data Product, Journal of Climate, 31, 895-918, 2017.

Loeb, N. G., Wielicki, B. A., Doelling, D. R., Smith, G. L., Keyes, D. F., Kato, S., Manalo-Smith, N., and Wong, T.: Toward optimal closure of the Earth's top-of-atmosphere radiation budget, Journal of Climate, 22, 748-766, 2009.

Lutz, D. A., Burakowski, E. A., Murphy, M. B., Borsuk, M. E., Niemiec, R. M., and Howarth, R. B.: Tradeoffs between three forest ecosystem services across the state of New Hampshire, USA: timber, carbon, and albedo, Ecological Applications, 26, 146-161, 2015.

Lutz, D. A. and Howarth, R. B.: The price of snow: albedo valuation and a case study for forest management, Environmental Research Letters, 10, 064013, 2015.

Mahadevan, S. and Sarkar, S.: Uncertainty analysis methods, U.S. Department of Energy, Washington, D.C., USA, 32 pp., 2009.

Muñoz, I., Campra, P., and Fernández-Alba, A. R.: Including CO2-emission equivalence of changes in land surface albedo in life cycle assessment. Methodology and case study on greenhouse agriculture, International Journal of Life Cycle Assessment, 15, 672-681, 2010.

O'Halloran, T. L., Law, B. E., Goulden, M. L., Wang, Z., Barr, J. G., Schaaf, C., Brown, M., Fuentes, J. D., Göckede, M., Black, A., and Engel, V.: Radiative forcing of natural forest disturbances, Global Change Biology, 18, 555-565, 2012.

Pendergrass, A. G., Conley, A., and Vitt, F. M.: Surface and top-of-atmosphere radiative feedback kernels for CESM-CAM5, Earth Syst. Sci. Data, 10, 317-324, 2018.

Qu, X. and Hall, A.: Assessing Snow Albedo Feedback in Simulated Climate Change, Journal of Climate, 19, 2617-2630, 2006.

768 Randerson, J. T., Liu, H., Flanner, M. G., Chambers, S. D., Jin, Y., Hess, P. G., Pfister, G., Mack, M.
769 C., Treseder, K. K., Welp, L. R., Chapin, F. S., Harden, J. W., Goulden, M. L., Lyons, E., Neff, J.
770 C., Schuur, E. A. G., and Zender, C. S.: The Impact of Boreal Forest Fire on Climate Warming,
771 Science, 314, 1130-1132, 2006.
772
773 Rasool, S. I. and Schneider, S. H.: Atmospheric Carbon Dioxide and Aerosols: Effects of Large
774 Increases on Global Climate, Science, 173, 138-141, 1971.
775
776 Richter, I.: Climate model biases in the eastern tropical oceans: causes, impacts and ways forward,
777 Wiley Interdisciplinary Reviews: Climate Change, 6, 345-358, 2015.
778
779 Schmidt, M. and Lipson, H.: Distilling free-form natural laws from experimental data, Science, 324,
780 81-85, 2009.
781
782 Schmidt, M. and Lipson, H.: Symbolic regression of implicit equations. In: Genetic Programming
783 Theory and Practice VII, Springer, 2010.
784
785 Shell, K. M., Kiehl, J. T., and Shields, C. A.: Using the Radiative Kernel Technique to Calculate
786 Climate Feedbacks in NCAR's Community Atmospheric Model, Journal of Climate, 21, 2269-
787 2282, 2008.
788
789 Smits, G. F. and Kotanchek, M.: Pareto-front exploitation in symbolic regression. In: Genetic
790 programming theory and practice II, Springer, 2005.
791
792 Soden, B. J., Held, I. M., Colman, R., Shell, K. M., Kiehl, J. T., and Shields, C. A.: Quantifying
793 Climate Feedbacks Using Radiative Kernels, Journal of Climate, 21, 3504-3520, 2008.
794
795 Srivastava, R.: Trends in aerosol optical properties over South Asia, International Journal of
796 Climatology, 37, 371-380, 2017.
797
798 Stephens, G. L., O'Brien, D., Webster, P. J., Pilewski, P., Kato, S., and Li, J.-l.: The albedo of Earth,
799 Reviews of Geophysics, 53, 141-163, 2015.
800
801 Stevens, B., Giorgetta, M., Esch, M., Mauritsen, T., Crueger, T., Rast, S., Salzmann, M., Schmidt, H.,
802 Bader, J., Block, K., Brokopf, R., Fast, I., Kinne, S., Kornblueh, L., Lohmann, U., Pincus, R.,
803 Reichler, T., and Roeckner, E.: Atmospheric component of the MPI-M Earth System Model:
804 ECHAM6, Journal of Advances in Modeling Earth Systems, 5, 146-172, 2013.
805
806 Taylor, K. E., Crucifix, M., Braconnot, P., Hewitt, C. D., Doutriaux, C., Broccoli, A. J., Mitchell, J. F.
807 B., and Webb, M. J.: Estimating Shortwave Radiative Forcing and Response in Climate Models,
808 Journal of Climate, 20, 2530-2543, 2007.
809
810 The GFDL Global Atmospheric Model Development Team: The New GFDL Global Atmosphere and
811 Land Model AM2–LM2: Evaluation with Prescribed SST Simulations, Journal of Climate, 17,
812 4641-4673, 2004.
813
814 Vanderhoof, M., Williams, C. A., Ghimire, B., and Rogan, J.: Impact of mountain pine beetle
815 outbreaks on forest albedo and radiative forcing, as derived from Moderate Resolution Imaging
816 Spectroradiometer, Rocky Mountains, USA, Journal of Geophysical Research: Biogeosciences,
817 118, 1461-1471, 2013.
818
819 Wang, H. and Su, W.: Evaluating and understanding top of the atmosphere cloud radiative effects in
820 Intergovernmental Panel on Climate Change (IPCC) Fifth Assessment Report (AR5) Coupled
821 Model Intercomparison Project Phase 5 (CMIP5) models using satellite observations, Journal of
822 Geophysical Research: Atmospheres, 118, 683-699, 2013.

Winton, M.: Simple optical models for diagnosing surface-atmosphere shortwave interactions, Journal of Climate, 18, 3796-3806, 2005.

Winton, M.: Surface Albedo Feedback Estimates for the AR4 Climate Models, Journal of Climate, 19, 359-365, 2006.

Wright, J. S., Fu, R., Worden, J. R., Chakraborty, S., Clinton, N. E., Risi, C., Sun, Y., and Yin, L.: Rainforest-initiated wet season onset over the southern Amazon, Proceedings of the National Academy of Sciences, doi: 10.1073/pnas.1621516114, 2017. 201621516, 2017.

Zhao, D., Xin, J., Gong, C., Wang, X., Ma, Y., and Ma, Y.: Trends of Aerosol Optical Properties over the Heavy Industrial Zone of Northeastern Asia in the Past Decade (2004–15), Journal of the Atmospheric Sciences, 75, 1741-1754, 2018.

838 **Table 1.** Attributes of existing GCM kernels, all of which having a monthly temporal
839 resolution.

Kernel	Base climatology extent	Base climatology period	Shortwave Radiative transfer	Horizontal Resolution	References
ECHAM6	1,000 years	Preindustrial*	RRTM-G	1.88° × 1.88°	(Block and Mauritsen, 2014; Stevens et al., 2013)
CAM3	6 years	1995-2000	δ-Eddington	1.4° × 1.4°	(Collins et al., 2006; Shell et al., 2008)
CAM5	1 year	2006-2007	RRTM-G	0.94° × 1.25°	(Pendergrass et al., 2018)
GFDL	17 years	1979-1995	Exponential sum-fits, 18 bands	2° × 2.5°	(Soden et al., 2008; The GFDL Global Atmospheric Model Development Team, 2004)

840 *Atmospheric CO_2 concentration = 284.7 ppmv; Exact time period unknown

841

842

Table 2. Definition of CERES input variables and other system optical properties derived from CERES inputs. All variables have a monthly temporal resolution and a spatial resolution of 1° × 1°.

CERES EBAF v.4 Shortwave Boundary Fluxes		
$SW_{\downarrow}^{TOA}$	Downwelling solar flux at top-of-atmosphere	Wm^{-2}
$SW_{\downarrow}^{SFC}$	Downwelling solar flux at surface	Wm^{-2}
$SW_{\downarrow,CLR}^{SFC}$	Clear-sky downwelling solar flux at surface	Wm^{-2}
$SW_{\uparrow}^{TOA}$	Upwelling solar flux at top-of-atmosphere	Wm^{-2}
$SW_{\uparrow}^{SFC}$	Upwelling solar flux at surface	Wm^{-2}
System Optical Properties		
$T = SW_{\downarrow}^{SFC} / SW_{\downarrow}^{TOA}$	Clearness index	unitless
$\alpha_p = SW_{\uparrow}^{TOA} / SW_{\downarrow}^{TOA}$	Planetary albedo	unitless
$\alpha_s = SW_{\uparrow}^{SFC} / SW_{\downarrow}^{SFC}$	Surface albedo	unitless
$A_p = 1 - \alpha_p$	Effective planetary absorption	unitless
$A_s = \left[SW_{\downarrow}^{SFC} - SW_{\uparrow}^{SFC} \right] / SW_{\downarrow}^{TOA}$	Effective surface absorption	unitless
$A_a = A_p - A_s$	Effective atmospheric absorption	unitless
$T_a = 1 - A_a$	Effective atmospheric transmission	unitless
$T_{a,CLR} = 1 - A_{a,CLR}$	Clear-sky effective atmospheric transmission	unitless
τ	Cloud visible optical depth	unitless
c	Cloud area fraction	fraction

Table 3. Normalized absolute deviation and CERES kernel model candidate ranking.

	Global		Land only		
	Δ_{NAD}	Rank	Δ_{NAD}	Rank	Mean Rank
ISO	0.05	6	0.05	6	*6*
ANISO	0.64	3	0.59	3	*3*
C12	0.45	4	0.47	4	*4*
M10	0.26	5	0.34	5	*5*
QH06	0.66	2	0.60	2	*2*
BO18	0.67	1	0.64	1	*1*

Table 4. Global monthly mean bias (*MB*) and mean absolute bias (*MAB*) for K_α^{BO18} emulated with T and $SW_\downarrow^{SFC}$ from ECHAM6 and CAM5. For reference, the global mean value of K_α^{BO18} is 133 W m^{-2}.

	MB (W m^{-2})												
	Jan.	**Feb.**	**Mar.**	**Apr.**	**May**	**Jun.**	**Jul.**	**Aug.**	**Sep.**	**Oct.**	**Nov.**	**Dec.**	**Ann.**
$K_\alpha^{BO18} - K_\alpha^{CAM5}$	-2.9	-3.4	-3.3	-3.9	-4.4	-3.8	-3.8	-3.7	-3.4	-3.8	-3.7	-3.3	-3.6
$K_\alpha^{BO18} - K_\alpha^{ECHAM6}$	-1.9	-2.2	-1.8	-1.9	-2.2	-1.5	-1.1	-1.6	-1.7	-2.5	-2.5	-1.8	-1.9
	MAB (W m^{-2})												
	Jan.	**Feb.**	**Mar.**	**Apr.**	**May**	**Jun.**	**Jul.**	**Aug.**	**Sep.**	**Oct.**	**Nov.**	**Dec.**	**Ann.**
$\lvert K_\alpha^{BO18} - K_\alpha^{CAM5} \rvert$	6.9	5.7	5.2	6.8	7.7	8.6	7.9	6.7	5.6	6.1	6.9	6.9	6.8
$\lvert K_\alpha^{BO18} - K_\alpha^{ECHAM6} \rvert$	6.3	5.7	5.0	5.9	6.7	6.8	6.4	5.8	5.3	5.6	6.4	6.7	6.1

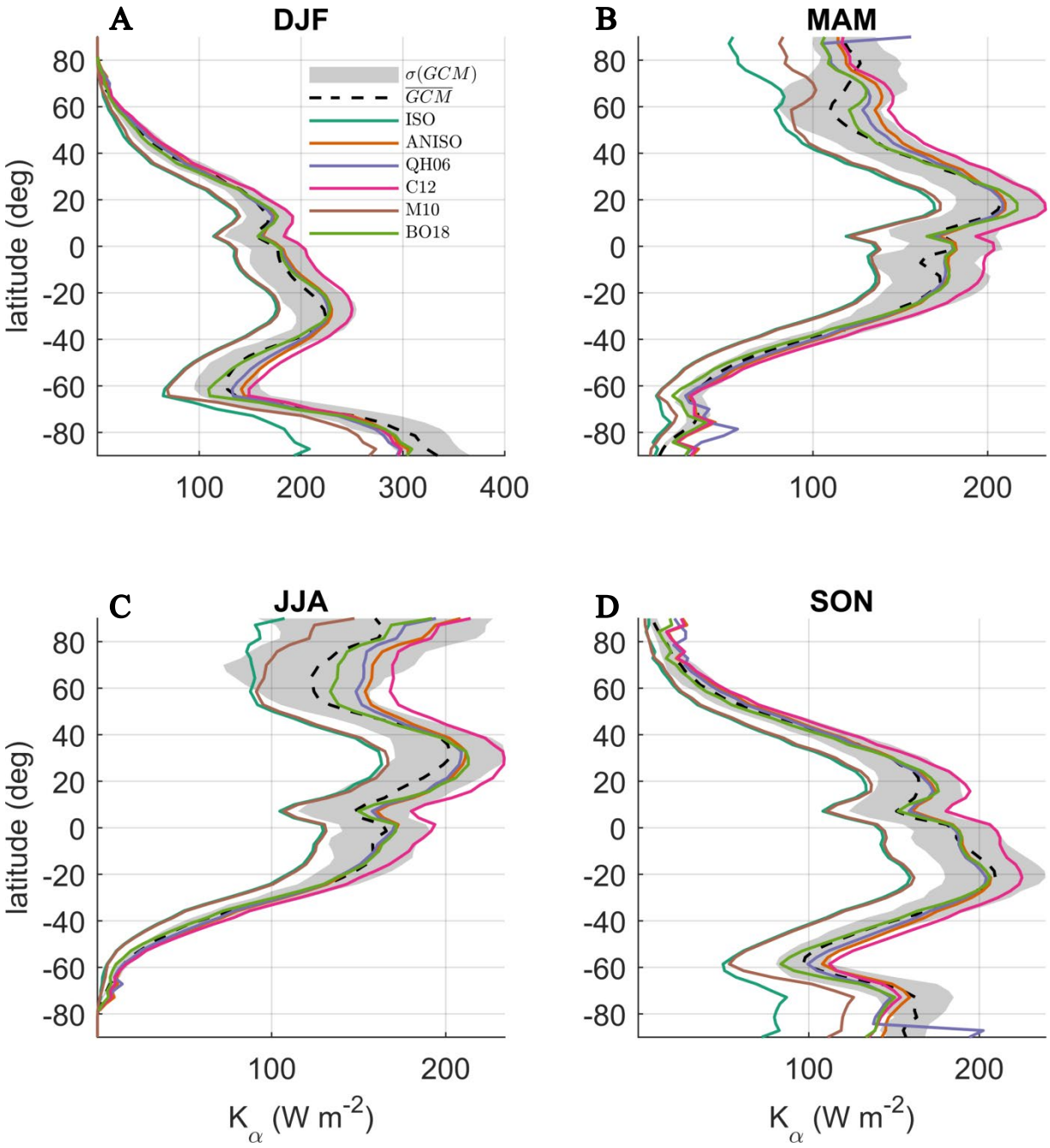

852

853 **Figure 1.** Latitudinal (1°) and seasonal means of the multi-GCM mean ($K_\alpha^{\overline{GCM}}$) and CACK

854 model candidates for: A) December-January-February (DJF); B) March-April-May (MAM);

855 C) June-July-August (JJA); D) September-October-November (SON).

856

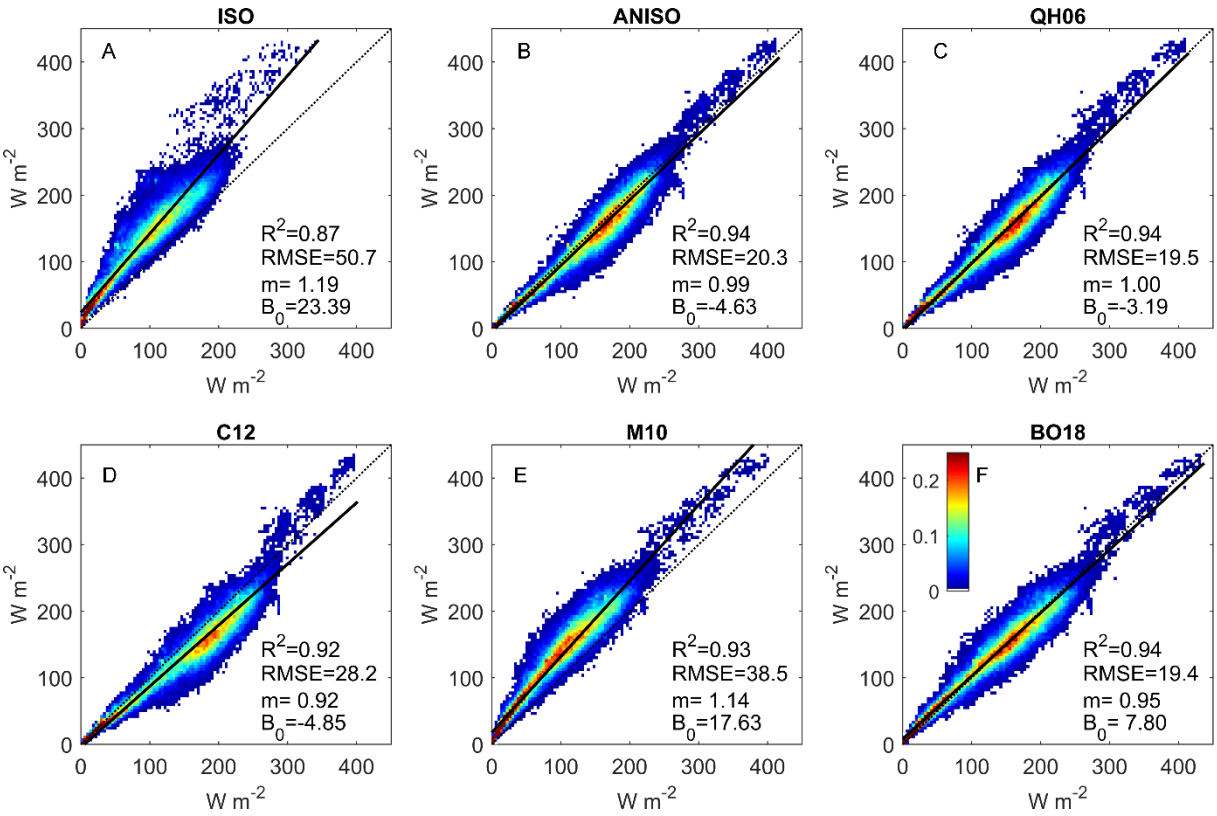

857

858 **Figure 2.** A)-F): Scatter-density regressions of global monthly mean $K_{\alpha}^{\overline{GCM}}$ (y-axis) and

859 K_{α}^{CERES} (x-axis), with the CERES kernel identifier shown at the top of each sub-panel. "*m*" =

860 slope; "B_0" = y-intercept. The color scale indicates the percentage of regression points that

861 fall within an averaging bin, where the x-axis and y-axis have been gridded into 100 × 100

862 equally-spaced bins to help illustrate the density of overlapping points.

863

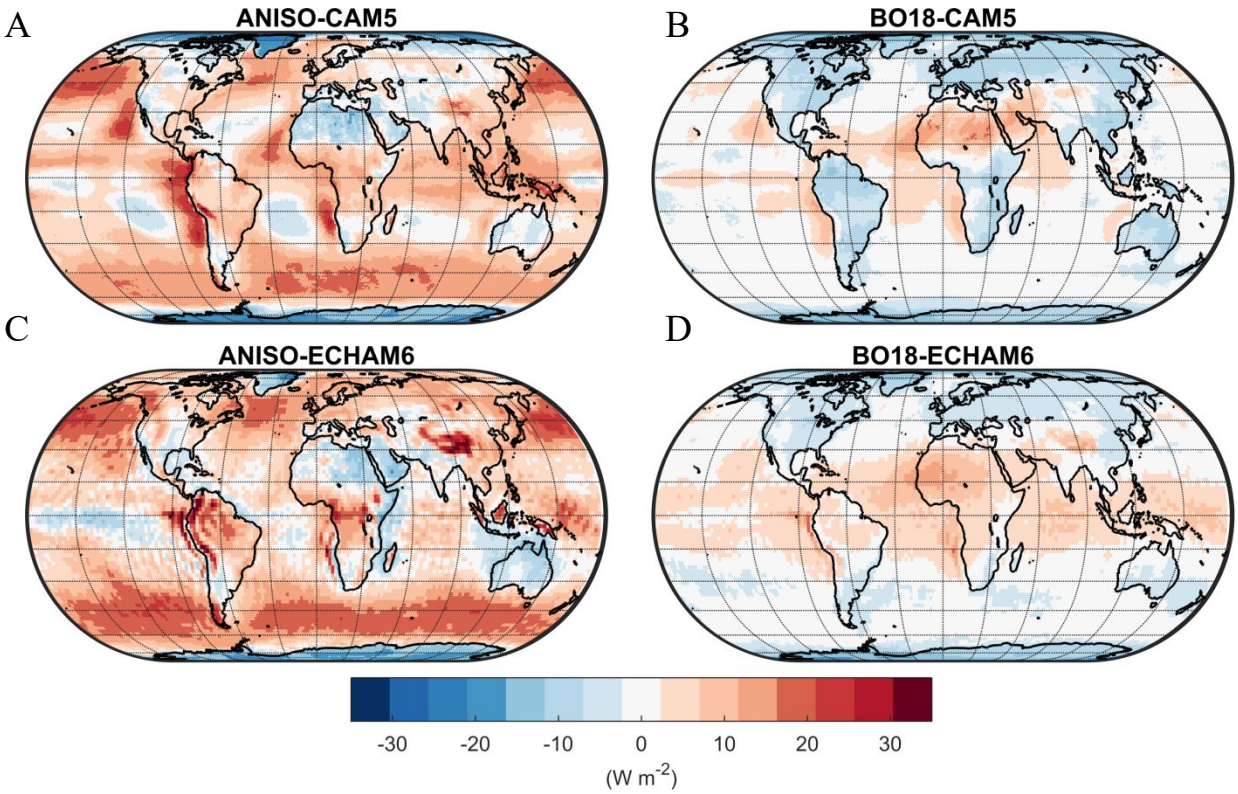

Figure 3. A) Mean annual bias of the CAM5 albedo change kernel emulated with the ANISO semi-empirical model; B) Mean annual bias of the CAM5 albedo change kernel emulated with the BO18 parameterization; C) Mean annual bias of the ECHAM6 albedo change kernel emulated with the ANISO semi-empirical model; D) Mean annual bias of the ECHAM6 albedo change kernel emulated with the BO18 parameterization

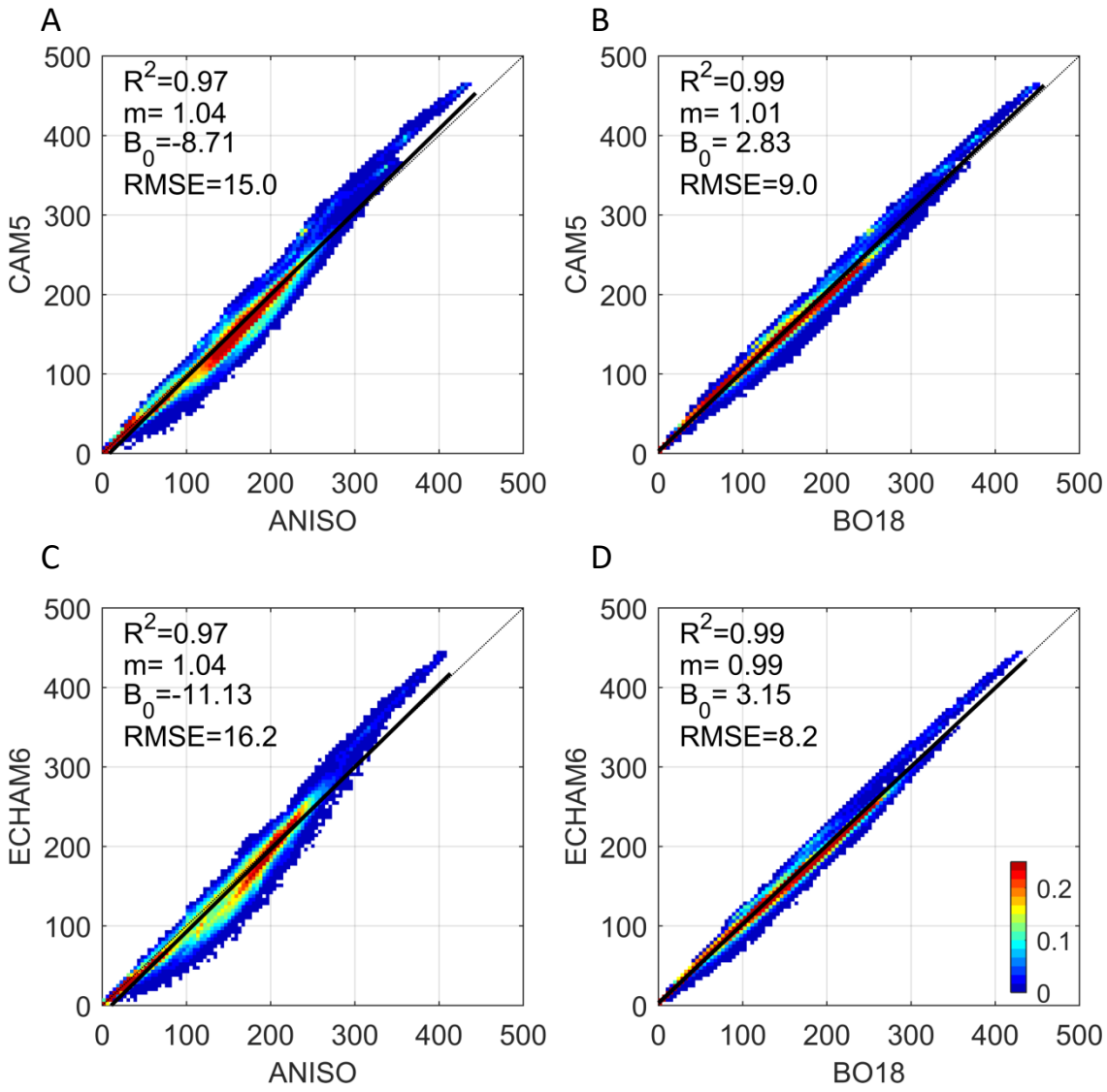

871

872 **Figure 4.** A)-D): Scatter-density regressions of K_{α}^{GCM} (y-axis) and K_{α}^{GCM} emulated with the

873 ANISO semi-empirical model and BO18 parameterization (x-axis); "m" = slope; "B_0" = y-

874 intercept. See Figure 2 caption for a description of the color scale.

875

876

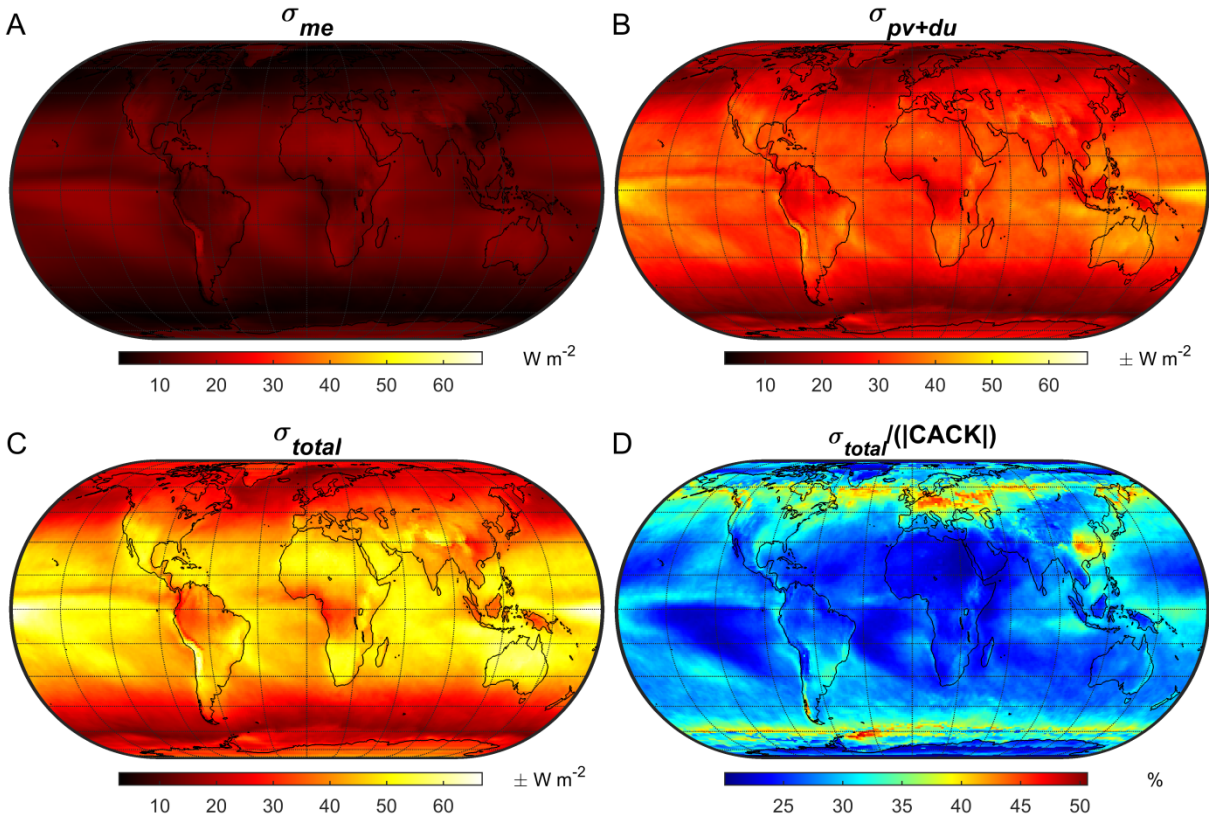

877

878 **Figure 5.** Annual uncertainty of a CACK based on 2001-2016 monthly mean CERES EBAF

879 v4 climatology: A) The absolute uncertainty related to *model error* (i.e., the $K_{\alpha_s}^{BO18}$

880 parameterization); B) The total propagated absolute uncertainty related to *physical variability*

881 and *data uncertainty* of CACK input variables; C) Total absolute uncertainty; D) Total

882 relative uncertainty.

883

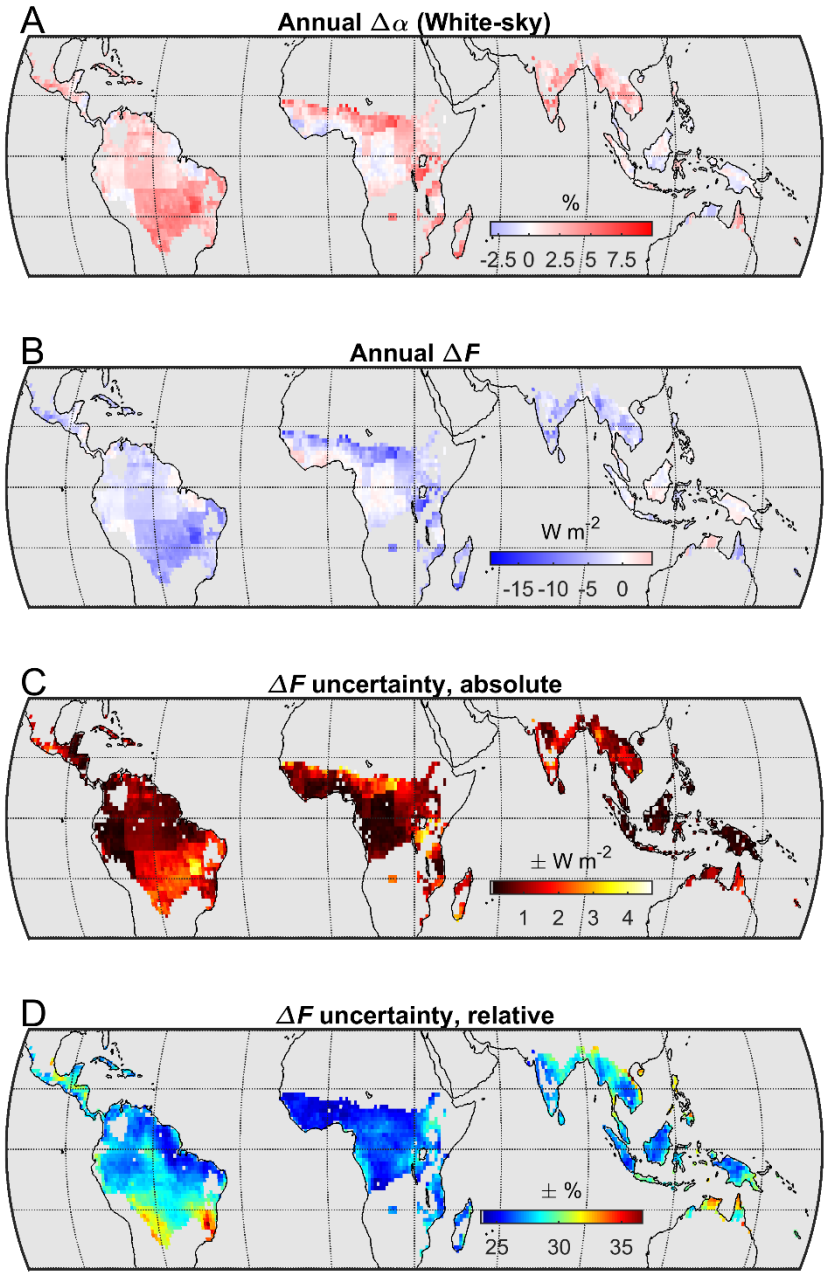

884

885 **Figure 6.** Example application of a CACK based on the 2001-2016 monthly mean CERES
886 EBAF v4 climatology. A) Annual mean of the climatological (i.e., 2001-2011) monthly
887 mean difference in white-sky surface albedo between *grasslands* and *evergreen broadleaved*
888 *forests* ($\Delta\alpha_s$) based on the 1° product of Gao *et al*. (2014); B) Annual mean instantaneous
889 radiative forcing (ΔF) of monthly mean $\Delta\alpha_s$ estimated with CACK; C) Absolute uncertainty
890 (annual mean) of the CACK-based ΔF estimate, including the uncertainty of $\Delta\alpha_s$; D)
891 Relative uncertainty (annual mean) of the CACK-based ΔF estimate.

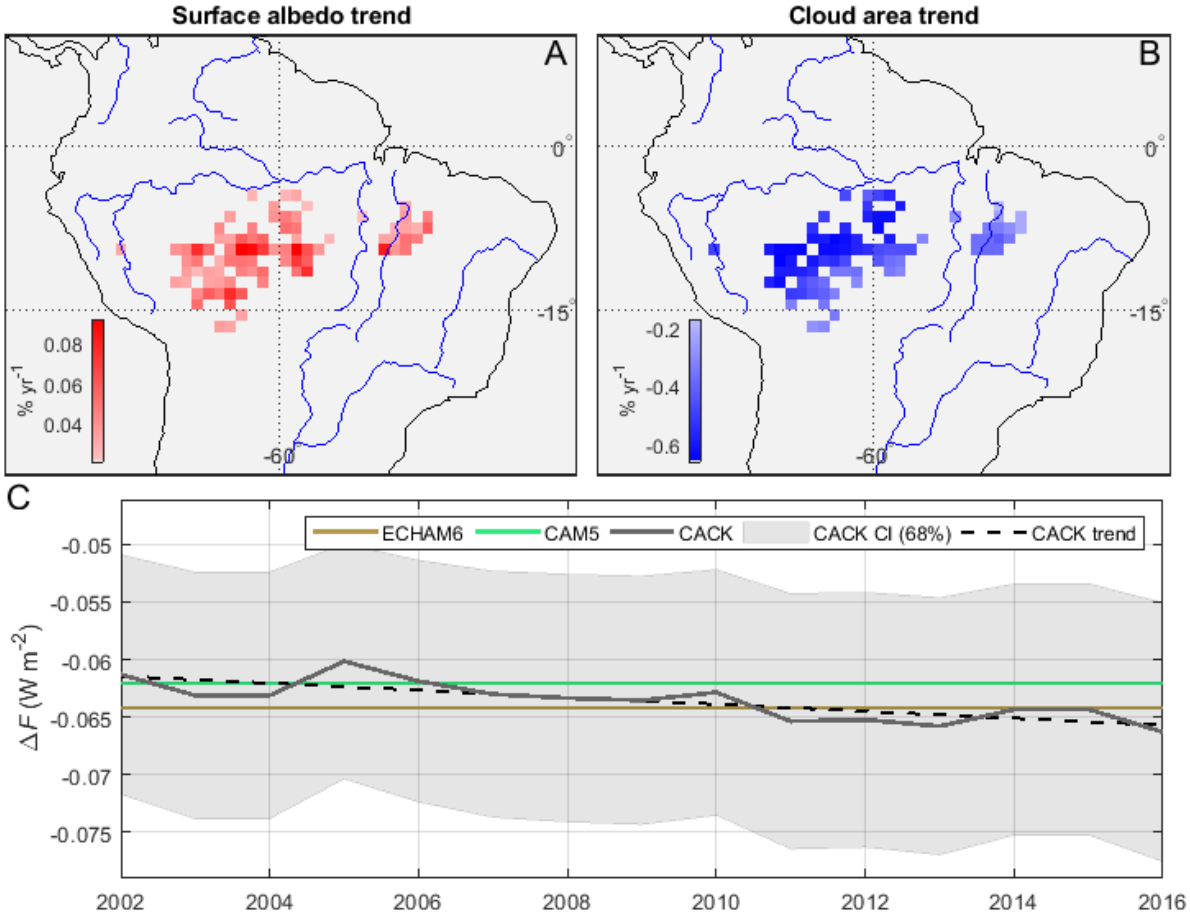

892

893 **Figure 7.** Example application of a temporally-explicit CACK. A) 2001-2016 statistically

894 significant positive trends in all-sky *surface albedo* derived from CERES EBAF-Surface v4;

895 B) 2001-2016 statistically significant negative trends in *cloud area* derived from CERES

896 EBAF-TOA v4; C) Mean local ΔF from $\Delta\alpha_s$ when estimated with the CACK, ECHAM6,

897 and CAM5 surface albedo change kernels. The 1σ confidence interval ("CI") shown for

898 CACK excludes the uncertainty component related to *physical variability*.

899

Supporting Information for:

Developing a monthly radiative kernel for surface albedo change from satellite climatologies of Earth's shortwave radiation budget: CACK v1.0

Ryan M. Bright and Thomas L. O'Halloran

Machine learning results summary

A subset of the machine learning model solutions for ECHAM6 and CAM5 and associated summary statistics are presented in Table S1. Equivalent solutions of complexities 1, 6, 7, and 10 were found independently by the two GCMs. The model with complexity 10 (red boldface) was the highest performing model common to both GCMs and was chosen to represent $K_{\alpha_s}^{BO18}$ and hence subjected to further performance evaluation in the main article.

Table S1. Subset of machine learning model solutions for ECHAM6 and CAM5 and associated statistics for the "selected" solutions shown in Figure S1. Means of CAM5 and ECHAM6 kernels are 140.2 and 133.4 W m^{-2}, respectively, which are used to compute the monthly relative RMSEs ("rRMSE"; in %). "Comp." = model complexity.

Solution	R^2	Max Error	rRMSE (%)	MSE	MAE	Comp.
ECHAM6						
$K = \left[SW_{\uparrow}^{SFC} + SW_{\uparrow}^{TOA} + SW_{\downarrow}^{SFC}\sqrt{SW_{\downarrow}^{SFC}} - SW_{\downarrow}^{TOA} \right] \Big/ \sqrt{SW_{\downarrow}^{TOA}} + \log\left(SW_{\downarrow}^{TOA} + SW_{\downarrow}^{TOA} SW_{\downarrow}^{SFC} \right)$	1.00	31.96	4.1	27.02	3.92	30
$K = \left[SW_{\uparrow}^{SFC} + SW_{\downarrow}^{SFC}\sqrt{SW_{\downarrow}^{SFC}} \right] \Big/ \sqrt{SW_{\downarrow}^{TOA}}$	0.99	32.59	5.6	40.93	4.91	16
$K = SW_{\downarrow}^{SFC}\sqrt{SW_{\downarrow}^{SFC} \Big/ SW_{\downarrow}^{TOA}}$	**0.99**	**31.59**	**7.1**	**66.48**	**6.03**	**10**
$K = SW_{\downarrow}^{SFC} - \sqrt{SW_{\downarrow}^{TOA}}$	0.86	81.55	22.0	947.8	25.10	7
$K = SW_{\downarrow}^{SFC\ 2} \Big/ SW_{\downarrow}^{TOA}$	0.81	82.95	31.4	1,314	33.03	6
$K = SW_{\downarrow}^{SFC}$	0.67	103.8	41.0	2,245	40.98	1
CAM5						
$K = \sqrt{SW_{\uparrow}^{SFC}\sqrt{SW_{\uparrow}^{SFC}} + SW_{\downarrow}^{SFC\ 3} \Big/ SW_{\downarrow}^{TOA} + SW_{\uparrow}^{SFC}\sqrt{SW_{\downarrow}^{TOA} + SW_{\uparrow}^{SFC}}}$	1.00	43.57	5.0	35.66	4.31	30
$K = SW_{\downarrow}^{SFC} + \left(SW_{\uparrow}^{SFC} - SW_{\downarrow}^{TOA} \right) \Big/ \log\left(SW_{\downarrow}^{TOA} \right) + \log\left(SW_{\downarrow}^{TOA} \right)$	0.99	53.39	5.7	45.82	5.31	18
$K = SW_{\downarrow}^{SFC}\sqrt{SW_{\downarrow}^{SFC} \Big/ SW_{\downarrow}^{TOA}}$	**0.99**	**36.62**	**7.7**	**83.37**	**6.71**	**10**
$K = SW_{\downarrow}^{SFC} - \sqrt{SW_{\downarrow}^{TOA}}$	0.88	82.26	25.0	874.9	23.87	7

$K = SW_{\downarrow}^{SFC\ 2} / SW_{\downarrow}^{TOA}$	0.80	83.99	32.4	1,474	35.04	6
$K = SW_{\downarrow}^{SFC}$	0.71	103.9	38.7	2,098	39.03	1
ECHAM6 & CAM5 mean						
$K = K_{\alpha_s}^{BO18} = SW_{\downarrow}^{SFC} \sqrt{SW_{\downarrow}^{SFC} / SW_{\downarrow}^{TOA}}$	***0.99***	***34.11***	***7.4***	***74.93***	***6.37***	***10***

The rRMSE for $K_{\alpha_s}^{BO18}$ of Table S1 is the mean rRMSE for the ECHAM6 and CAM5 solutions.

Figure S1 illustrates the Pareto front used to assist $K_{\alpha_s}^{BO18}$ model selection. Model solutions are plotted as small dots showing model MSE as a function of model complexity. A subset of models of interest, generally found at 'elbows' in the Pareto front, are indicated by larger dots. At these elbows, slight increases in model complexity lead to large reductions in model error. $K_{\alpha_s}^{BO18}$ has a model complexity of 10.

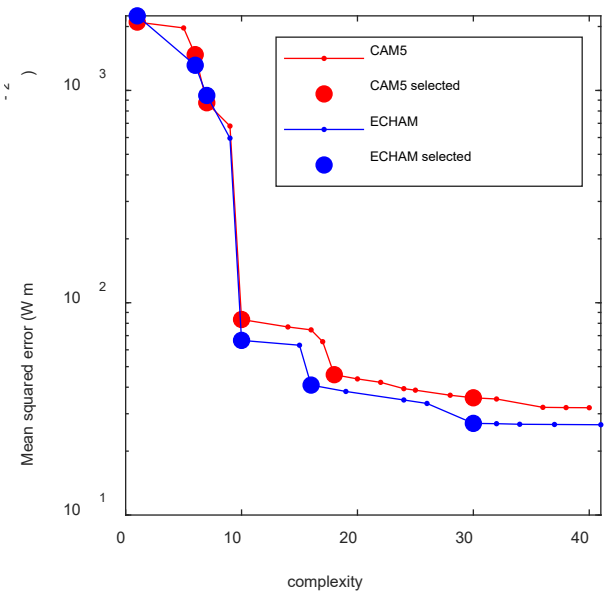

Figure S1. Pareto front used to assist model selection from machine learning output.

Additional uncertainty detail

The rRMSE for $K_{\alpha_s}^{BO18}$ (Table S1) is used to estimate CACK's monthly model error for a given grid cell as follows:

$$\sigma_{me,m,p}(CACK) = \frac{RMSE}{\left|\overline{K_{\alpha_s}^{GCM}}\right|} CACK_{m,p} \quad \text{(S1)}$$

where the numerator represents the mean RMSE of the ECHAM6 and CAM5 solutions, $\overline{K_{\alpha_s}^{GCM}}$ is the mean of the monthly ECHAM6 and CAM5 kernels in the training datasets, and $CACK_{m,p}$ is the CERES albedo change kernel (CACK) based on the $K_{\alpha_s}^{BO18}$ parameterization for month *m* and grid cell *p*.

Uncertainty related to the local "physical variability" of a CERES input variable x for any given month *m* and grid cell *p* is taken as the standard deviation within the 2001-2016 period:

$$\sigma_{PV,m,p}(x) = \sqrt{\frac{\sum \left| x_{m,p} - \overline{x}_{m,p} \right|}{Y}} \quad \text{(S2)}$$

where $x_{m,p}$ is the monthly and grid cell value of x, Y is the total number of years in the period (i.e., 16), and $\overline{x}_{m,p}$ is the monthly and grid cell mean of x during this period.

Uncertainty related to CERES EBAF input variable x for any given month *m* and grid cell *p* is estimated using its relative uncertainty as:

$$\sigma_{DU,m,p}(x) = \frac{\sigma(x)}{\left|\overline{x}\right|} x_{m,p} \quad \text{(S3)}$$

where x_m is the monthly and grid cell value of x, $\sigma(x)$ is the absolute uncertainty of x (Table S2), and $\overline{x}$ is the mean x of the sample domain (Table S2).

Table S2. Uncertainty of the CERES EBAF v4 input variables required by CACK.

CERES Variable	Domain	x (W m^{-2})	$\sigma(x)$ (W m^{-2})	$\sigma(x)/\left\|\overline{x}\right\|$	Reference
$SW_{\downarrow}^{SFC}$	"Ocean + land"	187	13	0.07	(Kato et al., 2018)
$SW_{\downarrow}^{TOA}$	N/A	N/A	N/A	0.01	(Loeb et al., 2017)

Covariance of CERES input variables x_1 and x_2 (i.e., $SW_{\downarrow}^{SFC}$ and $SW_{\downarrow}^{TOA}$) in any given grid cell *p* is estimated as:

$$\sigma_p(x_1, x_2) = \frac{1}{M-1} \sum_{m=1}^{M} (x_{1,m,p} - \overline{x}_{1,p})(x_{2,m,p} - \overline{x}_{2,p}) \quad \text{(S4)}$$

where M is the total number of months, $x_{1,m,p}$ and $x_{2,m,p}$ are the values for variables x_1 and x_2 in grid cell *p* and month *m*, and $\overline{x}_{1,p}$ and $\overline{x}_{2,p}$ are the means of x_1 and x_2 in grid cell *p* for the 2001-2016 time period.

Grid cell σ and grid cell and monthly σ_{PV} and σ_{DU} are then used to estimate the total propagated uncertainty of CERES input variables x_1 and x_2 (i.e., $SW_{\downarrow}^{SFC}$ and $SW_{\downarrow}^{TOA}$) as the second right-hand term of Eq. (21) of the main article. This is then summed together with the σ_{me} estimated as equation S1. In Eq. (21), the partial derivative of CACK with respect to $SW_{\downarrow}^{SFC}$ is given as:

$$\frac{\partial CACK}{\partial SW_{\downarrow}^{SFC}} = \frac{3\sqrt{SW_{\downarrow}^{SFC} / SW_{\downarrow}^{TOA}}}{2} \tag{S5}$$

The partial derivative of CACK with respect to $SW_{\downarrow}^{TOA}$ is given as:

$$\frac{\partial CACK}{\partial SW_{\downarrow}^{TOA}} = -0.5\left(\frac{SW_{\downarrow}^{SFC}}{SW_{\downarrow}^{TOA}}\right)^{\frac{3}{2}} \tag{S6}$$

CACK v1.0 dataset summary

Table S3 summarizes the variables comprising the CACK v1.0 dataset.

Table S3. Summary of variables included in the CACK v1.0 dataset.

Variable name	Description	Temporal resolution	Temporal signature (extent)
"CACK CM"	Eq. (17) with CERES inputs as 2001-2016 means	Monthly	2001-2016 mean
"Sigma_me CM"	First right-hand term of Eq. (21) estimated as Eq. (S1) with CERES inputs as 2001-2016 means	Monthly	2001-2016 mean
"Sigma_du_pv CM"	Second right-hand term in Eq. (21) where $\sigma(x_1, x_2)$, $\sigma_{PV}(x_n)$, and $\sigma_{DU}(x_n)$ are estimated with Eq.'s S2-S4, and x_1 an d x_2 are 2001-2016 means of $SW_{\downarrow}^{SFC}$ and $SW_{\downarrow}^{TOA}$	Monthly	2001-2016 mean
"Sigma_total CM"	Eq. (21), or the sum of "Sigma_me CM" and "Sigman_du_pv CM"	Monthly	2001-2016 mean
"CACK"	Eq. (17) estimated for all years in the 2001-2016 period	Monthly	Annual (2001-2016)
"Sigma_me"	First right-hand term of Eq. (21) estimated as Eq. (S1) for all years in the 2001-2016 period	Monthly	Annual (2001-2016)

"Sigma_du"	Second right-hand term of Eq. (21) estimated for all years in the 2001-2016 period but excluding $\sigma_{PV}(x_n)$; $\sigma(x_1, x_2)$ and $\sigma_{DU}(x_n)$ are estimated with Eq.'s S3-S4; x_1 an d x_2 are $SW_{\downarrow}^{SFC}$ and $SW_{\downarrow}^{TOA}$ provided by CERES EBAF v4.	Monthly	Annual (2001-2016)
"Sigma_total"	Sum of "Sigma_me" and "Sigma_du"	Monthly	Annual (2001-2016)

References

Kato, S., Rose, F. G., Rutan, D. A., Thorsen, T. J., Loeb, N. G., Doelling, D. R., Huang, X., Smith, W. L., Su, W., and Ham, S.-H.: Surface Irradiances of Edition 4.0 Clouds and the Earth's Radiant Energy System (CERES) Energy Balanced and Filled (EBAF) Data Product, Journal of Climate, 31, 4501-4527, 10.1175/JCLI-D-17-0523.1, 2018.

Loeb, N. G., Doelling, D. R., Wang, H., Su, W., Nguyen, C., Corbett, J. G., Liang, L., Mitrescu, C., Rose, F. G., and Kato, S.: Clouds and the Earth's Radiant Energy System (CERES) Energy Balanced and Filled (EBAF) Top-of-Atmosphere (TOA) Edition-4.0 Data Product, Journal of Climate, 31, 895-918, 10.1175/JCLI-D-17-0208.1, 2017.

Developing a monthly ~~albedo change~~ radiative ~~forcing~~ kernel for surface albedo change from satellite climatologies of Earth's shortwave radiation budget: CACK v1.0

Ryan M. Bright[1*] and Thomas L. O'Halloran[2,3]

1 – Norwegian Institute of Bioeconomy Research, Ås, Norway

2 – Department of Forestry and Environmental Conservation, Clemson University, Clemson, South Carolina, USA.

3 – Baruch Institute of Coastal Ecology and Forest Science, Clemson University, Georgetown, South Carolina, USA

[*]Contact: ryan.bright@nibio.no

Abstract

Due to the potential for land use / land cover change (LULCC) to alter surface albedo, there is need within the LULCC science community for simple and transparent tools for predicting radiative forcings (ΔF) from surface albedo changes ($\Delta\alpha_s$). To that end, the radiative kernel technique – developed by the climate modeling community to diagnose internal feedbacks within general circulation models (GCMs) – has been adopted by the LULCC science community as a tool to perform offline ΔF calculations for $\Delta\alpha_s$. However, the codes and data behind the GCM kernels are not readily transparent, and the climatologies of the atmospheric state variables used to derive them ~~GCM~~ vary widely both in time period and duration. ~~codes are not readily transparent and the atmospheric state variables used as model input are limited to single years, thus being sensitive to anomalous weather conditions that may have occurred in those simulated years.~~ Observation-based kernels ~~founded on longer-term climatologies of Earth's atmospheric state~~ offer an attractive alternative to GCM-based

kernels and could be updated annually at relatively low costs. Here, we present a radiative kernel for surface albedo change ~~we evaluate~~founded on ~~simplified models~~a novel, simplified parameterization ~~-~~of shortwave radiative transfer ~~as candidates for an albedo change kernel founded on~~driven with inputs from ~~the~~ the Clouds and the Earth's Radiant Energy System (CERES) Energy Balance and Filled (EBAF) products. When based on a 16-year climatology (2001-2016), we find that the CERES albedo change kernel – or CACK – ~~We find that a new, simple model supported by statistical analyses gives remarkable agreement when benchmarked t~~agrees remarkably well with ~~o~~ the mean kernel of four GCM~~-~~s (rRMSE = 14%)~~kernels~~. When the novel parameterization underlying CACK is applied to emulate two of the GCM kernels using their own boundary fluxes as input, we find even greater agreement (mean rRMSE = 7.4%), suggesting that this simple and transparent parameterization represents a credible candidate for a satellite-based alternative to GCM kernels ~~and to two GCM kernels following emulation with their own boundary fluxes as input. Our findings lend support to its candidacy as a satellite-based alternative to GCM kernels and to its application in land-climate studies~~. We document and compute the various sources of uncertainty underlying CACK and include them as part of a more extensive dataset (CACK v1.0) while providing examples showcasing its application.

Keywords: GCM, radiative forcing, land use change, land cover change, LULCC

1. Introduction

Diagnosing changes to the shortwave radiation balance at the top-of-the-atmosphere (TOA) resulting from changes to albedo at the surface ($\Delta\alpha_s$) is an important step in predicting climate change. However, outside the climate science community, many researchers do not have the tools to convert $\Delta\alpha$ to the climate-relevant ΔF measure (Bright, 2015;Jones et al., 2015), which requires a detailed representation of the atmospheric constituents that absorb or

scatter solar radiation (e.g. cloud, aerosols, and gases) and a sophisticated radiative transfer code. For single points in space or for small regions, these calculations are typically performed offline – meaning without feedbacks to the atmosphere (e.g., ~~(Randerson et al. 2006~~(Randerson et al., 2006))). Large-scale investigations (e.g. Amazonian or pan-boreal LULCC (Dickinson and Henderson-Sellers, 1988;Bonan et al., 1992)) typically prescribe the land surface layer in a GCM with initial and perturbed states, allowing the radiative transfer code to interact with the rest of the model. While this has the benefit of allowing interaction and feedbacks between surface albedo and scattering or absorbing components of the model, such an approach is computationally expensive and thereby restricts the number of LULCC scenarios that can be investigated (Atwood et al., 2016). Consequently, this method does not meet the needs of some modern LULCC studies which may require millions of individual land cover transitions to be evaluated cost effectively (Lutz and Howarth, 2015;Ghimire et al., 2014).

Within the LULCC science community, two methods have primarily met the need for efficient ΔF calculations from $\Delta\alpha_s$: simplified parameterizations of atmospheric transfer of shortwave radiation (Bright and Kvalevåg, 2013;Cherubini et al., 2012;Bozzi et al., 2015;Muñoz et al., 2010;Caiazzo et al., 2014;Carrer et al., 2018), and radiative kernels (Ghimire et al., 2014;O'Halloran et al., 2012;Vanderhoof et al., 2013) derived from sophisticated radiative transfer schemes embedded in GCMs (Soden et al., 2008;Shell et al., 2008;Pendergrass et al., 2018;Block and Mauritsen, 2014). Simplified parameterizations of the LULCC science community have not been evaluated comprehensively in space and time. Bright & Kvalevåg (2013) evaluated the shortwave ΔF parameterization of Cherubini *et al.* (2012) when applied at several ~~sites distributed~~ globally distributed sites on land, finding

inconsistencies in performance at individual sites despite good overall cross-site performance. Radiative kernels (Soden et al., 2008;Shell et al., 2008;Pendergrass et al., 2018;Block and Mauritsen, 2014) – while being based on state-of-the-art models of radiative transfer – have the downside of being model-dependent and not readily transparent. While the radiative transfer codes behind them are well-documented, the scattering components (i.e. aerosols, gases, and clouds) affecting transmission have many simplifying parameterizations, vary widely across models, and may contain significant biases (Dolinar et al., 2015;Wang and Su, 2013). An additional downside is ~~the~~ that the atmospheric state climatologies used to compute the GCM kernels vary widely in their time periods (i.e., from pre-industrial to the year 2007) and ~~extents~~durations (from 1 to 1,000 yrs). ~~variables used as model input are limited to single years, thus being sensitive to anomalous weather conditions that may have occurred in those years. Further, t~~The application of a state-dependent GCM kernel that is outdated may be undesirable in regions undergoing rapid changes in cloud cover or aerosol optical depth, such as in the northwest United States (Free and Sun, 2014) and in southern and eastern Asia (Zhao et al., 2018;Srivastava, 2017), respectively. An albedo change ~~-~~kernel based on Earth-orbiting satellite products ~~remotely-sensed observations~~ could be updated annually to capture changes in atmospheric state at relatively low costs.

The NASA Clouds and the Earth's Radiant Energy System (CERES) Energy Balance and Filled (EBAF) products (CERES Science Team, 2018a, b), which are based largely on satellite optical remote sensing, provide the monthly mean boundary fluxes and other atmospheric state information (e.g., cloud area fraction, cloud optical depth) that could be used to develop a more empirically-based alternative to the GCM-based kernels. The latest EBAF-TOA Ed4.0 (version 4.0) products have many improvements with respect to the previous version (version 2.8, Loeb et al. 2009), including the use of advanced and more

consistent input data, retrieval of cloud properties, and instrument calibration (Kato et al., 2018;Loeb et al., 2017).

Here, we present an albedo change kernel based on the CERES EBAF v4 products – or CACK. Underlying CACK is a simplified model of shortwave radiative transfer through a one-layer atmosphere. The model form (or parameterization) is selected after a two-stage performance evaluation of six model candidates: two analytical, one semi-empirical, and three empirical. An initial performance screening is implemented where all six model candidates are driven with a 16-year climatology (January 2001 – December 2016) of monthly all-sky boundary fluxes from CERES, with the resulting kernels benchmarked both qualitatively and quantitatively against the mean of four GCM-based kernels (Shell et al., 2008;Soden et al., 2008;Pendergrass et al., 2018;Block and Mauritsen, 2014). Top model candidates from the initial performance screening are then subjected to an additional performance evaluation where they are applied to emulate two GCM kernels using their own boundary fluxes as input, which eliminates possible biases related to differences in the GCM representation of clouds or other atmosphere state variables.

We start in Section 2 by providing a brief overview of existing approaches applied in LULCC climate studies for estimating ΔF from $\Delta\alpha$. We then present the six model candidates in Section 3. Section 4 describes the model evaluation and uncertainty quantification methods, in addition to two application examples. Results are presented in Section 5, while Section 6 discusses the merits and uncertainties of a CERES-based kernel relative to GCM-based kernels.

~~Within the atmospheric science community, simplified radiative transfer frameworks have been developed, either to diagnose effective surface and atmospheric optical properties from~~

climate model outputs, or to study the relative contributions of changes to these properties on shortwave flux changes at the top and bottom of the atmosphere (Rasool and Schneider, 1971;Winton, 2005;Winton, 2006;Taylor et al., 2007;Donohoe and Battisti, 2011;Atwood et al., 2016;Kashimura et al., 2017;Qu and Hall, 2006). These frameworks differ by whether or not the reflection and transmission properties of the atmospheric layer are assumed to have a directional dependency (Stephens et al., 2015) and by the number of variables required as input (Qu and Hall, 2006). Winton (2005) presented a four-parameter optical model to account for the directional dependency of up- and downwelling shortwave fluxes through a one-layer atmosphere and found good agreement (RMSE < 2% globally) when benchmarked to online radiative transfer calculations. Also considering a directional dependency of the atmospheric optical properties, Taylor et al. (2007) presented a two-parameter model where atmospheric absorption was assumed to occur at a level above atmospheric reflection. Donohoe and Battisti (2011) subsequently relaxed the directional dependency assumption and found the atmospheric attenuation of the surface albedo contribution to planetary albedo to be 8% higher than the model of Taylor et al. (2007). Elsewhere, Qu & Hall (2006) developed a framework making use of additional known atmospheric properties such as cloud cover fraction, cloud optical thickness, and the clear-sky planetary albedo which proved highly accurate when model estimates of planetary albedo were evaluated against climate models and satellite-based datasets.

Here, our primary research objective is to thoroughly evaluate a variety of shortwave kernels derived both analytically and statistically from satellite-based climatologies of Earth's shortwave radiation budget. To this end, we employ a 16-yr. time series of Earth's monthly mean radiation budget at both TOA (Loeb et al., 2017) and at the surface (Kato et al., 2012) as input to simplified models linking $\Delta\alpha_s$ to changes in the outgoing shortwave radiation flux at TOA. An initial performance screening is implemented where the six observation-driven

~~kernels are first assessed both qualitatively and quantitatively against the mean of four GCM kernels (Shell et al., 2008;Soden et al., 2008;Pendergrass et al., 2018;Block and Mauritsen, 2014). Top performers are then subjected to a more rigorous evaluation where they are applied to emulate the GCM kernels using the GCM's own boundary fluxes as input, which eliminates any bias related to differences in the GCM representation of clouds or other atmosphere state variables. Our results elucidate the merits and uncertainties of empirical alternatives to those based on GCMs.~~

~~We start in Section 2 by introducing the satellite-based energy balance product and the variables derived from them utilized in this study. We then provide a brief overview of the GCM-based kernels and of the methods currently being applied within the LULCC science community to estimate instantaneous radiative forcings from surface albedo change. Section 3 details the methods applied to derive candidate GCM kernel alternatives from the radiative fluxes at Earth's upper and lower boundaries. We then present results of a comparative analysis in Section 4 and conclude with a brief discussion surrounding the merits and uncertainties of albedo change kernels based on satellite remote sensing.~~

2 Review of existing approaches

~~*a. Shortwave* ΔF from $\Delta\alpha_s$~~

Earth's energy balance (at TOA) in an equilibrium state can be written:

$$0 = F = LW_{\uparrow}^{TOA} - (SW_{\downarrow}^{TOA} - SW_{\uparrow}^{TOA}) \quad (1)$$

where the equilibrium flux F is a balance between the net solar energy inputs ($SW_{\downarrow}^{TOA} - SW_{\uparrow}^{TOA}$) and thermal energy output ($LW_{\uparrow}^{TOA}$). Perturbing this balance results in a radiative forcing ΔF, while perturbing the shortwave component is referred to as a shortwave radiative forcing and may be written as:

$$\Delta F = \Delta(SW_{\downarrow}^{TOA} - SW_{\uparrow}^{TOA}) = \Delta SW_{\downarrow}^{TOA}\left(1 - \frac{SW_{\uparrow}^{TOA}}{SW_{\downarrow}^{TOA}}\right) - SW_{\downarrow}^{TOA}\left(\Delta\frac{SW_{\uparrow}^{TOA}}{SW_{\downarrow}^{TOA}}\right) \quad (2)$$

where the shortwave radiative forcing results either from changes to solar energy inputs ($\Delta SW_{\downarrow}^{TOA}$) or from internal perturbations~~-~~ within the Earth system ($\Delta\frac{SW_{\uparrow}^{TOA}}{SW_{\downarrow}^{TOA}}$). The latter can be brought about by changes to the reflective properties of Earth's surface~~ and/or atmosphere~~ which is the focus ~~in~~of this paper.

a. GCM-based radiative kernels

The radiative kernel technique was developed as a way to assess various climate feedbacks from climate change simulations across multiple climate models in a computationally efficient manner (Shell et al., 2008;Soden et al., 2008). A radiative kernel is defined as the differential response of an outgoing radiation flux at TOA to an incremental change in some climate state variable -- such as water vapor, air temperature, or surface albedo (Soden et al., 2008). To generate a radiative kernel for a change in surface albedo with a GCM, the prescribed surface albedo change is perturbed incrementally by 1%, and the response by the outgoing shortwave radiation flux at TOA is recorded:

$$\Delta SW_{\uparrow}^{TOA} = SW_{\uparrow}^{TOA}(\alpha_s + \Delta\alpha_s) - SW_{\uparrow}^{TOA}(\alpha_s) = \frac{\partial SW_{\uparrow}^{TOA}}{\partial \alpha_s}\Delta\alpha_s \equiv K_{\alpha_s}\Delta\alpha_s \quad (3)$$

Field Code Changed

where $SW_{\uparrow}^{TOA}$ is the outgoing shortwave flux at TOA and K_{α_s} is the radiative kernel (in Wm^{-2}) which ~~The NASA Clouds and the Earth's Radiant Energy System (CERES) Energy Balance and Filled (EBAF) products provide the monthly mean boundary fluxes and atmospheric state information necessary to derive our GCM kernel alternatives (CERES Science Team, 2018a, b). The latest EBAF-TOA Ed4.0 (version 4.0) products have many improvements with respect to the previous version (version 2.8, Loeb et al. 2009), including the use of advanced and more consistent input data, retrieval of cloud properties, and instrument calibration (Loeb et al. 2018). The temporal extent of the EBAF dataset employed in our analysis spans the sixteen full calendar years from January 1, 2001 to December 31, 2016 (retrieved April, 2018). An overview of all CERES inputs used in our analysis is presented in Table 1.~~

~~< Table 1 >~~

~~*a. Shortwave* ΔF ~~from~~ $\Delta\alpha_s$~~

~~Earth's energy balance (at TOA) in an equilibrium state can be written:~~

~~$0 = F = LW_{\uparrow}^{TOA} - (SW_{\downarrow}^{TOA} - SW_{\uparrow}^{TOA})$ (1)~~

~~where the equilibrium flux F is a balance between the net solar energy inputs ($SW_{\downarrow}^{TOA} - SW_{\uparrow}^{TOA}$) and thermal energy output ($LW_{\uparrow}^{TOA}$). Perturbing this balance results in a radiative forcing ΔF, while perturbing the shortwave component is referred to as a shortwave radiative forcing and may be written as:~~

~~$$\Delta F = \Delta(SW_{\downarrow}^{TOA} - SW_{\uparrow}^{TOA}) = \Delta SW_{\downarrow}^{TOA}\left(1 - \frac{SW_{\uparrow}^{TOA}}{SW_{\downarrow}^{TOA}}\right) - SW_{\downarrow}^{TOA}\left(\Delta\frac{SW_{\uparrow}^{TOA}}{SW_{\downarrow}^{TOA}}\right)$$ (2)~~

Field Code Changed

Field Code Changed

~~where the shortwave radiative forcing results either from changes to solar energy inputs ($\Delta SW_{\downarrow}^{TOA}$) or from internal perturbations within the Earth system ($\Delta \frac{SW_{\uparrow}^{TOA}}{SW_{\downarrow}^{TOA}}$). The latter can be brought about by changes to the reflective properties of Earth's surface and/or atmosphere which is the focus in this paper.~~

~~*b. GCM-based radiative kernels*~~

~~The radiative kernel technique was developed as a way to assess various climate feedbacks from climate change simulations across multiple climate models in a computationally efficient manner (Shell et al., 2008;Soden et al., 2008). A radiative kernel is defined as the differential response of an outgoing radiation flux at TOA to an incremental change in some climate feedback variable -- such as water vapor, air temperature, or surface albedo (Soden et al., 2008). To generate a radiative kernel for a change in surface albedo $\Delta\alpha$ with a GCM, the prescribed surface albedo is perturbed incrementally by 1% and the response by $SW_{\uparrow}^{TOA}$ is recorded, which can be expressed as:~~

~~$$\Delta SW_{\uparrow}^{TOA} = SW_{\uparrow}^{TOA}(\alpha_s + \Delta\alpha_s) - SW_{\uparrow}^{TOA}(\alpha_s) = \frac{\partial SW_{\uparrow}^{TOA}}{\partial \alpha_s}\Delta\alpha_s = K_{\alpha}\Delta\alpha_s \quad (3)$$~~

~~where K_{α} is the radiative kernel (in Wm^{-2}). The albedo change kernel~~ can ~~then~~ then be used with Eq. (1) to estimate an instantaneous shortwave radiative forcing (ΔF) at TOA:

$$\begin{aligned} F + \Delta F &= LW_{\uparrow}^{TOA} - (SW_{\downarrow}^{TOA} - SW_{\uparrow}^{TOA} + K_{\alpha_s}\Delta\alpha_s) \\ \Delta F &= -K_{\alpha_s}\Delta\alpha_s \end{aligned} \quad (4)$$

To the best of our knowledge, four albedo change kernels have been developed based on the following GCMs: the Community Atmosphere Model version 3, or CAM3 (Shell et al., 2008), the Community Atmosphere Model version 5, or CAM5 (Pendergrass et al., 2018), the European Center and Hamburg model version 6, or ECHAM6 (Block and Mauritsen, 2014), and the Geophysical Fluid Dynamics Laboratory model version AM2p12b, or GFDL (Soden

et al., 2008). These four GCM kernels vary in their vertical and horizontal resolutions, their parameterizations of shortwave radiative transfer, and their prescribed atmospheric state climatologies. ~~(Soden et al., 2008;Shell et al., 2008;Block and Mauritsen, 2014;Pendergrass et al., 2018)~~These differences are summarized in Table 1. Apart from differences in their prescribed atmospheric background states and radiative transfer schemes, a major source of uncertainty in GCM-based kernels is related to the GCM representation of atmospheric liquid water/ice associated with convective clouds; of the four aforementioned GCMs, only CAM5 and GFDL attempt to model the effects of convective core ice and liquid in their radiation calculations (Li et al., 2013).

< Table 1 >

b. Single-layer atmosphere models of shortwave radiation transfer

Within the atmospheric science community, various simplified analytical or semi-empirical modeling frameworks have been developed, either to diagnose effective surface and atmospheric optical properties from climate model outputs, or to study the relative contributions of changes to these properties on shortwave flux changes at the top and bottom of the atmosphere (Rasool and Schneider, 1971;Winton, 2005;Winton, 2006;Taylor et al., 2007;Donohoe and Battisti, 2011;Atwood et al., 2016;Kashimura et al., 2017;Qu and Hall, 2006). While these frameworks all treat the atmosphere as a single layer, they differ by whether or not the reflection and transmission properties of this layer are assumed to have a directional dependency (Stephens et al., 2015) and by whether or not inputs other than those derived from the boundary fluxes are required (e.g. cloud properties; (Qu and Hall, 2006)).

Winton (2005) presented a semi-empirical four-parameter optical model to account for the directional dependency of up- and downwelling shortwave fluxes through the one-layer

atmosphere and found good agreement (rRMSE < 2% globally) when benchmarked to online radiative transfer calculations. Also considering a directional dependency of the atmospheric optical properties, Taylor et al. (2007) presented a two-parameter analytical model where atmospheric absorption was assumed to occur at a level above atmospheric reflection. The analytical model of Donohoe and Battisti (2011) subsequently relaxed the directional dependency assumption and found the atmospheric attenuation of the surface albedo contribution to planetary albedo to be 8% higher than the model of Taylor et al. (2007). Elsewhere, Qu & Hall (2006) developed an analytical framework making use of additional atmospheric properties such as cloud cover fraction, cloud optical thickness, and the clear-sky planetary albedo, which proved highly accurate when model estimates of planetary albedo were evaluated against climate models and satellite-based datasets.

~~c~~. *Simple ~~kernel~~ empirical parameterizations of the LULCC science community*

Two ~~simplified~~ simple empirical parameterizations of shortwave radiative transfer have been widely applied within the LULCC science community for estimating ΔF from $\Delta\alpha_s$ (Muñoz et al., 2010;Lutz et al., 2015;Bozzi et al., 2015;Caiazzo et al., 2014;Cherubini et al., 2012;Carrer et al., 2018). While these parameterizations are also based on a single-layer atmosphere model of shortwave radiative transfer, ~~A~~at the core of these parameterizations is the fundamental assumption that radiative transfer is wholly independent of (or unaffected by) $\Delta\alpha_s$. In other words, they neglect the change in the attenuating effect of multiple reflections between the surface and the atmosphere that accompanies a change to the surface albedo ~~change~~. Nevertheless, due to their simplicity and ease of application they continue to be widely employed in climate research. ~~Although not referred to as "kernels" in the literature, we present them as such to ensure consistency in notation and terminology henceforth. These are subsequently included in the kernel evaluation exercise presented in Section 4.~~

~~The first simplified kernel presented in Muñoz et al. (2010) makes use of a local two-way transmittance factor based on the local clearness index (defined in Table 1):~~

$$\frac{\partial SW_{\uparrow}^{TOA}}{\partial \alpha_s}\Delta\alpha_s \equiv K_{\alpha}^{M10}\Delta\alpha_s = SW_{\downarrow}^{TOA}T^2\Delta\alpha_s \quad (5)$$

~~where~~ $SW_{\downarrow}^{TOA}$ ~~is the local incoming solar flux at TOA,~~ T ~~is the local clearness index, and~~ $\partial SW_{\uparrow}^{TOA}/\partial\alpha$ ~~is the approximated change in the upwelling shortwave flux at TOA due to a change in albedo at the surface.~~

~~The second simplified kernel proposed in Cherubini et al. (2012) makes direct use of the solar flux incident at the surface~~ $SW_{\downarrow}^{SFC}$ ~~combined with a one-way transmission constant~~ k~~:~~

$$\frac{\partial SW_{\uparrow}^{TOA}}{\partial \alpha_s}\Delta\alpha_s \equiv K_{\alpha}^{C12}\Delta\alpha_s = SW_{\downarrow}^{SFC}k\Delta\alpha_s \quad (6)$$

~~where~~ k ~~is based on the global annual mean share of surface reflected shortwave radiation exiting a clear sky (Lacis and Hansen, 1974;Lenton and Vaughan, 2009) and is hence temporally and spatially invariant. This value – or 0.85 – is similar to the global mean ratio of forward to total shortwave scattering reported in Iqbal (1983). Bright & Kvalevåg (2013) evaluated Eq. (6) at several locations and found large biases for some regions and months, despite good overall performance globally (normalized RMSE = 7%; n = 120 months).~~

3. ~~Methods~~Kernel model candidates

The six candidate models (or parameterizations) for a CERES-based albedo change kernel (CACK) are presented henceforth. All requisite variables and their derivatives may be obtained directly from the CERES EBAF v4 products (at monthly and 1° × 1° resolution) and are presented in Table 2. To improve readability, temporal and spatial indexing is neglected and all terms presented henceforth in Section 3 denote the monthly pixel means.

< Table 2 >

~~Simple analytical models developed by the climate science community treat the atmosphere as a single layer having various optical properties. These models vary by the number and type of optical properties included, whether these have a directional dependency (i.e., isotropic or anisotropic), or whether inputs other than those derived from the boundary fluxes are required (i.e., cloud properties). These models are adapted here to derive kernels analytically for $\Delta\alpha_s$.~~

a. ~~CERES isotropic~~ Analytical kernels

The first kernel candidate may be analytically-derived from the CERES EBAF all-sky boundary fluxes and their derivatives. The surface contribution to the outgoing shortwave flux at TOA $SW^{TOA}_{\uparrow,SFC}$ ~~is given~~can be expressed (Stephens et al., 2015;Donohoe and Battisti, 2011;Winton, 2005) as:

$$SW^{TOA}_{\uparrow,SFC} = SW^{TOA}_{\downarrow}\alpha_s \frac{(1-r-a)^2}{(1-r\alpha_s)} \quad (~~7~~5)$$

where r is a single pass atmospheric reflection coefficient, a is a single pass atmospheric absorption coefficient, $SW^{TOA}_{\downarrow}$ is the extraterrestrial (downwelling) shortwave flux at TOA, and α_s is the surface albedo (defined in Table ~~1~~2). The expression in the denominator of the righthand term represents a fraction attenuated by multiple reflections between the surface and the atmosphere. This model assumes that the atmospheric optical properties r and a are

insensitive to the origin and direction of shortwave fluxes – or in other words – that they are isotropic.

The single-pass reflectance coefficient is calculated from the system boundary fluxes (Table ~~1~~2) following Winton (2005) and Kashimura *et al.* (2017):

$$r = \frac{SW_{\downarrow}^{TOA} SW_{\uparrow}^{TOA} - SW_{\downarrow}^{SFC} SW_{\uparrow}^{SFC}}{SW_{\downarrow}^{TOA\ 2} - SW_{\uparrow}^{SFC\ 2}}$$

(~~8~~6)

while the single-pass absorption coefficient a is given as:

$$a = 1 - r - T(1 - \alpha_s r)$$

(~~9~~7)

where T is the clearness index ~~defined in~~(defined in -Table ~~1~~2). Our interest is in quantifying the $SW_{\uparrow,SFC}^{TOA}$ response to an albedo perturbation at the surface – or the partial derivative of $SW_{\uparrow,SFC}^{TOA}$ with respect to α in Eq. (~~7~~5):

$$\frac{\partial SW_{\uparrow}^{TOA}}{\partial \alpha_s} \Delta\alpha_s = K_{\alpha_s}^{ISO} \Delta\alpha_s = \frac{SW_{\downarrow}^{TOA}(1 - r - a)^2}{(1 - r\alpha_s)^2} \Delta\alpha_s$$

(~~10~~8)

where $K_{\alpha_s}^{ISO}$ is referred to henceforth as the ~~*CERES i*~~*Isotropic* kernel.

The second analytical kernel is based on the model of Qu and Hall (2006) which makes use of auxiliary cloud property information commonly provided in satellite-based products of Earth's radiation budget – including CERES EBAF – such as cloud cover area fraction, cloud visible optical depth, and clear-sky planetary albedo. This model links all-sky and clear-sky

effective atmospheric transmissivities of the earth system through a linear coefficient k relating the logarithm of cloud visible optical depth to the effective all-sky atmospheric transmissivity:

$$k = \frac{(T_{a,CLR}) - (T_a)}{\ln(\tau + 1)} \quad (9)$$

where $T_{a,CLR}$ is the clear-sky effective system transmissivity, T_a is the all-sky effective system transmissivity, and τ is the cloud visible optical depth. This linear coefficient can then be used together with the cloud cover area fraction to derive a shortwave kernel based on the model of Qu and Hall (2006) – or $K_{\alpha_s}^{QH06}$:

$$\frac{\partial SW_{\uparrow}^{TOA}}{\partial \alpha_s} \Delta\alpha_s = K_{\alpha_s}^{QH06} \Delta\alpha_s = SW_{\downarrow}^{SFC} \left[(T_a) - kc \ln(\tau + 1) \right] \Delta\alpha_s \quad (10)$$

where c is the cloud cover area fraction.

b. ~~CERES anisotropic~~ Semi-empirical kernel

The ~~second~~ third kernel makes use of three directionally-dependent (anisotropic) bulk optical properties $r_{\uparrow}$, $t_{\uparrow}$, and $t_{\downarrow}$, where the first is the atmospheric reflectivity to upwelling shortwave radiation and the latter two are the atmospheric transmission coefficients for upwelling and downwelling shortwave radiation, respectively (Winton, 2005). It is not possible to derive $r_{\uparrow}$ analytically from the ~~CERES~~ all-sky boundary fluxes; however, Winton (2005) provides an empirical formula relating upwelling reflectivity $r_{\uparrow}$ to the ratio of all-sky to clear-sky fluxes incident at surface:

$$r_{\uparrow} = 0.05 + 0.85 \left(1 - \frac{SW_{\downarrow}^{SFC}}{SW_{\downarrow,CLR}^{SFC}} \right) \quad (11)$$

Field Code Changed
Field Code Changed
Field Code Changed
Field Code Changed
Field Code Changed
Field Code Changed

where $SW_{\downarrow,CLR}^{SFC}$ is the clear-sky shortwave flux incident at the surface.

Knowing $r_{\uparrow}$, we can then solve for the two remaining optical parameters needed to ~~derive~~ obtain our kernel:

$$t_{\downarrow} = \frac{SW_{\downarrow}^{SFC} - r_{\uparrow} SW_{\uparrow}^{SFC}}{SW_{\downarrow}^{TOA}}$$

(~~11~~12)

$$t_{\uparrow} = T_a - \left[t_{\downarrow} - t_{\downarrow}(1 - r_{\uparrow}\alpha_s) \right]$$

(~~12~~13)

where T_a is the effective atmospheric transmittance (Table ~~1~~2) of the earth system.

The ~~anisotropic~~ kernel $K_{\alpha_s}^{ANISO}$ ~~can~~may now be ~~derived~~ expressed as:

$$\frac{\partial SW_{\uparrow}^{TOA}}{\partial \alpha_s} \Delta\alpha_s = K_{\alpha_s}^{ANISO} \Delta\alpha_s = \frac{SW_{\downarrow}^{TOA} t_{\downarrow} t_{\uparrow}}{(1 - r_{\uparrow}\alpha_s)^2} \Delta\alpha_s$$

(~~13~~14)

where $K_{\alpha_s}^{ANISO}$ is henceforth referred to as the *Anisotropic* kernel.

c. ~~CERES a~~Existing empirical parameterizations~~uxiliary input kernel~~

Although not referred to as "kernels" in the literature *per se*, we present ~~them~~the simple empirical parameterizations as such to ensure consistency ~~in~~with previously described notation and terminology~~ henceforth~~. ~~These are subsequently included in the kernel evaluation exercise presented in Section 4.~~

The first ~~simplified kernel~~candidate parameterization, originally presented in Muñoz *et al.* (2010), makes use of a local two-way transmittance factor based on the local clearness index (~~*defined in Table 1*~~):

$$\frac{\partial SW_{\uparrow}^{TOA}}{\partial \alpha_s}\Delta\alpha_s \equiv K_{\alpha_s}^{M10}\Delta\alpha_s = SW_{\downarrow}^{TOA}T^2\Delta\alpha_s \quad (15)$$

where $SW_{\downarrow}^{TOA}$ is the local incoming solar flux at TOA, T is the local clearness index, and $\partial SW_{\uparrow}^{TOA}/\partial\alpha_s$ is the approximated change in the upwelling shortwave flux at TOA due to a change in ~~albedo at~~ the surface albedo.

The second ~~simplified kernel~~candidate parameterization, originally proposed in Cherubini *et al.* (2012), makes direct use of the solar flux incident at the surface $SW_{\downarrow}^{SFC}$ combined with a one-way transmission constant k:

$$\frac{\partial SW_{\uparrow}^{TOA}}{\partial \alpha_s}\Delta\alpha_s \equiv K_{\alpha_s}^{C12}\Delta\alpha_s = SW_{\downarrow}^{SFC}k\Delta\alpha_s \quad (16)$$

where k is based on the global annual mean share of surface reflected shortwave radiation exiting a clear-sky (Lacis and Hansen, 1974;Lenton and Vaughan, 2009) and is hence temporally and spatially invariant. This value – or 0.85 -- is similar to the global mean ratio of forward-to-total shortwave scattering reported in Iqbal (1983). Bright & Kvalevåg (2013) evaluated Eq. (16) at several global locations and found large biases for some regions and months, despite good overall performance globally (~~normalized~~ rRMSE = 7%; n = 120 months).

~~Qu and Hall (2006) developed an alternative analytical kernel to the two described above. The model makes use of auxiliary cloud property information commonly provided in satellite-based products of Earth's radiation budget – including CERES EBAF – such as cloud cover area fraction, cloud visible optical depth, and clear-sky planetary albedo. The model links all-sky and clear-sky effective atmospheric transmissivities of the earth system through a linear coefficient k relating the logarithm of cloud visible optical depth to the effective all-sky atmospheric transmissivity:~~

~~(14)~~

~~where $T_{a,CLR}$ is the clear-sky effective system transmissivity, T_a is the all-sky effective system transmissivity, and τ is the cloud visible optical depth. This linear coefficient can then be used together with the cloud cover area fraction to derive a shortwave kernel based on the model of Qu and Hall (2006) – or $K_{\alpha_s}^{QH06}$:~~

~~(15)~~

~~where c is the cloud cover area fraction.~~

d. ~~CERES statistical kernel~~Novel empirical parameterization

To determine whether the GCM-based kernels could be approximated with sufficient fidelity using ~~even~~ other simpler model formulations based on ~~the CERES~~their own boundary data, we applied machine learning to identify potential model forms using GCM boundary fluxes as input. For the two GCMs kernels in which the GCM's own boundary fluxes are also made available (CAM5 and ECHAM6), we used machine learning to ~~the CERES EBAF all-sky boundary fluxes (or system parameters derived from these fluxes) that~~ minimize~~d~~ the sum of squared residuals between ~~monthly means~~the four shortwave boundary fluxes and the GCM kernel at the monthly time step.~~of four GCM-based kernels (described below) and model~~

~~estimates.~~ The reference dataset consisted of a random global sample of ~~50~~200,000 (~50%) ~~2.8° x 2.8°~~ grid cells at native model resolution (97% and 32% of all cells for ECHAM6 and CAM5, respectively) ~~, from the multi-GMC mean,~~ of which 50% were used for training and 50% for validation. Models were identified using a form of genetic programming known as symbolic regression (Eureqa®; Nutonian Inc.; (Schmidt and Lipson, 2009, 2010)) which searches a wide space of ~~for both optimal~~ model structures as constrained by user input ~~and coefficients~~. In our case, we allowed the model to include the operators (i.e., addition, subtraction, multiplication, division, sine, cosine, tangent, exponential, natural logarithm, factorial, power, square root), but numerical coefficients were forbidden. The model search was allowed to continue until the percent convergence and maturity metrics exceeded 98% and 50%, respectively, at which point more than 1×10^{11} formulae had been evaluated. A parsimonious solution was chosen by minimizing the error metric and model complexity using the Pareto front (Figure S1 of Supporting Information) (Smits and Kotanchek, 2005). Between CAM5 and ECHAM6, four common model solutions were found (Table S1 of Supporting Information). The best of these common solutions is subsequently referred to as $K_{\alpha_s}^{BO18}$ and is given as~~Based on the mean squared deviation (MSD) and Akaike's information criterion (AIC), the best model form of the statistical kernel, subsequently referred to as $K_{\alpha_s}^{BO18}$, is given as~~:

$$\frac{\partial SW_{\uparrow}^{TOA}}{\partial \alpha_s}\Delta\alpha_s = K_{\alpha_s}^{BO18}\Delta\alpha_s = SW_{\downarrow}^{SFC}\sqrt{T}\Delta\alpha_s \quad (\text{~~16~~}17)$$

~~subsequently referred to as $K_{\alpha_s}^{BO18}$, is given as~~

4. Kernel model evaluation

Field Code Changed

~~*d. Initial screening of candidate models for a CERES based kernel*~~

~~Four GCM kernels are employed as benchmarks to initially screen the six CERES based kernel model candidates: the Community Atmosphere Model version 3, or CAM3 (Shell et al., 2008), the Community Atmosphere Model version 5, or CAM5 (Pendergrass et al., 2018), the European Center and Hamburg model version 6, or ECHAM6 (Block and Mauritsen, 2014), and the Geophysical Fluid Dynamics Laboratory model version AM2p12b, or GFDL (Soden et al., 2008). The four GCM kernels vary in vertical and horizontal resolution, parameterization of shortwave radiative transfer, and year of atmospheric state (input variables).~~

a. Initial candidate screening

The four GCM kernels presented in Section 2.b are employed as benchmarks to initially screen the six simple model candidates. We compute a skill metric analogous to the "relative error" metric used to evaluate GCMs by Anav et al. (2013) that takes into account error in the spatial pattern between a model and an observation. Because we have no true observational reference, our evaluation instead focuses on the disagreement or deviation between CERES and GCM kernels at the monthly time step. Given interannual climate variability in the earth system, the challenge of comparing the multi-year CERES kernel to a single-year GCM kernel can be partially overcome by averaging the four GCM kernels.

Using the multi-GCM mean as the reference, we first compute the absolute deviation $AD^{X}_{m,p}$ as:

$$AD^{X}_{m,p} = \left| CERES^{X}_{m,p} - \overline{GCM}_{m,p} \right|$$

(~~17~~18)

where $CERES^{X}_{m,p}$ is the kernel for CERES model candidate ~~*X*~~ *x* in month *m* and pixel *p* and $\overline{GCM}_{m,p}$ is the multi-GCM mean of the same pixel and month. $AD^{X}_{m,p}$ is then normalized to the maximum absolute deviation of all six CERES kernels for the same pixel and month to obtain a normalized absolute deviation, $NAD^{X}_{m,p}$, which is analogous to the "relative error" metric of Anav et al. (2013) ~~with~~ having values ranging between 0 and 1:

$$NAD^{X}_{m,p} = 1 - \frac{AD^{X}_{m,p}}{\max(AD_{m,p})}$$

(~~18~~19)

where $\max(AD_{m,p})$ is the maximum absolute deviation of all six CERES kernels at pixel *p* and month *m*.

CERES kernel ranking is based on the mean relative absolute deviation in both space and time – or $\overline{NAD}^{X}$:

$$\overline{NAD}^{X} = \frac{1}{M}\sum_{m=1}^{M}\frac{1}{P}\sum_{p=1}^{P} NAD^{X}_{m,p}$$

(~~19~~20)

where *M* is the total number of months (i.e., 12) and *P* is the total number of grid cells.

~~*c*~~*b. GCM kernel emulation*

In order to eliminate any bias related to differences in the atmospheric state embedded in the GCM ~~and CERES derived~~ kernel~~s~~ input climatologies, we ~~re-compute our simple kernels~~emulate them by applying the candidate models (or parameterizations) using the original GCM boundary fluxes as input. Emulation is only done for two of GCM-based kernels since only two of them have provided the accompanying ~~same shortwave boundary fluxes used to compute the two most recent albedo change kernels based~~boundary fluxes needed to do so: ~~ on~~ ECHAM6 (Block and Mauritsen, 2014) and CAM5 (Pendergrass et al., 2018). ~~This~~ Emulation enables a more critical evaluation of the functional form of the candidate~~simple~~ models in relation to the more sophisticated radiative transfer schemes employed by ECHAM6 (Stevens et al., 2013) and CAM5 (Hurrell et al., 2013).

c. CACK model uncertainty

Following emulation, monthly GCM kernels are then regressed on the monthly kernels emulated with the leading model candidates. The model that best emulates both GCM kernels – as measured in terms of the mean coefficient of determination (R^2) and mean RMSE – is chosen to represent CACK.

Three sources of uncertainty are considered for CACK when based on the CERES boundary flux climatology (i.e., 2001-2016 monthly means): 1) *physical variability* 2) *data uncertainty*; and 3) *model error* (Mahadevan and Sarkar, 2009)~~.~~~~{}~~. The first is related to the interannual variability of Earth's atmospheric state and boundary radiative fluxes. The second is related to the uncertainty of the CERES EBAF v4 variables used as input to CACK (including measurement error). The third source of uncertainty is the error related to CACK's model form. CACK's combined uncertainty for any given pixel and month is estimated as follows, where if CACK or y is some non-linear function of the CERES boundary inputs x_1 and x_2 that co-vary in time and space, then the combined uncertainty of y – or $\sigma(y)$ – may be

Field Code Changed
Field Code Changed
Field Code Changed
Field Code Changed
Field Code Changed

expressed as the sum of the *model error* plus the combined *physical variability* and *data uncertainty* associated with x_1 and x_2 summed in quadrature (Clifford, 1973;Breipohl, 1970;Green et al., 2017):

$$\sigma(y) \approx \sigma_{ME}(y) + \sqrt{\left(\frac{\partial y}{\partial x_1}\right)^2 \left[\sigma_{PV}(x_1) + \sigma_{DU}(x_1)\right]^2 + \left(\frac{\partial y}{\partial x_2}\right)^2 \left[\sigma_{PV}(x_2) + \sigma_{DU}(x_2)\right]^2 + \sqrt{\left(2\frac{\partial y}{\partial x_1}\frac{\partial y}{\partial x_2}\sigma(x_1,x_2)\right)^2}} \quad (21)$$

where $\sigma_{PV}(x_1)$ and $\sigma_{PV}(x_2)$ are the standard deviations of the 16-yr. climatological record of CERES input variables x_1 and x_2, respectively, for a given grid cell and month, $\sigma_{DU}(x_1)$ and $\sigma_{DU}(x_2)$ are the absolute uncertainties of CERES input variables x_1 and x_2, respectively, for a given grid cell and month, $\sigma(x_1,x_2)$ is the covariance within the 16-yr. climatological record between CERES input variables x_1 and x_2 for a given month and grid cell, and σ_{ME} is the monthly grid cell model error. Model error ($\sigma_{ME}(y)$) and data uncertainties ($\sigma_{DU}(x_n)$) for any given grid cell and month are based on the relative RMSE (Supporting Information) and relative uncertainties of CERES boundary terms reported in Kato *et al.* (2018) (cf. Table 8, "Monthly gridded, Ocean + Land") and Loeb *et al.* (2017) (cf. Table 8, "All-sky, *Terra-Aqua* period"). For the model error, we take the mean relative RMSE of the machine learning model solutions for ECHAM5 and CAM5. For the relative uncertainty of the incoming solar flux at TOA ($SW_{\downarrow}^{TOA}$), we use the 1% "calibration uncertainty" reported in Loeb *et al.* (2017).

If CACK's intended application is to estimate a temporally-explicit ΔF within the CERES era (i.e., if temporally-explicit rather than the climatological mean CERES boundary fluxes are desired to compute CACK), the uncertainty related to *physical variability* ($\sigma_{PV}(x_n)$) can be dropped from Eq. (21).

Field Code Changed

d. Climatological CACK example application

To demonstrate CACK's application when based on monthly CERES EBAF climatology, including the handling of uncertainty, we estimate the annual mean ΔF from a $\Delta\alpha$ scenario associated with hypothetical deforestation in the tropics, where ΔF for a given month is estimated as Eq. (4) where K_{α_s} is the 2001-2016 monthly climatological CACK and $\Delta\alpha$ is the difference in the 2001-2011 monthly climatological mean white-sky surface albedo between "Croplands" (CRO) and "Evergreen broadleaved forests" (EBF) taken from Gao *et al.* (2014) which is based on International Geosphere-Biosphere Program definitions of land cover classification.

The monthly climatological albedo look-up maps of Gao *et al.* (2014) contain their own uncertainties, which we take as the mean absolute difference between the monthly albedos reconstructed using their look-up model and the monthly MODIS retrieval record (c.f. Table 3 in Gao *et al.* (2014)).

The total estimated uncertainty linked to the annual local (i.e., grid cell) instantaneous ΔF can thus be expressed (in W m^{-2}) as:

$$\sigma(\Delta F) = \frac{1}{12}\sum_{m=1}^{12}|\Delta F_m|\sqrt{\left(\frac{\sigma(K_{\alpha_s,m})}{K_{\alpha_s,m}}\right)^2+\left(\frac{\sigma(\Delta\alpha_{s,m})}{\Delta\alpha_{s,m}}\right)^2} \quad (22)$$

where $\sigma(K_{\alpha_s,m})/K_{\alpha_s,m}$ is the relative grid cell uncertainty of CACK and $\sigma(\Delta\alpha_{s,m})/\Delta\alpha_{s,m}$ is the relative uncertainty of $\Delta\alpha_s$ in month *m* defined as:

$$\frac{\sigma(\Delta\alpha_{s,m})}{\Delta\alpha_{s,m}} = \sqrt{\left(\frac{\sigma(\alpha_{s,m})}{\alpha_{CRO,m}}\right)^2+\left(\frac{\sigma(\alpha_{s,m})}{\alpha_{EBF,m}}\right)^2} \quad (23)$$

Field Code Changed
Field Code Changed
Field Code Changed
Field Code Changed
Field Code Changed
Field Code Changed
Field Code Changed
Field Code Changed

where $\sigma(\alpha_{s,m})$ is the monthly absolute uncertainty of the climatological mean surface albedo (i.e., of the Gao *et al*. (2014) product).

e. Temporally-explicit CACK application example

Use of a temporally-explicit CACK may be desirable for time-sensitive applications within the CERES era. This is particularly true for regions experiencing significant changes to the atmospheric state affecting shortwave radiation transfer. A good example is in southern Amazonia where tropical deforestation has been linked to changes in cloud cover (Durieux et al., 2003;Lawrence and Vandecar, 2014;Wright et al., 2017). To exemplify this, we estimate the annual mean instantaneous ΔF for CERES grid cells in the region having experienced significant trends in both surface albedo and cloud area fraction during the 2001-2016 period. Grid cell trends in surface albedo and cloud area fraction are deemed significant if the slopes of linear fits obtained from local (i.e., grid cell) ordinary least squares regressions had p-values ≤ 0.05. We then apply the slope of the surface albedo trend to represent the monthly mean interannal $\Delta\alpha$ incurred over the time series together with CACK updated monthly to estimate the local annual mean instantaneous ΔF at each step in the series:

$$\Delta F(t) = \sum_{m=1}^{m=12} -K_{\alpha_s,m}(t)\Delta\alpha_s \qquad (24)$$

where $K_{\alpha_s,m}(t)$ is the monthly CACK in year t of the time series. ΔF is then averaged across all grid cells in the sample, with the results then compared to the ΔF that is computed for the same grid sample using the time-insensitive CAM5 and ECHAM6 kernels (i.e., $K_{\alpha_s,m} \neq f(t)$). Using the slope of the surface albedo trend as the $\Delta\alpha_s$ for all months and years rather than the actual $\Delta\alpha_{s,m}(t)$ (i.e., $\Delta\alpha_{s,m}(t) = \alpha_{s,m,t} - \alpha_{s,m,t-1}$) yields the same result when averaged over the full time period but allows us to isolate the effect of the changing atmospheric state on

Field Code Changed
Field Code Changed
Field Code Changed
Field Code Changed
Field Code Changed
Field Code Changed
Field Code Changed
Field Code Changed

calculations of ΔF. We limit the ΔF uncertainty estimate to CACK's uncertainty that includes $\sigma_{DU}(x_n)$ and $\sigma_{ME}(x_n)$ ~~e~~but excludes $\sigma_{PV}(x_n)$.

Field Code Changed
Field Code Changed
Field Code Changed

45. Results

a. Initial performance screening

~~*a. Initial kernel performance screening*~~

Seasonally, differences in latitude band means between ~~the CERES~~the CERES kernel candidates and the multi-GCM mean kernels are shown in Figure 1.

< Figure 1 >

Qualitatively, starting with December-January-February (*DJF*), $K_{\alpha_s}^{BO18}$ gives the best agreement with $K_{\alpha_s}^{\overline{GCM}}$ with the exception of the zone around 55 – 65°S (-55 – -65°), where $K_{\alpha_s}^{QH06}$ gives slightly better agreement (Fig. 1A). In March-April-May (*MAM*), $K_{\alpha_s}^{BO18}$ appears to give the best overall agreement with the exception of the high Arctic, where $K_{\alpha_s}^{ANISO}$ and $K_{\alpha_s}^{C12}$ give better agreement, and with the exception of the zone around 60 – 65°S (-60 – -65°) where $K_{\alpha_s}^{QH06}$, $K_{\alpha_s}^{ANISO}$, and $K_{\alpha_s}^{C12}$ agree best with $K_{\alpha_s}^{\overline{GCM}}$ (Fig. 1B). The largest spread in disagreement across all six CERES kernels is found in June-July-August (*JJA*; Fig. 1C) at northern high latitudes. $K_{\alpha_s}^{BO18}$ ~~appears~~appears to agree best both here and elsewhere with the exception of the zone between ~20 – 35°N, where $K_{\alpha_s}^{QH06}$ gives slightly better agreement. In September-October-November (*SON*), $K_{\alpha_s}^{BO18}$ agrees best with $K_{\alpha_s}^{\overline{GCM}}$ at all latitudes except the zone between 10 – 25°N and 55 – 65°S where $K_{\alpha_s}^{QH06}$ agrees slightly better.

Quantitatively, the proportion of the total variance explained by linear regressions of monthly $K_{\alpha_s}^{\overline{GCM}}$ on monthly $K_{\alpha_s}^{CERES}$ (i.e., "R^2") is highest and equal for the CERES kernels based on the ANISO, QH06, and BO18 models (Fig. 2 B, C, & D). Of these three, $K_{\alpha_s}^{QH06}$ has a y-intercept ("B_0") closest to 0 and a slope ("m") of 1, although the root mean squared ~~deviation~~ error ("~~*RMSD*~~*RMSE*") – an accuracy measure – is slightly better (lower) for $K_{\alpha_s}^{BO18}$. The two CERES kernels with the lowest R^2, highest slopes (negative deviations), highest ~~*RMSDs*~~*RMSEs*, and y-intercepts with the largest absolute difference from zero – or the worst performing candidates – are those based on the ISO and M10 models (Fig. 2 A&E).

< Figure 2 >

Although the y-intercept deviation from 0 for $K_{\alpha_s}^{C12}$ is relatively low, its *RMSD* is ~50% higher than that of $K_{\alpha_s}^{QH06}$, $K_{\alpha_s}^{BO18}$, and $K_{\alpha_s}^{ANISO}$ and leads to notable positive deviation from the multi-GCM mean ($K_{\alpha_s}^{\overline{GCM}}$) judging by its slope of 0.92.

~~*c. Normalized absolute deviation*~~

Globally, *NAD* for the QH06, ANISO, and BO18 kernels are far superior to the ISO, M10, and C12 kernels (Table ~~2~~3).

< Table ~~2~~ 3 >

After filtering to remove grid cells for oceans and other water bodies, *NAD* scores for these three kernels decreased; the decrease was smallest for $K_{\alpha_s}^{BO18}$ (-0.03) and largest for $K_{\alpha_s}^{QH06}$ (-

0.06). Despite constraining the analysis to land surfaces only, the rank order remained unchanged (Table ~~2~~3), and $K_{\alpha_s}^{QH06}$, $K_{\alpha_s}^{BO18}$, and $K_{\alpha_s}^{ANISO}$ are subjected to further evaluation. ~~.~~

Field Code Changed
Field Code Changed
Field Code Changed

~~*d*~~*b. GCM kernel emulation and additional performance ~~screening~~evaluation*

However, ~~B~~because ~~the simple kernel based on~~ the QH06 model ($K_{\alpha_s}^{QH06}$) required auxiliary inputs for cloud cover area fraction and cloud optical depth – two atmospheric state variables not provided with the ECHAM6 and CAM5 kernel datasets – it was not possible to emulate these two GCM kernels ~~using~~ with $K_{\alpha_s}^{QH06}$ ~~the QH06 model~~. Additional performance evaluation through GCM kernel emulation is therefore restricted to the ANISO and BO18 models.

Field Code Changed

< Figure 3 >

Globally, the kernel based on the ANISO model displays larger annual mean biases relative to BO18 when compared to both ECHAM6 and CAM5 kernels (Figure 3). Notable positive biases over land with respect to both ECHAM6 and CAM5 kernels are evident in the northern Andes region of South America, the Tibetan plateau, and the tropical island region comprising Indonesia, Malaysia, and Papua New Guinea (Fig. 3 A & C). Notable negative biases over land with respect to both ECHAM6 and CAM5 kernels are evident over Greenland, Antarctica, northeastern Africa, and the Arabian Peninsula (Fig. 3 A & C).

< Figure 4 >

Globally, annual biases for BO18 are generally found to be lower than for ANISO and are mostly non-existent in extra-tropical ocean regions (Fig. 3 B & D). Patterns in biases over land are mostly negative with the exception of Saharan Africa where the annual mean bias

with respect to both GCMs is positive. For BO18, systematic positive biases – or biases evident with respect to both GCM kernels – appear over eastern tropical and subtropical marine coastal upwelling zones where marine stratocumulus cloud dynamics are difficult for GCMs to resolve (Bretherton et al., 2004;Richter, 2015).

< Table ~~3~~ 4 >

~~Performance metrics based on regressing monthly kernels from the two GCMs on kernels emulated with both ANISO and BO18 models~~Regression statistics (Figure 4) indicate a greater overall ~~accuracy (or agreement)~~performance for BO18 ~~(Figure 4)~~than for ANISO. ~~RMSDs~~ RMSEs for monthly kernels emulated with BO18 are 9.0 and 8.2 W m^{-2} ~~with respect to~~for CAM5 and ECHAM6, respectively – which is ~50-60% of the ~~RMSDs~~ RMSEs emulated with the ANISO model. Relative to ANISO, the BO18 model also gives a higher R^2, a slope closer to 1, and a y-intercept closer to zero (Figure 4). The BO18 model (or parameterization) is therefore selected for the CERES albedo change kernel (CACK).

Focusing ~~henceforth~~ only on the ~~only on the kernel emulated with BO18 model~~GCM kernels emulated with $K_{\alpha_s}^{BO18}$ henceforth, negative biases are evident in all months (Table ~~3~~4), with the largest biases (in magnitude) appearing in May (-4.4 W m^{-2}) and November (-2.5 W m^{-2}) for CAM5 and ECHAM6, respectively. In absolute terms, largest biases of 8.6 W m^{-2} and 6.8 W m^{-2} appear in June for CAM5 and ECHAM6, respectively. Annually, the mean absolute bias for CAM5 and ECHAM6 is 6.8 and 6.1 W m^{-2}, respectively – a magnitude which seems remarkably low if one compares this to the annual mean disagreement (standard deviation) of 33 W m^{-2} across all four GCM kernels (not shown; for seasonal mean standard deviations see Fig. 1).

c. CACK uncertainty

Field Code Changed

For a kernel based on 2001-2016 monthly mean CERES EBAF climatology, Figure 5 illustrates the contribution of the absolute error related to $K_{\alpha_s}^{BO18}$'s model form (Fig. 5 A, annual mean) relative to CACK's total absolute uncertainty (Fig. 5 C, annual mean), which includes the uncertainty surrounding CERES EBAF v4 input variables $SW_{\downarrow}^{SFC}$ and $SW_{\downarrow}^{TOA}$ and their interannual variability (Fig. 5 B, annual mean).

< Figure 5 >

Total propagated σ_{pv} and σ_{du} far exceeds σ_{me}, is dominated by $\sigma_{du}(SW_{\downarrow}^{SFC})$ and $\sigma_{pv}(SW_{\downarrow}^{SFC})$, and is largest in the Pacific region to the south of the intertropical convergence zone (ITCZ). Over land, the annual σ_{pv} and σ_{du} as well as the annual σ_{total} are generally largest in arid or high altitude regions (Fig. 5 B). However, annual CACK values are also large in these regions reducing the relative uncertainty (Fig. 5 D). The largest relative uncertainties over land (on an annual basis) – which can approach 50% – are found over central Europe, northwestern Asia, southeastern China, Andean Chile, and northwestern N. America (Fig. 5 D).

d. Climatological CACK application

When estimated with a CACK based on monthly CERES EBAF climatology, the annual ΔF from $\Delta\alpha_s$ linked to hypothetical deforestation in the tropics is negative in most regions, approaching -20 W m^{-2} locally in some regions of the Brazilian Cerrado and south of the Sahel region in Africa (Fig. 6 B). The combined CACK and $\Delta\alpha_s$ uncertainty for these regions can approach ± 5 W m^{-2} annually (Fig. 6 C) in regions like the Brazilian Cerrado and sub-Sahel Africa. Relative to the ΔF magnitude, however, the largest uncertainties (annual)

Field Code Changed
Field Code Changed
Field Code Changed
Field Code Changed
Field Code Changed
Field Code Changed
Field Code Changed
Field Code Changed
Field Code Changed
Field Code Changed
Field Code Changed

may be found in the subtropical regions of Central America, southern Brazil, southern Asia, and northern Australia, where it can approach 30-40% (Fig. 6 D).

e. Temporally-explicit CACK application

The effect of a decreasing cloud cover trend in southern Amazonia (Fig. 7 B) on shortwave radiative transfer and thus a CACK-based estimate of regional mean annual ΔF emerges in Figure 7 C, where ΔF increases in magnitude by 0.004 W m^{-2} from 2002 to 2016. This ΔF trend would otherwise go undetected if a GCM-based kernel were applied to the same surface albedo trend – that is, to a sustained positive interannual monthly albedo change "pulse". Alternatively, a CACK based on 2001 CERES EBAF inputs (applied with $\Delta\alpha_s$ for 2001-2002) would give slightly higher ΔF estimates relative to those based on ECHAM6 and CAM5 kernels; conversely, a CACK based on 2015 CERES EBAF inputs (applied with $\Delta\alpha_s$ for 2015-2016) that would yield lower ΔF estimates relative to those based on the same two GCM-based kernels (Fig. 7 C). Use of temporally-explicit CACK can therefore capture ΔF trends related to a changing atmospheric state that fixed-state GCM kernels are unable to capture.

Field Code Changed

Field Code Changed

5. Discussion ~~and conclusions~~

Motivated by an increasing abundance of climate impact research focusing on land processes in recent years, we comprehensively evaluated six simplified models (or parameterizations) as candidates for an albedo change kernel based on the CERES EBAF v4 products (Loeb et al., 2017;Kato et al., 2018). ~~linking shortwave radiative flux perturbations at TOA with surface albedo changes at the surface.~~ Relative to albedo change kernels based on sophisticated radiative transfer schemes embedded in GCMs, ~~the simplified models evaluated here~~a CERES-based albedo change kernel – or CACK – represents a more transparent and empirically-rooted alternative that can be updated frequently at relatively low cost ~~using~~

~~boundary fluxes obtained from remote sensing based products of Earth's shortwave energy budget~~. This allows greater flexibility to meet the needs of research ~~that focuses~~focusing on ~~longer term~~surface albedo trends within the CERES era in ~~or~~ regions currently undergoing rapid change~~s~~ ~~in~~ to atmospheric ~~composition~~state as it affects shortwave radiation transfer. Although some modeling groups have provided recent updates to ~~radiative~~ their albedo change kernels using the latest GCM versions (e.g., (Pendergrass et al., 2018)), the atmospheric state ~~of the boundary~~ conditions used to derive them may still be considered outdated or not in sync with that required for ~~some~~ many applications (Table 1).

Based on both qualitative and quantitative benchmarking against the mean of four GCM kernels, the ~~simple~~ novel kernel ~~model~~ parameterization ~~derived~~ obtained from machine learning~~,~~ $K_{\alpha_s}^{BO18}$ ~~BO18~~, together with the two (semi-)analytically derived ~~models~~kernels~~,~~ $K_{\alpha_s}^{QH06}$ ~~QH06~~ and $K_{\alpha_s}^{ANISO}$ ~~ANISO~~, proved far superior to the $K_{\alpha_s}^{ISO}$ analytical kernel and to the two additional empirical parameterizations $K_{\alpha_s}^{C12}$ and $K_{\alpha_s}^{M10}$ ~~M10, C12, and the ISO kernel models~~. When subjected to additional performance evaluation, however, we found that $K_{\alpha_s}^{BO18}$ ~~the BO18 model~~ was able to more robustly emulate ~~the~~ two GCM kernels (ECHAM6 and CAM5) ~~kernels~~ with exceptionally high ~~accuracy~~agreement, suggesting that $K_{\alpha_s}^{BO18}$ ~~this model~~ c~~an~~ould serve as a suitable candidate for ~~an albedo change kernel based on CERES boundary fluxes~~CACK.

Relative to the monthly CAM5 and ECHAM6 kernels, ~~T~~the ~~RMSD~~ mean absolute monthly emulation "error" ~~of this kernel – henceforth referred to as the CERES Albedo Change Kernel (CACK v1.0)~~of $K_{\alpha_s}^{BO18}$ – was found to be 6.8 and 6.1 W m^{-2} ~~when benchmarked to the~~,

Field Code Changed
Field Code Changed
Field Code Changed
Field Code Changed
Field Code Changed
Field Code Changed
Field Code Changed
Field Code Changed
Field Code Changed

~~CAM5 and ECHAM6 kernel,~~ respectively – a magnitude which is only ~20% of the standard deviation found across four GCM kernels (annual mean) ~~(annual mean)~~. CACK's remarkable simplicity lends support to the idea of using machine learning to explore and detect emergent properties of ~~shortwave~~ radiative transfer or other complex, interactive model outputs in future research. The fact that the $K_{\alpha_s}^{BO18}$ parameterization emerged as the best common solution from two independently executed machine learning analyses each employing a random sampling unique to a specific GCM kernel suggests that the $K_{\alpha_s}^{BO18}$ parameterization is robust and insensitive to the underlying GCM representation of shortwave radiative transfer.

Field Code Changed

Field Code Changed

Despite ~~the stronger empirical foundation of CACK~~its stronger empirical foundation over a GCM-based kernel, it is important to recognize CACK's ~~its~~ limitations. Firstly, while CACK has a finer spatial resolution than most GCM kernels, it still represents a spatially averaged response rather than a truly local response; in other words, the state variables used to define the $SW_{\uparrow}^{TOA}$ response are averages tied to the coarse spatial (i.e., 1° x 1°) resolution of the CERES EBAF v4 product grids. Secondly, the monthly CERES EBAF-Surface product used to define lower atmospheric boundary conditions is not strictly an observation. The space-borne ~~observation~~ platform is not able to directly ~~observe Earth's surface fluxes~~observe surface irradiances, requiring ~~under overcast conditions and hence requires model augmentation~~additional satellite-based estimates of cloud and aerosol properties as input to a radiative transfer model (Kato et al., 2012). ~~However,~~Although TOA irradiances are applied to constrain the surface irradiances, ~~the energy balancing step ensures that fluxes are adjusted to match the observed rate of heat accumulation in the climate system (i.e., the oceans) (Hansen et al., 2005)~~they remain susceptible to errors in the radiative transfer model inputs.

Field Code Changed

Considering this error as "data uncertainty" increases CACK's overall uncertainty beyond that which is related to its underlying parameterization or "model error". ~~These processes~~The uncertainty of CERES surface shortwave irradiances ~~,~~ as well as extensive ground validation and testing ~~,~~ are documented in greater detail elsewhere (Kato et al., 2013;Loeb et al., 2009;Loeb et al., 2017;Kato et al., 2018) and may continue to be reduced in future EBAF-Surface version~~.~~s. ~~Further, while CACK has a finer spatial resolution than most GCM kernels, it still represents a spatially averaged response rather than a truly local response; in other words, the state variables used to define the response are tied to the course spatial (i.e., 1° x 1°) resolution of the CERES EBAF product grids. Lastly, it is important to emphasize that CACK is based on the climate conditions of the present day (2001-2016); hence, caution should be exercised when applying it to estimate associated with albedo changes occurring outside this range.~~

a. Concluding remarks

To conclude, we developed, evaluated, and proposed a radiative kernel for surface albedo change based on CERES EBAF v4 products – or CACK. Relative to existing kernels based on GCMs, ~~evaluated six simplified albedo change kernels based on CERES shortwave boundary fluxes as candidate alternatives to GCM-based albedo change kernels. Albedo change kernels are useful tools for estimating instantaneous shortwave radiative forcings connected to anthropogenic land use activities. Our results showed that the BO18 model developed and presented in this study is the best candidate for a CERES albedo change kernel – or CACK.~~ CACK provides a higher spatial resolution, higher transparency alternative ~~to existing kernels based on GCMs~~that is more amenable to user needs. For LULCC research of the near-past, present day, or near-future periods, application of a CACK whose inputs are based on

monthly climatological means of the full CERES EBAF record can better-account for the corresponding interannual variability in Earth's atmospheric state affecting shortwave radiative transfer. For regions undergoing changes in atmospheric state that are detectable above the normal variability within the CERES era, application of a temporally-explicit CACK can better-account for its influence on ΔF estimates from surface albedo change. CACK's input flexibility and transparency combined with documented uncertainty make it well-suited to be applied~~CACK could be easily applied~~ as part of a Monitoring, Reporting, and Verification (MRV) framework~~s~~ for biogeophysical impacts on land, analogous to those which currently exist for land sector greenhouse gas emissions.

~~Given the extensive time span of the CERES EBAF products, CACK based on a multi-year climatology of Earth's shortwave radiation budget would better account for internal climate variability in the earth system. However, CACK's flexibility regarding input year should make it broadly appealing across a range of disciplines. One example is the land-based solar radiation management (SRM) research community who frequently calculate fromto evaluate climate mitigation strategies.~~

Code and Dataset Availability

We make both monthly temporally-explicit and monthly climatological mean CACKs for years 2001-2016 available as a complete data product ("CACKv1.0"; netCDF file available at doi:10.6073/pasta/d77b84b11be99ed4d5376d77fe0043d8~~DOI.XXX~~) that includes their respective uncertainty layers. A summary of this dataset and associated variables is provided in Table S3 of the Supporting Information. ~~A~~Octave~~ Matlab~~ script files for generating monthly CACK ~~with user-specified temporal and spatial extents~~ and demonstrating its application with user-specified temporal and spatial extents ~~is~~ are ~~also available at~~

~~DOI.XXX~~bundled with the netCDF file. ~~The 2001-2016 global monthly climatological CACK provided as a Matlab data file is also available at DOI.XXX.~~

Data Availability

CERES EBAF data are available for download at: https://ceres.larc.nasa.gov/products.php?product=EBAF-TOA . The CAM3 kernel is available at: http://people.oregonstate.edu/~shellk/kernel.html . The CAM5 kernel is available at: https://www.earthsystemgrid.org/ac/guest/secure/sso.html . The ECHAM5 kernel is available at: https://swiftbrowser.dkrz.de/public/dkrz_0c07783a-0bdc-4d5e-9f3b-c1b86fac060d/Radiative_kernels/ .

Acknowledgements

R.M.B. was supported by the Research Council of Norway, grants #244074/E20 and #250113/F20; T.L.O. was supported by Climate and Land Use program award #2017-68002-26612 of the USDA National Institute of Food and Agriculture.

References

Anav, A., Friedlingstein, P., Kidston, M., Bopp, L., Ciais, P., Cox, P., Jones, C., Jung, M., Myneni, R., and Zhu, Z.: Evaluating the Land and Ocean Components of the Global Carbon Cycle in the CMIP5 Earth System Models, Journal of Climate, 26, 6801-6843, 10.1175/JCLI-D-12-00417.1, 2013.

Atwood, A. R., Wu, E., Frierson, D. M. W., Battisti, D. S., and Sachs, J. P.: Quantifying Climate Forcings and Feedbacks over the Last Millennium in the CMIP5–PMIP3 Models, Journal of Climate, 29, 1161-1178, 10.1175/jcli-d-15-0063.1, 2016.

Block, K., and Mauritsen, T.: Forcing and feedback in the MPI-ESM-LR coupled model under abruptly quadrupled CO2, Journal of Advances in Modeling Earth Systems, 5, 676-691, 10.1002/jame.20041, 2014.

Bonan, G. B., Pollard, D., and Thompson, S. L.: Effects of Boreal Forest Vegetation on Global Climate, Nature, 359, 716-718, 1992.

Bozzi, E., Genesio, L., Toscano, P., Pieri, M., and Miglietta, F.: Mimicking biochar-albedo feedback in complex Mediterranean agricultural landscapes, Environmental Research Letters, 10, 084014, 2015.

Breipohl, A. M.: Probabilistic systems analysis: an introduction to probabilistic models, decisions, and applications of random processes, Wiley, New York, 1970.

837 Bretherton, C. S., Uttal, T., Fairall, C. W., Yuter, S. E., Weller, R. A., Baumgardner, D., Comstock, K.,
838 Wood, R., and Raga, G. B.: The Epic 2001 Stratocumulus Study, Bulletin of the American
839 Meteorological Society, 85, 967-978, 10.1175/BAMS-85-7-967, 2004.
840 Bright, R. M., and Kvalevåg, M. M.: Technical note: Evaluating a simple parameterization of radiative
841 shortwave forcing from surface albedo change, Atmospheric Chemistry and Physics, 13, 11169-
842 11174, 2013.
843 Bright, R. M.: Metrics for Biogeophysical Climate Forcings from Land Use and Land Cover Changes
844 and Their Inclusion in Life Cycle Assessment: A Critical Review, Environmental Science & Technology,
845 49, 3291-3303, 10.1021/es505465t, 2015.
846 Caiazzo, F., Malina, R., Staples, M. D., Wolfe, P., J. ,, Yim, S. H. L., and Barrett, S. R. H.: Quantifying the
847 climate impacts of albedo changes due to biofuel production: a comparison with biogeochemical
848 effects, Environmental Research Letters, 9, 024015, 2014.
849 Carrer, D., Pique, G., Ferlicoq, M., Ceamanos, X., and Ceschia, E.: What is the potential of cropland
850 albedo management in the fight against global warming? A case study based on the use of cover
851 crops, Environmental Research Letters, 13, 044030, 2018.
852 CERES Science Team: CERES EBAF-Surface Edition 4.0. NASA Atmospheric Science and Data Center
853 (ASDC). https://doi.org/10.5067/TERRA+AQUA/CERES/EBAF-SURFACE_L3B004.0 . Accessed January
854 14, 2018., in, 2018a.
855 CERES Science Team: CERES EBAF-TOA Edition 4.0. NASA Atmospheric Science and Data Center
856 (ASDC). https://doi.org/10.5067/TERRA+AQUA/CERES/EBAF-TOA_L3B004.0 . Accessed January 14,
857 2018. , in, 2018b.
858 Cherubini, F., Bright, R. M., and Strømman, A. H.: Site-specific global warming potentials of biogenic
859 CO2 for bioenergy: contributions from carbon fluxes and albedo dynamics, Environmental Research
860 Letters, 7, 045902, 2012.
861 Clifford, A. A.: Multivariate error analysis: A handbook of error propagation and calculation in many-
862 parameter systems, Applied Science Publishers, London, U. K., 1973.
863 Collins, W. D., Rasch, P. J., Boville, B. A., Hack, J. J., McCaa, J. R., Williamson, D. L., Briegleb, B. P., Bitz,
864 C. M., Lin, S.-J., and Zhang, M.: The Formulation and Atmospheric Simulation of the Community
865 Atmosphere Model Version 3 (CAM3), Journal of Climate, 19, 2144-2161, 10.1175/JCLI3760.1, 2006.
866 Dickinson, R. E., and Henderson-Sellers, A.: Modelling tropical deforestation: A study of GCM land-
867 surface parametrizations, Quarterly Journal of the Royal Meteorological Society, 114, 439-462,
868 10.1002/qj.49711448009, 1988.
869 Dolinar, E. K., Dong, X., Xi, B., Jiang, J. H., and Su, H.: Evaluation of CMIP5 simulated clouds and TOA
870 radiation budgets using NASA satellite observations, Clim. Dyn., 44, 2229-2247, 10.1007/s00382-014-
871 2158-9, 2015.
872 Donohoe, A., and Battisti, D. S.: Atmospheric and Surface Contributions to Planetary Albedo, Journal
873 of Climate, 24, 4402-4418, 10.1175/2011JCLI3946.1, 2011.
874 Durieux, L., Machado, L. A. T., and Laurent, H.: The impact of deforestation on cloud cover over the
875 Amazon arc of deforestation, Remote Sensing of Environment, 86, 132-140,
876 http://dx.doi.org/10.1016/S0034-4257(03)00095-6, 2003.
877 Free, M., and Sun, B.: Trends in U.S. Total Cloud Cover from a Homogeneity-Adjusted Dataset,
878 Journal of Climate, 27, 4959-4969, 10.1175/jcli-d-13-00722.1, 2014.
879 Gao, F., He, T., Wang, Z., Ghimire, B., Shuai, Y., Masek, J., Schaaf, C., and Williams, C.: Multi-scale
880 climatological albedo look-up maps derived from MODIS BRDF/albedo products, Journal of Applied
881 Remote Sensing, 8, 2014.
882 Ghimire, B., Williams, C. A., Masek, J., Gao, F., Wang, Z., Schaaf, C., and He, T.: Global albedo change
883 and radiative cooling from anthropogenic land cover change, 1700 to 2005 based on MODIS, land use
884 harmonization, radiative kernels, and reanalysis, Geophysical Research Letters, 41, 9087-9096,
885 10.1002/2014GL061671, 2014.
886 Green, P., Gardiner, T., Medland, D., and Cimini, D.: WP2: Guide to uncertainty in measurement and
887 its nomenclature. Version 4.0. , U.K., 212, 2017.

888 Hurrell, J. W., Holland, M. M., Gent, P. R., Ghan, S., Kay, J. E., Kushner, P. J., Lamarque, J. F., Large, W.
889 G., Lawrence, D., Lindsay, K., Lipscomb, W. H., Long, M. C., Mahowald, N., Marsh, D. R., Neale, R. B.,
890 Rasch, P., Vavrus, S., Vertenstein, M., Bader, D., Collins, W. D., Hack, J. J., Kiehl, J., and Marshall, S.:
891 The Community Earth System Model: A Framework for Collaborative Research, Bulletin of the
892 American Meteorological Society, 94, 1339-1360, 10.1175/BAMS-D-12-00121.1, 2013.
893 Iqbal, M.: An introduction to solar radiation, Academic Press Canada, Ontario, CA, 389 pp., 1983.
894 Jones, A. D., Calvin, K. V., Collins, W. D., and Edmonds, J.: Accounting for radiative forcing from
895 albedo change in future global land-use scenarios, Climatic Change, 131, 691-703, 10.1007/s10584-
896 015-1411-5, 2015.
897 Kashimura, H., Abe, M., Watanabe, S., Sekiya, T., Ji, D., Moore, J. C., Cole, J. N. S., and Kravitz, B.:
898 Shortwave radiative forcing, rapid adjustment, and feedback to the surface by sulfate
899 geoengineering: analysis of the Geoengineering Model Intercomparison Project G4 scenario, Atmos.
900 Chem. Phys., 17, 3339-3356, 2017.
901 Kato, S., Loeb, N. G., Rose, F. G., Doelling, D. R., Rutan, D. A., Caldwell, T. E., Yu, L., and Weller, R. A.:
902 Surface Irradiances Consistent with CERES-Derived Top-of-Atmosphere Shortwave and Longwave
903 Irradiances, Journal of Climate, 26, 2719-2740, 10.1175/JCLI-D-12-00436.1, 2012.
904 Kato, S., Loeb, N. G., Rose, F. G., Doelling, D. R., Rutan, D. A., Caldwell, T. E., Yu, L., and Weller, R. A.:
905 Surface irradiances consistent with CERES-derived top-of-atmosphere shortwave and longwave
906 irradiances, Journal of Climate, 26, 2719-2740, 2013.
907 Kato, S., Rose, F. G., Rutan, D. A., Thorsen, T. J., Loeb, N. G., Doelling, D. R., Huang, X., Smith, W. L.,
908 Su, W., and Ham, S.-H.: Surface Irradiances of Edition 4.0 Clouds and the Earth's Radiant Energy
909 System (CERES) Energy Balanced and Filled (EBAF) Data Product, Journal of Climate, 31, 4501-4527,
910 10.1175/JCLI-D-17-0523.1, 2018.
911 Lacis, A. A., and Hansen, J. E.: A parameterization for the absorption of solar radiation in the earth's
912 atmosphere, Journal of Atmospheric Sciences, 31, 118-133, 1974.
913 Lawrence, D., and Vandecar, K.: Effects of tropical deforestation on climate and agriculture, Nature
914 Climate Change, 5, 27, 10.1038/nclimate2430

915 https://www.nature.com/articles/nclimate2430#supplementary-information, 2014.
916 Lenton, T. M., and Vaughan, N. E.: The radiative forcing potential of different climate geoengineering
917 options, Atmospheric Chemistry and Physics 9, 5539-5561, 2009.
918 Li, J. L. F., Waliser, D. E., Stephens, G., Lee, S., L'Ecuyer, T., Kato, S., Loeb, N., and Ma, H.-Y.:
919 Characterizing and understanding radiation budget biases in CMIP3/CMIP5 GCMs, contemporary
920 GCM, and reanalysis, Journal of Geophysical Research: Atmospheres, 118, 8166-8184,
921 10.1002/jgrd.50378, 2013.
922 Loeb, N. G., Wielicki, B. A., Doelling, D. R., Smith, G. L., Keyes, D. F., Kato, S., Manalo-Smith, N., and
923 Wong, T.: Toward optimal closure of the Earth's top-of-atmosphere radiation budget, Journal of
924 Climate, 22, 748-766, 2009.
925 Loeb, N. G., Doelling, D. R., Wang, H., Su, W., Nguyen, C., Corbett, J. G., Liang, L., Mitrescu, C., Rose, F.
926 G., and Kato, S.: Clouds and the Earth's Radiant Energy System (CERES) Energy Balanced and Filled
927 (EBAF) Top-of-Atmosphere (TOA) Edition-4.0 Data Product, Journal of Climate, 31, 895-918,
928 10.1175/JCLI-D-17-0208.1, 2017.
929 Lutz, D. A., Burakowski, E. A., Murphy, M. B., Borsuk, M. E., Niemiec, R. M., and Howarth, R. B.:
930 Tradeoffs between three forest ecosystem services across the state of New Hampshire, USA: timber,
931 carbon, and albedo, Ecological Applications, 26, 146-161, 10.1890/14-2207.1, 2015.
932 Lutz, D. A., and Howarth, R. B.: The price of snow: albedo valuation and a case study for forest
933 management, Environmental Research Letters, 10, 064013, 2015.
934 Mahadevan, S., and Sarkar, S.: Uncertainty analysis methods, U.S. Department of Energy,
935 Washington, D.C., USA, 32, 2009.
936 Muñoz, I., Campra, P., and Fernández-Alba, A. R.: Including CO2-emission equivalence of changes in
937 land surface albedo in life cycle assessment. Methodology and case study on greenhouse agriculture,
938 International Journal of Life Cycle Assessment, 15, 672-681, 2010.

939 O'Halloran, T. L., Law, B. E., Goulden, M. L., Wang, Z., Barr, J. G., Schaaf, C., Brown, M., Fuentes, J. D.,
940 Göckede, M., Black, A., and Engel, V.: Radiative forcing of natural forest disturbances, Global Change
941 Biology, 18, 555-565, 2012.
942 Pendergrass, A. G., Conley, A., and Vitt, F. M.: Surface and top-of-atmosphere radiative feedback
943 kernels for CESM-CAM5, Earth Syst. Sci. Data, 10, 317-324, 10.5194/essd-10-317-2018, 2018.
944 Qu, X., and Hall, A.: Assessing Snow Albedo Feedback in Simulated Climate Change, Journal of
945 Climate, 19, 2617-2630, 10.1175/JCLI3750.1, 2006.
946 Randerson, J. T., Liu, H., Flanner, M. G., Chambers, S. D., Jin, Y., Hess, P. G., Pfister, G., Mack, M. C.,
947 Treseder, K. K., Welp, L. R., Chapin, F. S., Harden, J. W., Goulden, M. L., Lyons, E., Neff, J. C., Schuur, E.
948 A. G., and Zender, C. S.: The Impact of Boreal Forest Fire on Climate Warming, Science, 314, 1130-
949 1132, 2006.
950 Rasool, S. I., and Schneider, S. H.: Atmospheric Carbon Dioxide and Aerosols: Effects of Large
951 Increases on Global Climate, Science, 173, 138-141, 10.1126/science.173.3992.138, 1971.
952 Richter, I.: Climate model biases in the eastern tropical oceans: causes, impacts and ways forward,
953 Wiley Interdisciplinary Reviews: Climate Change, 6, 345-358, 10.1002/wcc.338, 2015.
954 Schmidt, M., and Lipson, H.: Distilling free-form natural laws from experimental data, science, 324,
955 81-85, 2009.
956 Schmidt, M., and Lipson, H.: Symbolic regression of implicit equations, in: Genetic Programming
957 Theory and Practice VII, Springer, 73-85, 2010.
958 Shell, K. M., Kiehl, J. T., and Shields, C. A.: Using the Radiative Kernel Technique to Calculate Climate
959 Feedbacks in NCAR's Community Atmospheric Model, Journal of Climate, 21, 2269-2282,
960 10.1175/2007JCLI2044.1, 2008.
961 Smits, G. F., and Kotanchek, M.: Pareto-front exploitation in symbolic regression, in: Genetic
962 programming theory and practice II, Springer, 283-299, 2005.
963 Soden, B. J., Held, I. M., Colman, R., Shell, K. M., Kiehl, J. T., and Shields, C. A.: Quantifying climate
964 feedbacks using radiative kernels, Journal of Climate, 21, 3504-3520, Doi 10.1175/2007jcli2110.1,
965 2008.
966 Srivastava, R.: Trends in aerosol optical properties over South Asia, International Journal of
967 Climatology, 37, 371-380, doi:10.1002/joc.4710, 2017.
968 Stephens, G. L., O'Brien, D., Webster, P. J., Pilewski, P., Kato, S., and Li, J.-l.: The albedo of Earth,
969 Reviews of Geophysics, 53, 141-163, 10.1002/2014RG000449, 2015.
970 Stevens, B., Giorgetta, M., Esch, M., Mauritsen, T., Crueger, T., Rast, S., Salzmann, M., Schmidt, H.,
971 Bader, J., Block, K., Brokopf, R., Fast, I., Kinne, S., Kornblueh, L., Lohmann, U., Pincus, R., Reichler, T.,
972 and Roeckner, E.: Atmospheric component of the MPI-M Earth System Model: ECHAM6, Journal of
973 Advances in Modeling Earth Systems, 5, 146-172, doi:10.1002/jame.20015, 2013.
974 Taylor, K. E., Crucifix, M., Braconnot, P., Hewitt, C. D., Doutriaux, C., Broccoli, A. J., Mitchell, J. F. B.,
975 and Webb, M. J.: Estimating Shortwave Radiative Forcing and Response in Climate Models, Journal of
976 Climate, 20, 2530-2543, 10.1175/JCLI4143.1, 2007.
977 The GFDL Global Atmospheric Model Development Team: The New GFDL Global Atmosphere and
978 Land Model AM2–LM2: Evaluation with Prescribed SST Simulations, Journal of Climate, 17, 4641-
979 4673, 10.1175/JCLI-3223.1, 2004.
980 Vanderhoof, M., Williams, C. A., Ghimire, B., and Rogan, J.: Impact of mountain pine beetle outbreaks
981 on forest albedo and radiative forcing, as derived from Moderate Resolution Imaging
982 Spectroradiometer, Rocky Mountains, USA, Journal of Geophysical Research: Biogeosciences, 118,
983 1461-1471, 10.1002/jgrg.20120, 2013.
984 Wang, H., and Su, W.: Evaluating and understanding top of the atmosphere cloud radiative effects in
985 Intergovernmental Panel on Climate Change (IPCC) Fifth Assessment Report (AR5) Coupled Model
986 Intercomparison Project Phase 5 (CMIP5) models using satellite observations, Journal of Geophysical
987 Research: Atmospheres, 118, 683-699, doi:10.1029/2012JD018619, 2013.
988 Winton, M.: Simple optical models for diagnosing surface-atmosphere shortwave interactions,
989 Journal of Climate, 18, 3796-3806, 2005.

990 Winton, M.: Surface Albedo Feedback Estimates for the AR4 Climate Models, Journal of Climate, 19,
991 359-365, 10.1175/jcli3624.1, 2006.
992 Wright, J. S., Fu, R., Worden, J. R., Chakraborty, S., Clinton, N. E., Risi, C., Sun, Y., and Yin, L.:
993 Rainforest-initiated wet season onset over the southern Amazon, Proceedings of the National
994 Academy of Sciences, 201621516, 10.1073/pnas.1621516114, 2017.
995 Zhao, D., Xin, J., Gong, C., Wang, X., Ma, Y., and Ma, Y.: Trends of Aerosol Optical Properties over the
996 Heavy Industrial Zone of Northeastern Asia in the Past Decade (2004–15), Journal of the Atmospheric
997 Sciences, 75, 1741-1754, 10.1175/jas-d-17-0260.1, 2018.

998

Table 1. Attributes of existing GCM kernels, all of which having a monthly temporal resolution.

Kernel	Base climatology extent	Base climatology period	Shortwave Radiative transfer	Horizontal Resolution	References
ECHAM6	1,000 years	Preindustrial*	RRTM-G	1.88° × 1.88°	(Block and Mauritsen, 2014;Stevens et al., 2013)
CAM3	6 years	1995-2000	δ-Eddington	1.4° × 1.4°	(Shell et al., 2008;Collins et al., 2006)
CAM5	1 year	2006-2007	RRTM-G	0.94° × 1.25°	(Pendergrass et al., 2018)
GFDL	17 years	1979-1995	Exponential sum-fits, 18 bands	2° × 2.5°	(Soden et al., 2008;The GFDL Global Atmospheric Model Development Team, 2004)

*Atmospheric CO_2 concentration = 284.7 ppmv; Exact time period unknown

Table ~~1~~2. Definition of CERES input variables and other system optical properties derived from CERES inputs. All variables ~~are~~ have a ~~2001-2016 monthly means~~monthly temporal resolution and a ~~at 1° × 1°~~ spatial resolution of 1° × 1°.

CERES EBAF v.4 Shortwave Boundary Fluxes		
$SW_{\downarrow}^{TOA}$	Downwelling solar flux at top-of-atmosphere	Wm^{-2}
$SW_{\downarrow}^{SFC}$	Downwelling solar flux at surface	Wm^{-2}
$SW_{\downarrow,CLR}^{SFC}$	Clear-sky downwelling solar flux at surface	Wm^{-2}
$SW_{\uparrow}^{TOA}$	Upwelling solar flux at top-of-atmosphere	Wm^{-2}
$SW_{\uparrow}^{SFC}$	Upwelling solar flux at surface	Wm^{-2}
System Optical Properties		
$T = SW_{\downarrow}^{SFC} / SW_{\downarrow}^{TOA}$	Clearness index	unitless
$\alpha_p = SW_{\uparrow}^{TOA} / SW_{\downarrow}^{TOA}$	Planetary albedo	unitless
$\alpha_s = SW_{\uparrow}^{SFC} / SW_{\downarrow}^{SFC}$	Surface albedo	unitless
$A_p = 1 - \alpha_p$	Effective planetary absorption	unitless
$A_s = \left[SW_{\downarrow}^{SFC} - SW_{\uparrow}^{SFC} \right] / SW_{\downarrow}^{TOA}$	Effective surface absorption	unitless
$A_a = A_p - A_s$	Effective atmospheric absorption	unitless
$T_a = 1 - A_a$	Effective atmospheric transmission	unitless
$T_{a,CLR} = 1 - A_{a,CLR}$	Clear-sky effective atmospheric transmission	unitless
τ	Cloud visible optical depth	unitless
c	Cloud area fraction	fraction

Table 23. Normalized absolute deviation and CERES kernel model candidate ranking.

	Global		Land only		
	$\overline{NAD}$	Rank	$\overline{NAD}$	Rank	Mean Rank
ISO	0.05	6	0.05	6	*6*
ANISO	0.64	3	0.59	3	*3*
C12	0.45	4	0.47	4	*4*
M10	0.26	5	0.34	5	*5*
QH06	0.66	2	0.60	2	*2*
BO18	0.67	1	0.64	1	*1*

Table ~~3~~4. Global monthly mean bias (*MB*) and mean absolute bias (*MAB*) for K_α^{BO18} emulated with T and $SW_\downarrow^{SFC}$ from ECHAM6 and CAM5. For reference, the global mean value of K_α^{BO18} is 133 W m^{-2}.

MB (W m^{-2})

	Jan.	**Feb.**	**Mar.**	**Apr.**	**May**	**Jun.**	**Jul.**	**Aug.**	**Sep.**	**Oct.**	**Nov.**	**Dec.**	**Ann.**
$K_\alpha^{BO18} - K_\alpha^{CAM5}$	-2.9	-3.4	-3.3	-3.9	-4.4	-3.8	-3.8	-3.7	-3.4	-3.8	-3.7	-3.3	-3.6
$K_\alpha^{BO18} - K_\alpha^{ECHAM6}$	-1.9	-2.2	-1.8	-1.9	-2.2	-1.5	-1.1	-1.6	-1.7	-2.5	-2.5	-1.8	-1.9

MAB (W m^{-2})

	Jan.	**Feb.**	**Mar.**	**Apr.**	**May**	**Jun.**	**Jul.**	**Aug.**	**Sep.**	**Oct.**	**Nov.**	**Dec.**	**Ann.**
$\lvert K_\alpha^{BO18} - K_\alpha^{CAM5} \rvert$	6.9	5.7	5.2	6.8	7.7	8.6	7.9	6.7	5.6	6.1	6.9	6.9	6.8
$\lvert K_\alpha^{BO18} - K_\alpha^{ECHAM6} \rvert$	6.3	5.7	5.0	5.9	6.7	6.8	6.4	5.8	5.3	5.6	6.4	6.7	6.1

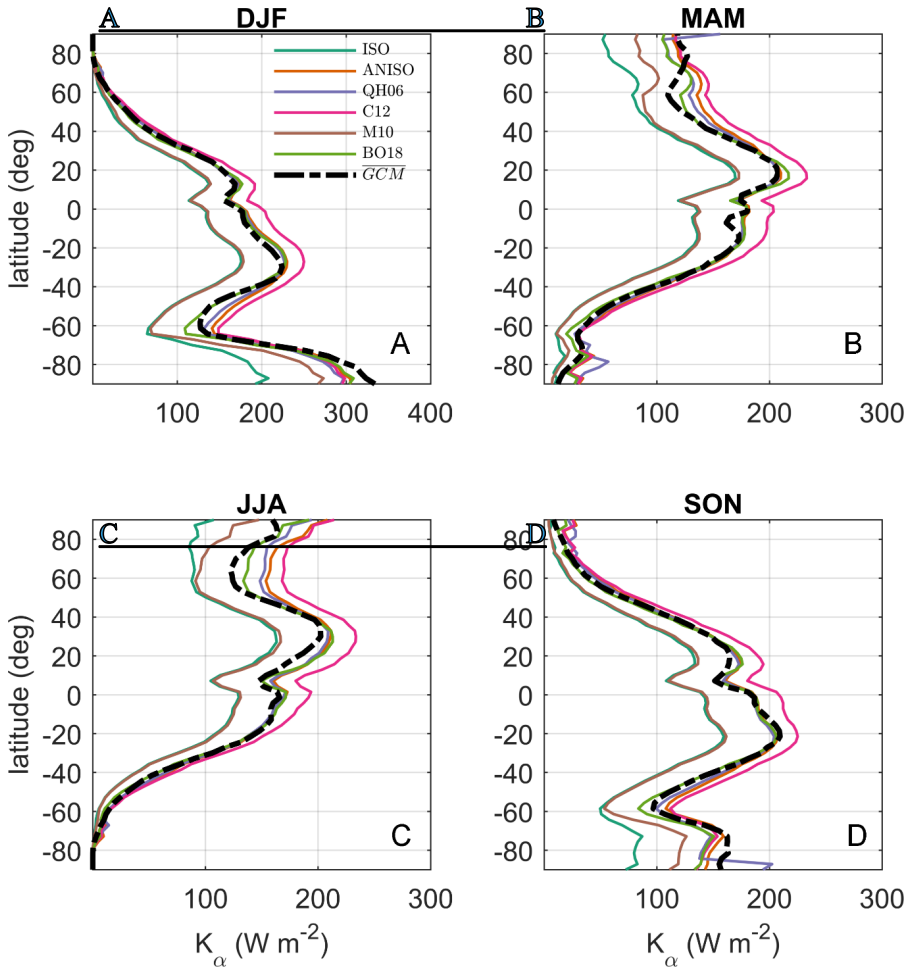
A
DJF
B
MAM
C
JJA
D
SON
ISO
ANISO
QH06
C12
M10
BO18
GCM
latitude (deg)
80
60
40
20
0
-20
-40
-60
-80
100
200
300
400
K$_\alpha$ (W m^{-2})

1013

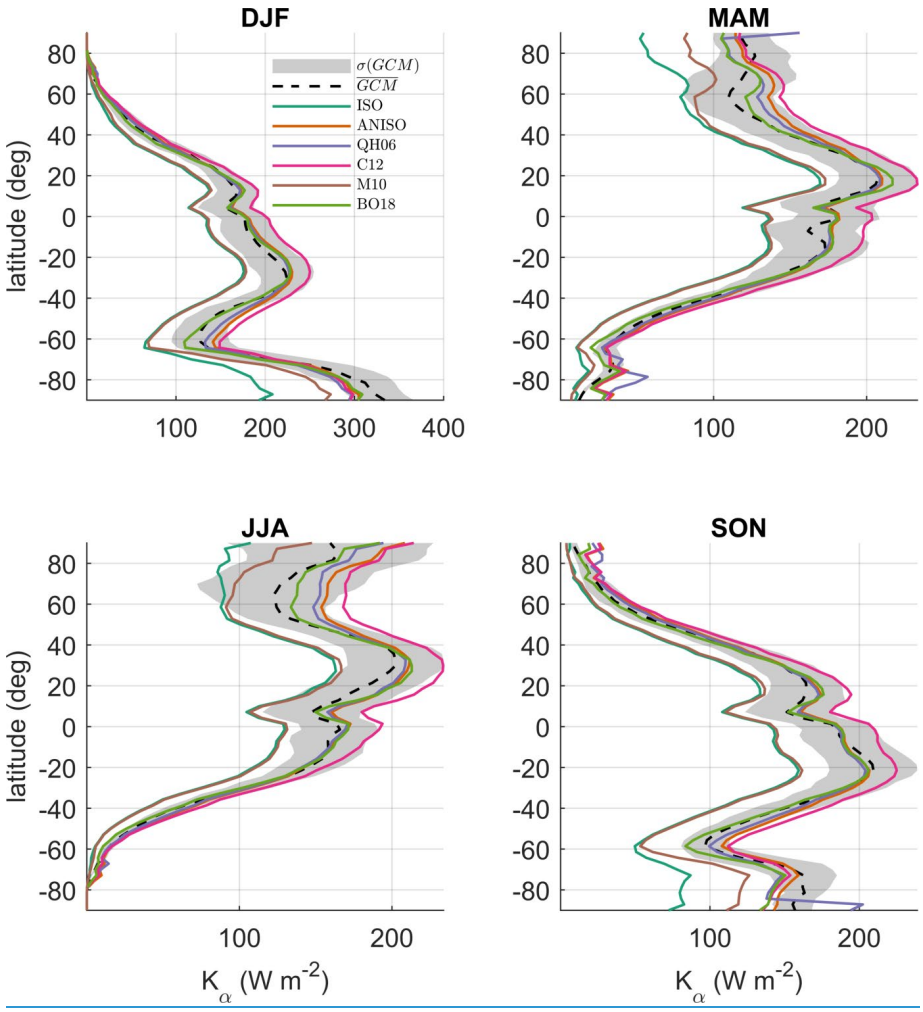

Figure 1. Latitudinal (1°) and seasonal means of the multi-GCM mean ($K_\alpha^{\overline{GCM}}$) and CACK ~~K_α^{CERES}~~ model candidates for: A) December-January-February (DJF); B) March-April-May (MAM); C) June-July-August (JJA); D) September-October-November (SON).

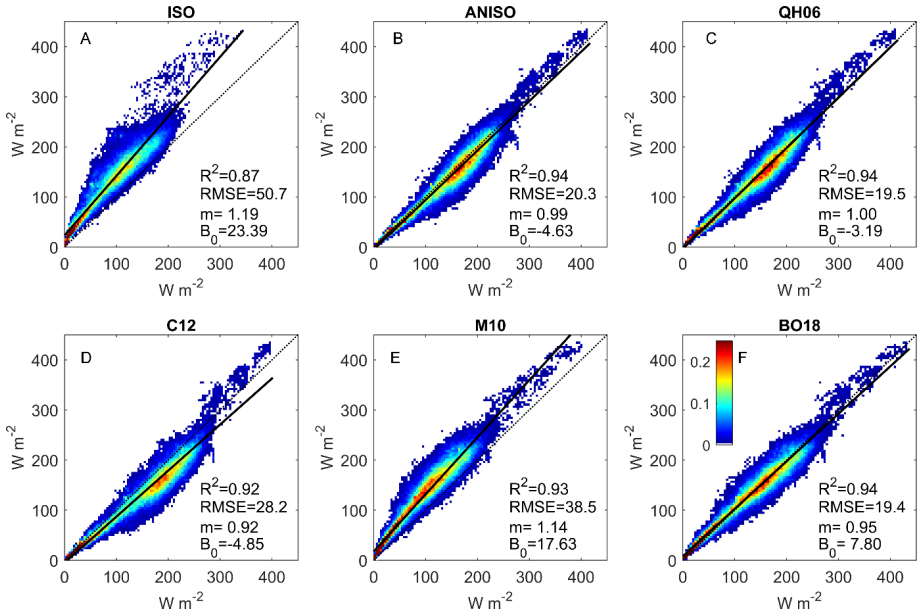

Figure 2. A)-F): Scatter-density regressions of global monthly mean $K_{\alpha}^{\overline{GCM}}$ (y-axis) and K_{α}^{CERES} (x-axis), with the CERES kernel identifier shown at the top of each sub-panel. "*m*" = slope; "B_0" = y-intercept. The color scale indicates the percentage of regression points that fall within an averaging bin, where the x-axis and y-axis have been gridded into 100 × 100 equally-spaced bins to help illustrate the density of overlapping points. ~~The color scale indicates the percentage of regression points that fall within a 100 × 100 sample grid centered on the plotted point.~~

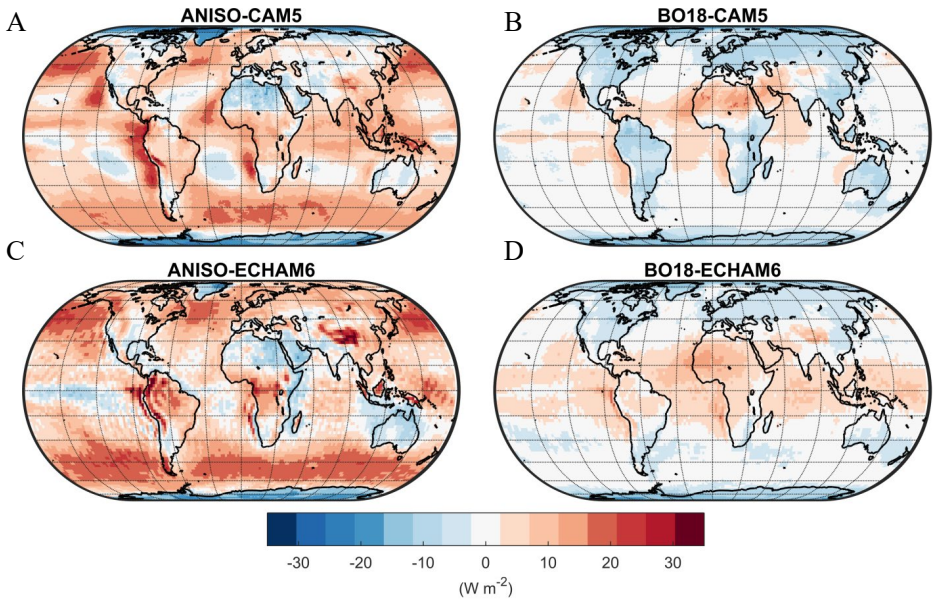

Figure 3. A) Mean annual bias of the CAM5 albedo change kernel emulated with the ANISO ~~analytical~~ semi-empirical model; B) Mean annual bias of the CAM5 albedo change kernel emulated with the BO18 parameterization; C) Mean annual bias of the ECHAM6 albedo change kernel emulated with the ANISO semi-empirical~~analytical~~ model; D) Mean annual bias of the ECHAM6 albedo change kernel emulated with the BO18 parameterization

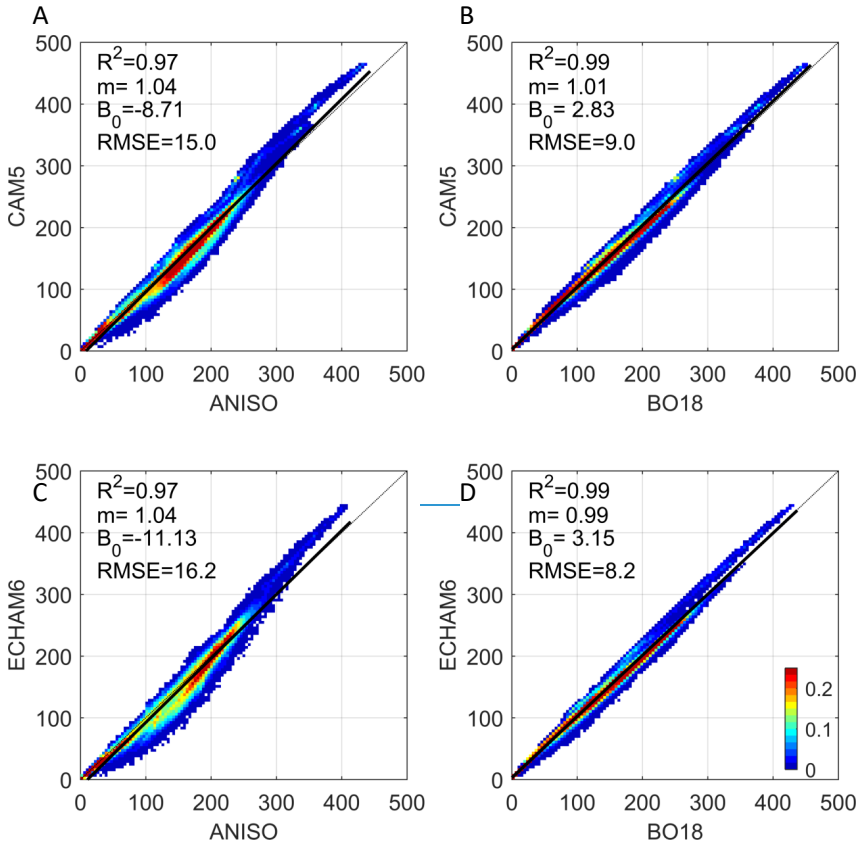

Figure 4. A)-D): Scatter-density regressions of K_{α}^{GCM} (y-axis) and K_{α}^{GCM} emulated with the ANISO semi-empirical model and BO18 parameterization (x-axis); "m" = slope; "B_0" = y-intercept. ~~The color scale indicates the percentage of regression points that fall within a 100 × 100 sample grid centered on the plotted point.~~See Figure 2 caption for a description of the color scale.

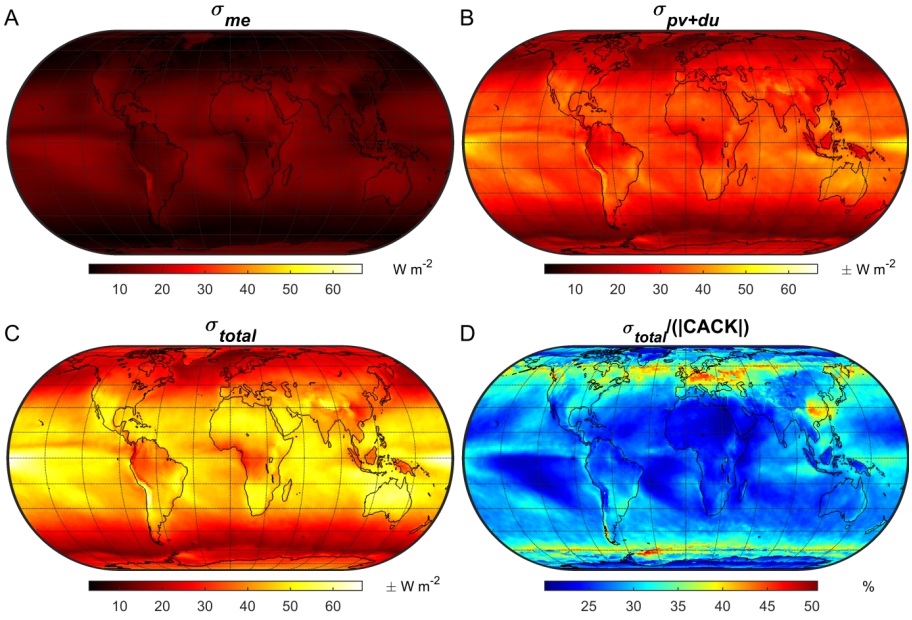

Figure 5. Annual uncertainty of a CACK based on 2001-2016 monthly mean CERES EBAF v4 climatology: A) The absolute uncertainty related to *model error* (i.e., the $K_{\alpha_s}^{BO18}$ parameterization); B) The total propagated absolute uncertainty related to *physical variability* and *data uncertainty* of CACK input variables; C) Total absolute uncertainty; D) Total relative uncertainty.

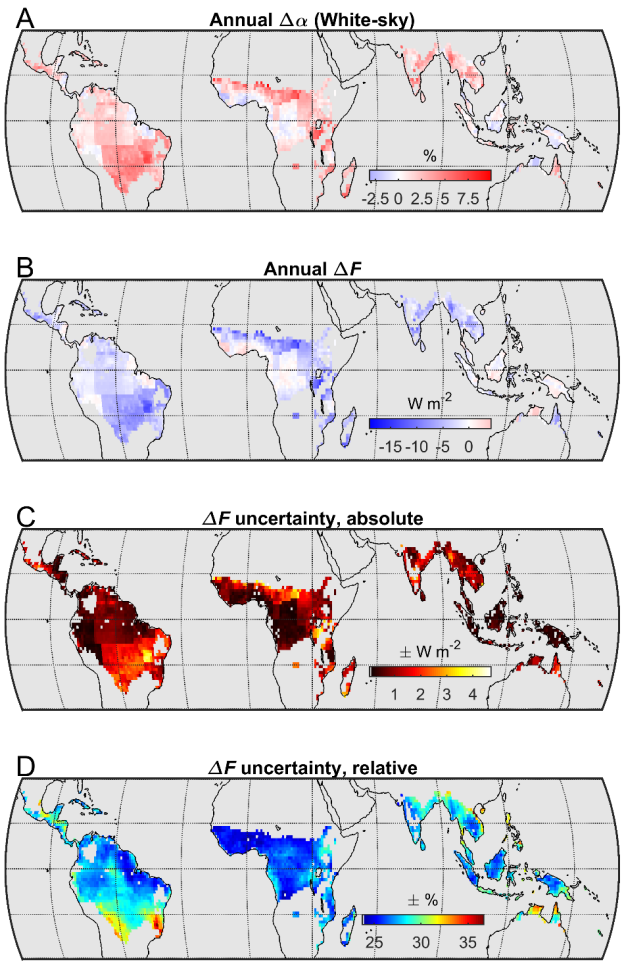

Figure 6. Example application of a CACK based on the 2001-2016 monthly mean CERES EBAF v4 climatology. A) Annual mean of the climatological (i.e., 2001-2011) monthly mean difference in white-sky surface albedo between *grasslands* and *evergreen broadleaved forests* ($\Delta\alpha_s$) based on the 1° product of Gao *et al.* (2014); B) Annual mean instantaneous radiative forcing (ΔF) of monthly mean $\Delta\alpha_s$ estimated with CACK; C) Absolute uncertainty

Field Code Changed

Field Code Changed

Field Code Changed

(annual mean) of the CACK-based ΔF estimate, including the uncertainty of $\Delta\alpha_s$; D)

Relative uncertainty (annual mean) of the CACK-based ΔF estimate.

Field Code Changed

Field Code Changed

Field Code Changed

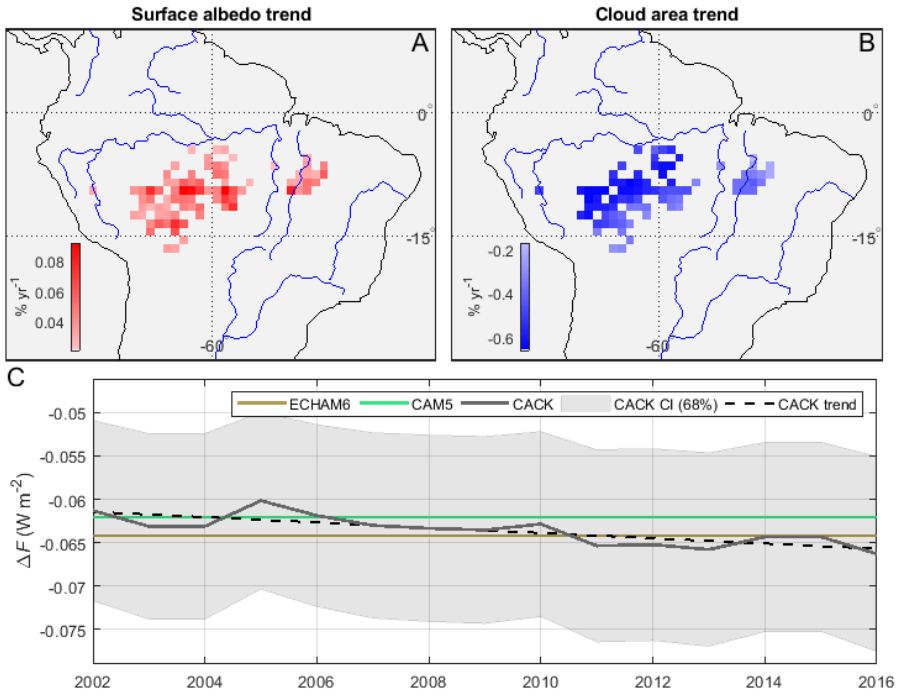

Figure 7. Example application of a temporally-explicit CACK. A) 2001-2016 statistically significant positive trends in all-sky *surface albedo* derived from CERES EBAF-Surface v4; B) 2001-2016 statistically significant negative trends in *cloud area* derived from CERES EBAF-TOA v4; C) Mean local ΔF from $\Delta\alpha_s$ when estimated with the CACK, ECHAM6, and CAM5 surface albedo change kernels. The 1σ confidence interval ("CI") shown for CACK excludes the uncertainty component related to *physical variability*.

Field Code Changed

Field Code Changed